Probing Neutron Star Interiors with Type I X-ray Bursts

Michael Zamfir

Department of Physics
McGill University
Montréal, Québec
Canada

November 17, 2014

A Thesis submitted to McGill University
in partial fulfillment of the requirements of the degree of
Doctor of Philosophy

Contents

List of Figures

List of Tables

Abstract

The study of Type I X-ray bursts, brief and bright flashes in X-rays from neutron star binary systems, can reveal clues about the structure, composition and thermal properties of neutron star interiors. Here, we pursue two different approaches to probing the interior of neutrons stars. Firstly, we develop a method to derive constraints on the mass and radius which are independent of distance to the source, and anisotropic emission. We apply this method to the regular bursting source GS $1826-24$, and derive upper limits on the neutron star radius "at infinity", $R_\infty = R(1+z)$, where R is the neutron star radius and z is the gravitational redshift from the neutron star surface. We then explore the effects of varying composition on lightcurves in mixed H/He bursts, and show that the behaviour of GS $1826-24$ is not yet well understood. We calibrate an empirical law relating the peak flux of a burst to the average helium mass fraction at ignition to KEPLER multizone burst simulations. Using this law, we suggest an accretion composition for GS $1826-24$ that has low-metallicity and is helium-enriched, with respect to solar values. In chapter 4, we attempt to constrain a shallow heat source to explain the transition from stable to unstable burning in 4U $1820-30$. We map the critical accretion rate at this transition as a function of a heat flux which emerges from deeper layers.

Résumé

L'étude de sursauts the Type I peut révélé des indices sur la structure, la composition, et les propriétés de l'intérieur des étoiles à neutrons. Ici, nous poursuivons deux différentes approches pour sonder l'intérieur des étoiles à neutrons. Premièrement, nous développons une méthode pour mesurer la masse et le rayon qui est indépendante de la distance à la source, et l'anisotropie de l'émission. Nous appliquons cette méthode à une source présentant des sursauts réguliers, GS $1826-24$, et obtenons des limites supérieures sur R_∞. Ensuite, nous explorons les effets d'une variation de la composition sur les courbes de lumière de sursauts de types "mixed H/He", et démontrons que le comportement de GS $1826-24$ n'est pas entièrement compris. Nous calibrons une loi empirique qui relie le flux maximal à la fraction de masse moyenne d'hélium au moment du sursaut aux simulations à zones multiples. Grâce a cette loi, nous suggérons une composition de l'accrétion pour GS $1826-24$ qui a une basse metallicité et qui est enrichie en hélium, comparé à la composition solaire. Dans le Chapitre 4, nous essayons de determiner la quantité de chaleur à faible profondeur nécessaire pour expliquer la transition entre les états de combustion stable et instable de 4U $1820-30$. Nous déterminons le taux d'accrétion critique à cette transition en fonction du flux de chaleur qui émerge des couches profondes.

Acknowledgments

I wish to acknowledge my supervisor, Andrew Cumming, to whom I am indebted for his guidance, support, and above all, his patience and willingness to help.

I also wish to thank my family who have always supported me in the pursuit of my goals.

I thank all my friends and colleagues at McGill and elsewhere who have helped make these past years truly enriching.

Contributions of Authors

My thesis supervisor Andrew Cumming was involved in all stages of my doctoral work. Specifically, he provided ideas for projects, valuable scientific discussions, as well as direct help with the research and writing that has gone into this thesis.

Chapter 2

This work was originally published as: M. Zamfir, A. Cumming, D. K. Galloway, *Constraints on Neutron Star Mass and Radius in GS 1826-24 from Sub-Eddington X-ray Bursts.* ApJ, 749:69, April 2012

The contribution of the co-authors is as follows. Galloway provided the data analysis, the text describing the data analysis in §2.2, and helpful comments and discussion at various stages of the draft. Cumming provided the early motivation for this project and assistance at all stages of the research and writing.

Chapter 3

I wish to acknowledge contribution to this chapter from A. Cumming, D. K. Galloway, N. Lampe and A. Heger. Heger contributed simulations of bursts using KEPLER. Lampe and Galloway analyzed the lightcurves to extract the useful parameters that we used in this chapter. Galloway also provided the observational data that we used in our comparison, from his catalog (Galloway et al., 2004). Cumming provided the idea for this project and assistance at all stages of the research and writing.

Chapter 4

This chapter was published as: M. Zamfir, A. Cumming, C. Niquette, *The Thermal Stability of Helium Burning in Accreting Neutron Stars.* MNRAS, vol. 445, 3278, 12/2014.

The contribution of the co-authors is as follows. Niquette, as part of her M.Sc. work, developed the method for the linear stability analysis which is used in this chapter. Cumming provided the idea for this project and assistance at all stages of the research and writing.

Probing Neutron Star Interiors with Type I X-ray Bursts

1

Introduction

Neutron stars, formed from the collapsed core of massive stars, are the densest directly observable objects in the universe. Their mass is similar to that of the Sun, but with a diameter believed to be of only ∼20 km, the average density is expected to be in excess of $10^{14}\,\mathrm{g\,cm^{-3}}$. Harbouring this extreme form of matter, neutron star interiors serve as unique laboratories for nuclear physics. From observations of radiative phenomena originating at or near the surface of neutron stars, we can probe their interiors with the aim of ultimately constraining the properties of matter at and above nuclear densities. The focus of this thesis is one such phenomenon – Type I X-ray bursts. These are bright momentary flashes in X-rays caused by unstable nuclear reactions taking place within several meters beneath the neutron star surface.

This chapter will introduce the reader to the neutron star structure, their formation, Type I X-ray bursts and the current approaches to constraining the interior properties of neutron stars.

1.1 Neutron stars and their structure

The surface of the neutron star consists of mostly light nuclei such as hydrogen, helium and carbon, in a cloud of unbound electrons. Within a few meters, the density reaches $\rho \sim 10^6\,\mathrm{g\,cm^{-3}}$, where the electrons become relativistic, meaning that their Fermi energy exceeds their rest mass energy, $E_F > m_e c^2$. This increase in the electron Fermi energy makes it energetically favourable for some protons to capture electrons, thereby being converted into neutrons. At this depth, the electrons are fully degenerate, and provide the pressure support. As the density is increased, the nuclei become increasingly neutron-rich. At a density of $\sim 10^9\,\mathrm{g\,cm^{-3}}$ the liquid ocean begins to solidify into an ion lattice, marking the start of the outer crust. When a density of $\sim 4 \times 10^{11}\,\mathrm{g\,cm^{-3}}$ is reached, a few hundred meters below the surface, the neutron-rich nuclei become unable to accomodate additional neutrons. This leads to the most energetic neutrons becoming unbound from their host nuclei, a phenomenon called called neutron drip. This part of the neutron star is called the inner crust.

At a depth of around one kilometre, the density approaches that of nucleon matter in heavy atomic nuclei, which is $\rho = 2.8 \times 10^{14}\,\mathrm{g\,cm^{-3}}$ (Haensel et al., 2007). The density of free neutrons is comparable to that of neutrons bound inside nuclei, and the nuclei merge to form a fluid consisting of mostly free neutrons, with $5 - 10\%$ contribution of protons, with the necessary density of electrons to ensure the electrical neutrality of the matter. Below this depth, the properties and composition of the matter are theoretically uncertain, and the focus of ongoing research (see Page & Reddy 2006 for a review). The appearance of different exotic phases of the matter have been suggested, such as pion or kaon condensates, or possibly a transition to a deconfined quark plasma (Witten, 1984; Haensel et al., 1986). The different theories imply different physical properties for the matter, such as the compressibility, which influences the size that a neutron star will have as a function of mass. For example, if the equation of state, which relates the pressure to the density, is *soft* then the maximum mass a neutron star can reach will be lower than the mass attainable with a *stiff* equation of state (Prakash et al., 1988).

There is a direct mapping between the equation of state and a mass-radius relationship via the integration of the Tolman-Oppenheimer-Volkov equations (Oppenheimer & Volkoff, 1939). Measurements of neutron star masses and radii can therefore provide valuable clues needed to constrain the properties of matter above nuclear densities (Lattimer & Prakash, 2007).

The progenitors of neutron stars are believed to be evolved stars with masses in the range of $8 - 20M_{\odot}$. A massive star will evolve through cycles of fusion of progressively heavier elements in its core burning. This ends with the buildup of a core of iron, at which point fusion reactions, instead of releasing energy, require it. The core, being supported by electron-degeneracy pressure, collapses once its mass exceeds the Chandrasekhar limit, which is $\sim 1.4M_{\odot}$. The implosion of the core releases $\sim 10^{53}$ ergs of gravitational energy, causing the envelope of the collapsing star to be violently ejected in a supernova event. The nascent proto-neutron star is initially very hot, with temperatures on the order of $10^{11} - 10^{12}$ K, but rapidly cools down due to large neutrino emission (Prakash et al., 2001). For the next $\sim 10^5$ years, neutrino emission will be the dominant channel by which the neutron star cools. Later, the dominant cooling mechanism will shift to the thermal diffusion of heat from the internal layers out to the neutron star surface, resulting in the emission of photons. When the neutron star has thermally relaxed, the temperature becomes uniform throughout. The rate at which a neutron star cools during its neutrino-dominated phase is sensitive to the composition and properties of the core, while during the photon phase, the cooling becomes sensitive to the outer parts of the neutron star. The modelling of neutron star cooling and comparisons to observations can therefore be very useful in probing the interior properties (e.g. Page et al. 2011, or see Yakovlev & Pethick 2004 for a review).

1.2 Neutron Stars in Low Mass X-ray binaries

There are an estimated 10^9 neutron stars in our galaxy (Timmes et al., 1996), of which only a tiny fraction, on the order of $\sim 10^3$, have been observed. Isolated neutron stars make up a large majority of known neutron star sources. Among those isolated sources, an overwhelming fraction is manifested as pulsars, detected from their radio-frequency pulsations. Pulsar emission is believed to be powered by the spin-down of the neutron star dipole-like magnetic field (Goldreich & Julian, 1969). From their spin-down rates, it is possible to infer the strength of their magnetic fields, which show a range of $10^8 - 10^{14}$ G. The spin periods of known pulsars vary from a few seconds, down to ~ 1.5 milliseconds (Backer et al., 1982). The most rapidly spinning neutron stars are likely the result of a few billion years of angular momentum transfer from mass accretion in a class of binaries called low-mass X-ray binaries (LMXB) (Smarr & Blandford, 1976).

An estimated 10% of the observable neutron stars in our Galaxy are found in LMXBs (Liu et al., 2007). These systems have likely evolved from a binary consisting of two main sequence stars, one of which has a mass in the range of a neutron star progenitor ($8 - 20 M_\odot$), the other having a mass similar to that of the sun. If the binary is not disrupted by the violent collapse of the massive star into a neutron star, accretion from the low mass star onto its compact companion may eventually commence. The mass transfer proceeds via Roche-lobe overflow, forming an accretion disk around the neutron star (see Tauris & van den Heuvel 2003 for a review). Due to the large gravity and compact size of a neutron star, the gravitational energy released from the infalling mass causes the accretion disk and the neutron star surface to radiate brightly in X-rays.

The mass that is accreted from the low-mass companion onto the neutron star surface is typically composed of a mixture of hydrogen and helium, with a small proportion of "metals" (a term used in astronomy to refer to any element heavier than helium). Most LMXBs have orbital periods of a few hours, but a small subset, called ultra-compact X-ray binaries (UCXB), are known to have periods of roughly less than an hour. In these systems, the donor is either an evolved star which has shed its hydrogen envelope and is mostly composed of helium (sdB star), or a white dwarf. These are the only known stars that can fill their Roche lobe in the small orbits that characterize ultra-compact X-ray binaries (Nelson et al., 1986). In UCXBs, such as 4U 1820-30, the accretion is believed to be mostly, if not pure, helium (Stella et al., 1987).

Once the accreted matter has reached the neutron star surface, it can "burn" via thermonuclear reactions. Depending on the conditions of the surface layers and the accretion rate, the light elements can burn in steady-state, that is, at the rate at which they are accreted, or alternatively they can accumulate for a time, eventually being rapidly consumed by unstable burning. This unstable form of burning is manifested as a Type I X-ray burst.

1.3 Type I X-ray bursts

Type I X-ray bursts are characterized observationally as bright flashes in X-rays, lasting 10-100 s, and repeating on a timescale of hours to a day. The lightcurves of X-ray bursts show a rapid rise in flux lasting 1 to 5 seconds, followed by a $\sim 10-100$ second-long decay (see Lewin et al. 1993 for a review). In this section, we will describe the various nuclear reactions associated with type I X-ray bursts. We also briefly review the characteristics of the spectral emission during X-ray burst events.

1.3.1 Nuclear burning

As mentioned in the previous section, type I X-ray bursts are powered by the unstable burning of hydrogen and helium accreted from a low-mass companion. The main reaction by which helium is burned is the triple-alpha reaction, which occurs in two phases. Firstly, two α particles will bind to make ^{8}Be, an unstable isotope which has a lifetime of only 2.6×10^{-16} s (Clayton, 1968). At high temperatures ($\gtrsim 10^8$ K), the production of ^{8}Be will be fast enough to create a sufficient amount of ^{8}Be for the second phase of the reaction to occur; $^{8}\mathrm{Be}(\alpha, \gamma)^{12}\mathrm{C}^{\star}$, where $^{12}\mathrm{C}^{\star}$ is an excited state of ^{12}C. The $^{12}\mathrm{C}^{\star}$ nucleus can either decay back into ^{8}Be by releasing an alpha particle, or emit a γ-ray and settle to the ground state of ^{12}C.

The reaction rate of triple-α burning would be small if not for the existence of a particular resonant reaction energy. In the second part of the reaction, $^{8}\mathrm{Be}+\alpha$ has almost the same energy as $^{12}\mathrm{C}^{\star}$, enabling a larger than expected production of carbon. In fact, from the study of relative abundances of ^{12}C in stellar atmospheres, Fred Hoyle predicted the existence of this excited state (Hoyle, 1954).

Hydrogen burning can proceed via a few different versions of the CNO cycle, and at sufficiently high temperatures, by the rp-process. The CNO cycles consist of four proton captures onto isotopes of carbon, nitrogen and oxygen (as well as fluorine in some minor branches) interspersed with inverse beta (or positron) decays, ending with the release of an alpha particle (Bethe, 1939). Since the CNO elements are produced and destroyed at the same rate in these reactions, they effectively act as catalysts. The main branch of the the *cold* CNO cycle is as follows (Hansen et al., 2004):

$$
\begin{aligned}
{}^{12}\mathrm{C} + p &\longrightarrow {}^{13}\mathrm{N} + \gamma \\
{}^{13}\mathrm{N} &\longrightarrow {}^{13}\mathrm{C} + \mathrm{e}^{+} + \nu_e \\
{}^{13}\mathrm{C} + p &\longrightarrow {}^{14}\mathrm{N} + \gamma \\
{}^{14}\mathrm{N} + p &\longrightarrow {}^{15}\mathrm{O} + \gamma \\
{}^{15}\mathrm{O} &\longrightarrow {}^{15}\mathrm{N} + \mathrm{e}^{+} + \nu_e \\
{}^{15}\mathrm{N} + p &\longrightarrow {}^{12}\mathrm{C} + \alpha
\end{aligned}
$$

There are minor branches of the CNO cycle which can occur if in the final step, the reaction instead proceeds as ${}^{15}\mathrm{N}(p,\gamma){}^{16}\mathrm{O}$, where the initially excited state of ${}^{16}\mathrm{O}^{\star}$ eventually gamma decays. This will be followed by a proton capture to make ${}^{17}\mathrm{F}$, thereby breaking out of the main CNO cycle branch. The cold CNO cycle is regulated by the rate at which protons are captured, particularly the slowest of these reactions, ${}^{14}\mathrm{N}(p,\gamma){}^{15}\mathrm{O}$. Since the rate of proton captures is temperature sensitive, the cold CNO cycle energy generation rate increases with temperature. When a temperature of $\sim 8 \times 10^{7}\,\mathrm{K}$ is reached, the rate saturates as the proton captures become much faster than the beta decays, which now limit the rate at which the cycle can operate. This forms a slightly altered CNO cycle, called the *hot* CNO cycle, whose main branch is as follows (Wiescher et al., 2010):

$$
\begin{aligned}
{}^{12}\mathrm{C} + p &\longrightarrow {}^{13}\mathrm{N} + \gamma \\
{}^{13}\mathrm{N} + p &\longrightarrow {}^{14}\mathrm{O} + \gamma \\
{}^{14}\mathrm{O} &\longrightarrow {}^{14}\mathrm{N} + \mathrm{e}^{+} + \nu_e \\
{}^{14}\mathrm{N} + p &\longrightarrow {}^{15}\mathrm{O} + \gamma \\
{}^{15}\mathrm{O} &\longrightarrow {}^{15}\mathrm{N} + \mathrm{e}^{+} + \nu_e \\
{}^{15}\mathrm{N} + p &\longrightarrow {}^{12}\mathrm{C} + \alpha
\end{aligned}
$$

In the hot CNO cycle, ${}^{13}\mathrm{N}$, before having time to β-decay down into ${}^{13}\mathrm{C}$, will quickly capture a proton. The waiting points for the hot CNO cycle are the beta decays of ^{14}O and ^{15}O, with half-lives of 71 and 122 seconds, respectively. Similarly to the cold CNO cycle, the hot CNO cycle can also break out into minor branches if the last reaction results in the formation of stable ^{16}O. At temperatures above $\simeq 5 \times 10^8$ K, α-captures onto ^{14}O and ^{15}O nuclei will break out of the hot CNO cycle, forming the seed nuclei for proton captures in the rp-process (Wallace & Woosley, 1981; Schatz et al., 1999).

The rp-process consists of a long sequence of proton captures and beta decays, creating proton-rich nuclei near the proton drip line, and producing heavy nuclei up to Tellurium (Schatz et al., 2001). The thermal time at depths relevant to X-ray bursts is ~ 10 s, which implies that burst luminosities are expected to decay on this timescale. However, the slow β-decays in the rp-process prolong the energy release during a burst, which is manifested as a noticeable delay in cooling of the lightcurve lasting ~ 100 seconds following the burst peak.

Freshly accreted fuel undergoes a thermal runaway via the *thin-shell instability*. This process was first discovered by Schwarzschild & Härm (1965) by modelling the helium layer residing above a carbon/oxygen core of evolved solar-mass stars. If a shell in hydrostatic balance is sufficiently thin, a temperature change will not affect the pressure at its location, which is set by the weight of the matter above it. If in this shell the nuclear heating rate becomes more temperature-sensitive than the cooling rate, then it can be shown that any temperature perturbation will cause a thermal runaway, leading to a rapid thermonuclear burning of the accreted fuel layer (see chapter 4 for more details). This is the accepted mechanism for the unstable burning which powers X-ray bursts, with either hydrogen or helium burning driving the instability.

For hydrogen to ignite the layer, it must be burning via the cold CNO cycle, which has a temperature dependence in the rate of proton captures. For accretion rates of $\dot{M} < 0.01\dot{M}_{Edd}$ (where we take the Eddington accretion rate to be $\dot{M}_{Edd} = 1.7 \times 10^{-8} M_{\odot}\,\mathrm{yr}^{-1}$), the temperature in the accretion layer will be $T \lesssim 8 \times 10^{7}\,\mathrm{K}$, and hydrogen burning will be in the cold CNO cycle regime, which can burn unstably, leading to "hydrogen-triggered" bursts (Fujimoto et al. 1981 or Cumming 2004 for a review).

If the accretion rate is larger than $\dot{M} \approx 0.01\dot{M}_{Edd}$, hydrogen will burn stably via the hot CNO cycle. If the accretion rate is also below $0.05\dot{M}_{Edd}$, then bursts will occur with a long enough recurrence time that almost all the accreted hydrogen will have burned to helium by the hot CNO cycle. In this case, bursts will be triggered by unstable triple-alpha burning in a pure helium layer. If the accretion rate is larger than $0.05\dot{M}_{Edd}$, the depletion of hydrogen will be prevented by the shortened recurrence times for bursts. In this scenario, helium will still be the trigger for bursts, but the ignition will take place in an environment where hydrogen is present. This is called the mixed H/He burst regime, whose bursts show lightcurves having the long tails associated with rp-process burning of hydrogen. An example of this bursting regime is displayed by GS $1826-24$, a source which is the focus of chapters 2 and 3. At accretion rates larger than $\sim \dot{M}_{Edd}$, both hydrogen and helium are expected to burn stably, implying that no bursts will occur. The exact accretion rate at which the transition to stable burning occurs is not precisely known, and is sensitive to the flux emerging from below the burning layer, which can stabilize the burning (Bildsten, 1998). This topic will be explored in more detail in chapter 4.

Pure helium bursts can also occur in sources which accrete hydrogen-deficient matter. Bursts which occur in a pure helium layer will often be very bright, due to the rapid nature of triple-alpha reactions, and their lightcurves will also decay very rapidly from the lack of rp-process burning in the tail. Such bright bursts often give rise to photospheric radius expansion (PRE), where the burst flux exceeds the local Eddington limit, pushing the photosphere outwards (Hoffman et al., 1980).

A very rare class of X-ray bursts, called superbursts, are believed to be the result of the ignition of a deep layer of carbon. These bursts, which last for many hours, emit energies roughly a thousand times larger than regular type I X-ray bursts (Cumming & Bildsten, 2001a).

1.3.2 Burst spectra

The spectrum of an X-ray burst is typically well-fit by a Planck function, which describes the emission of a perfect blackbody in thermal equilibrium (Lewin et al., 1993). The blackbody spectrum is characterized fully by two parameters; the blackbody normalization, which is the angular size of the observed stellar object, and the blackbody temperature. Type I X-ray burst spectra are consistent with a blackbody normalization of $\sim$ 10km at distances appropriate for the galactic center ($\simeq$10 kpc), and temperatures of $\sim$ 1keV (10^7K). In actuality, while the shape is consistent with a blackbody, the spectrum is expected to be shifted to higher photon energies, or "hardened", by electron scattering and free-free absorption in the neutron star atmosphere. The ratio of the apparent, or colour (also called 'blackbody') temperature of the spectrum, T_c, to the temperature a blackbody would need have to match the total flux, the effective temperature $T_{\rm eff}$, is called the colour correction factor f_c. The values of f_c are believed to have a range of $1.2 - 2.0$, depending on the flux emerging through the surface layer, composition, and surface gravity (Madej, 1974; London et al., 1984, 1986; Ebisuzaki, 1987; Pavlov et al., 1991; Zavlin et al., 1996; Madej et al., 2004; Majczyna et al., 2005; Suleimanov et al., 2012). Note that spectral hardening also implies a decrease in the apparent blackbody normalization. This comes from the requirement that the total integrated flux, $F = (R/d)^2\sigma T^4$ be unchanged by a colour correction to the temperature.

1.4 Probing neutron star interiors with X-ray bursts

In this section, we describe the two main avenues for constraining the interior properties of neutron stars with X-ray bursts. The first is by using X-ray bursts to try to directly constrain the neutron star mass and radius. The second involves measuring the thermal properties of the neutron star.

1.4.1 Measuring neutron star mass and radius with X-ray bursts

Previous works have shown that it is possible to constrain the neutron star mass and radius from observations of Type I X-ray bursts. There have been two leading approaches recently in the literature, both of which focused exclusively on observations of PRE bursts. The first approach involves measuring the flux at the moment that the PRE phase ends, called the "touchdown", and interpreting this flux as being the Eddington flux at the surface of the neutron star. A separate measurement is then made of the blackbody normalization while the burst decays, during which it is assumed that the colour correction factor is a constant. A combination of these two measurements, along with an independent measurement of the distance to the source, yields a quadratic equation which is solved for the mass and radius of the neutron star, typically yielding solutions in two separate lobes (Özel et al., 2009, 2010; Güver et al., 2010a,b). This method is sometimes referred to as the "touchdown method".

A second approach involves a careful calculation of the neutron star burst spectra on a grid of flux, composition, and surface gravity (Suleimanov et al., 2011a, 2012). From these simulated spectra, values of f_c are extracted, which allows for the comparison of the evolution of f_c with diminishing flux, during the decay of a burst. This comparison allows for the measurement of the Eddington flux and the real (as opposed to apparent, or blackbody) normalization R_∞/d, where $R_\infty = R(1+z)$. Again, an independent measurement of the distance is required, which combined with the two previous measurements, yields a quadratic equation which is solved for the mass and radius. This method is called the "cooling tail method" (Suleimanov et al., 2011b).

Some questions have been raised about the different systematic errors that may affect these two approaches (Miller, 2013). For the touchdown method, Steiner et al. (2010) showed that the assumption that the photosphere has returned to the neutron star surface at the touchdown point leads to an overwhelming rejection of solutions, given the distributions of the measured parameters. When the assumption of the touchdown flux being equal to the Eddington flux at the neutron star surface is relaxed, the acceptance rate of solutions increased dramatically. This suggests the possibility of a flawed assumption for the touchdown location, which would cause the measurements of the Eddington flux and blackbody normalization to be inconsistent with a real solution for mass and radius, leading to the rejection of solutions. Among other things, Suleimanov et al. (2011b) also pointed out that, while the colour correction can remain flat for some range of fluxes, there are still significant variations in f_c during burst cooling, particularly at high flux.

Another possible source of systematic uncertainty in these measurements is the choice of bursts to use for analysis. Depending on the accretion rate, the same source can exhibit "short" or "long" PRE bursts. As shown in Suleimanov et al. (2011b), applying the touchdown method to short and long PRE bursts yields very different constraints on mass and radius. Since the cooling tail in "short" PRE bursts shows a normalization which is nearly constant at all fluxes, and are therefore not well reproduced by their spectral models, Suleimanov et al. (2011b) restrict their analysis to only "long" PRE bursts, which are well-fit by their models. Since short PRE bursts are associated with a higher accretion rate, Suleimanov et al. (2011a) argue for the influence of the enhanced accretion in distorting the burst spectra. However, it is not yet clear why the colour correction factor would remain nearly constant throughout the cooling of these short bursts (Kajava et al., 2014).

Furthermore, the two methods described above do not account for the possibly anisotropic emission of radiation during a burst. In Lapidus & Sunyaev (1985), it was shown that this effect can boost or diminish the perceived flux by $1.5 - 2$ relative to the flux from an isotropic source. As we will show in §2.3 of Chapter 2, the burst anisotropy factor ξ_b always appears with the distance d in the combination $\xi_b^{1/2} d$, implying that an uncertainty in ξ_b will affect the measurement of mass and radius in the same way as an uncertainty in the distance to the source. Since it is the angular size $\sim R/d$ of a source that is typically measured with X-ray bursts, this potentially introduces a large uncertainty in the radius measurement.

One approach to constraining the neutron star mass and radius from X-ray bursts that has remained relatively unexplored is the comparison of observed lightcurves to time-dependent multizone calculations. This presents another way to measure the angular size of a source, by determining its intrinsic brightness from simulations. In Heger et al. (2007a), a value for the neutron star radius and redshift was assumed, allowing them to obtain a constraint on the distance to the source GS $1826 - 24$ by comparing lightcurves from their simulations to observations. Without assuming a radius or a redshift, we use this same comparison in §4 of Chapter 2 to obtain a constraint on the mass and radius. The downside of this approach is that these complex simulations are time-consuming.

1.4.2 The thermal state of neutron stars

A second approach to probing neutron star interiors is from their thermal properties, and how these properties influence bursting and cooling behaviour.

Young isolated neutron stars which are passively cooling have been used to constrain the composition of the neutron star core by comparing the observed cooling curves to theoretical simulations that include different modes of neutrino cooling (e.g. Page et al. 2004). Neutron stars in Soft X-ray Transient (SXRT) systems offer a similar opportunity (e.g. Brown et al. 1998; Heinke et al. 2007, 2010). These systems, having episodes of accretion which heat the crust, are then monitored during quiescence to infer their cooling mechanisms.

X-ray bursts are also useful tools to constrain the thermal properties of the neutron star interior (Fujimoto et al., 1987a). The ignition of carbon superbursts depends on the thermal state of the neutron star at column depths of $y \sim 10^{12}\,\mathrm{g\,cm^{-2}}$, which is strongly influenced by the neutrino cooling efficiency in the core and the thermal conductivity of the crust (e.g. Cumming et al. 2006). The ignition of intermediate duration bursts, longer and more energetic bursts resulting from a large helium build-up at column depths of $\sim 10^{10}\,\mathrm{g\,cm^{-2}}$, are similarly influenced.

One common uncertainty in these different approaches to studying the cooling of neutron stars is the amount of heat that is generated inside the neutron star crust or ocean. Theoretical models estimate the emergent flux from the crust to be $\sim 0.05-0.1$ MeV per nucleon (Brown, 2000). There has been growing evidence from a number of studies for a substantially larger, but unknown shallow heat source in the neutron star ocean which is generating a larger flux outwards. Superburst ignition models require temperatures of $\sim 5-6\times10^8$ K to be attained at a column depth of $y \approx 10^{12}\,\mathrm{g\,cm^{-2}}$ in order to match observations, requiring input from an additional heat source (Brown, 2004; Cumming et al., 2006). In the SXRTs KS 1731 − 260 and MXB 1659 − 29, Brown & Cumming (2009) found that the temperatures observed approximately one month into quiescence required an inward flux into the crust, with a corresponding strong shallow heat source. Degenaar et al. (2013) similarly report the presence of a shallow heat source from the rapid cooling of the transient XTE J1709 − 267, after a short $\simeq$10 week outburst. Heinke et al. (2010) show that many transients have elevated quiescent luminosities, near the extremity of what is permitted by low-efficiency neutrino cooling. This may be further evidence of the necessity to include an additional heat source in the modelling of quiescent luminosities. As a final example, for the ultra-compact binary 4U 1820−30, Cumming (2003) inferred that a significant flux from below, $Q_b = 0.4$ MeV per nucleon, was needed to explain the short $\simeq 3$ hours recurrence times. In the same source, in't Zand et al. (2012) also noted that the timescale for the appearance and disappearance of bursts, as the source entered the hard (low accretion rate) or soft state (high accretion rate), was of roughly $\simeq 1$ day. They suggested that this implies the existence of a heat source, shallow enough that it can adjust to the changing accretion rate on a $\sim$1-day timescale.

One possible candiate for this shallow source of heat comes from dissipation caused by differential rotational between the ocean and crust. The differential rotation arises from the large difference in angular velocity between the neutron star and the accreted matter, which moves at Keplerian speeds of $\simeq 0.5c$ near the star surface. This leads to a spin-up of the ocean, which causes heat dissipation at the boundary with the solid outer crust (Inogamov & Sunyaev, 2010).

The nature of the shallow heat source has emerged as a major question in studies of the thermal state of the outer parts of LMXB neutron stars. Understanding the nature of the heat source is crucial if we are to accurately interpret the thermal relaxation of transients or understand the ignition depths of superbursts, which directly affects attempts to constrain the internal temperatures of these neutron stars. In Chapter 4, we study the effect of strong heating on the behaviour of nuclear burning in accreting neutron stars, specifically the stabilization of burning at high temperatures. This offers an alterative approach to constraining the presence and strength of shallow heat sources.

1.5 This thesis

Here, we briefly preview the contents of chapter 2, 3 and 4. We also describe how these chapters address the issues outlined in the previous section.

In the next chapter, we address the issues relating to systematic uncertainties described in §1.4.1 by developing a method for deriving mass and radius constraints which do not depend on the distance to the source, or the anisotropy factor. We apply our method to a very regular burst source, GS $1826-24$. This source has not displayed PRE events, but our approach applies equally to sub-Eddington bursts. Our approach consists, on the one hand, of comparing the observed lightcurve to time-dependent multizone burst simulations. Combined with a measurement of the blackbody normalization, this yields a distance and anisotropy-independent constraint on the gravitational redshift. A second constraint comes from a partial application of the "cooling tail" method, described above, to GS $1826-24$. We show that an upper limit can be placed on R_∞ (the neutron star radius "at infinity", defined as $R_\infty = R(1+z)$, where R is the neutrons star radius, and z is the gravitational redshift), independent of the distance and anisotropy parameter.

Chapter 3 takes a close look at the comparison of simulated to observed lightcurves first shown in Heger et al. (2007a), but also used in Chapter 2. We show that what appears to be a nearly flawless agreement in lightcurve shape at one recurrence time breaks down as the recurrence time is changed. We show that a wider grid of simulations is needed to accurately describe the GS $1826-24$ lightcurves. Since these lightcurve comparisons are a part of the approach to deriving mass and radius constraints which is described in Chapter 2, it is important that the simulations accurately capture the variations in the observed lightcurves. Using a simple empirical law relating the peak flux to the average helium mass fraction in the accreted layer at ignition, we argue that the data can be well-described by a low-metallicity, helium-enriched model. We also rederive upper limits on R_∞ for GS $1826-24$, similarly to Chapter 2, this time using the most recent burst spectra calculations.

In Chapter 4, we attempt to constrain the strength of the shallow heat source in 4U $1820-30$. This source, an ultra-compact binary, is believed to accrete pure helium. We first investigate the stability boundary of pure helium accretion using the MESA stellar evolution code. We calculate the critical accretion rate at which helium burning transitions from stable to unstable, as a function of the heat flux from deeper layers. We interpret these results using a simple one-zone model, and derive analytical formulae for the critical accretion rate, as well as the temperature at which the stability transition occurs. We also investigate whether the critical accretion rate can be determined by examining steady-state models only, without time-dependent simulations. We examine the argument that the stability boundary coincides with the turning point $dy_{\rm burn}/d\dot{m} = 0$ ($y_{\rm burn}$ is the column depth at which helium burning is a maximum) in the steady-state models, and find that it does not hold outside of the one-zone, zero base flux case. A linear stability analysis of a large suite of steady-state models is also carried out, which yields critical accretion rates a factor of ~ 3 larger than the MESA result, but with a similar dependence on base flux. Lastly, we discuss the implications of our results for 4U 1820-30.

We summarize and conclude in Chapter 5.

2

Constraints on Neutron Star Mass and Radius in GS 1826-24 from Sub-Eddington X-ray Bursts

This chapter was published as: M. Zamfir, A. Cumming, D. K. Galloway, *Constraints on Neutron Star Mass and Radius in GS 1826-24 from Sub-Eddington X-ray Bursts.* ApJ, 749, 69, 04/2012.

2.1 Introduction

Thermonuclear flashes from accreting neutron stars, observed as type I X-ray bursts, in principle provide a way to constrain neutron star masses and radii (for a review see §4 of Lewin, van Paradijs & Taam 1993). The large observational catalogues of type I X-ray bursts now available (Galloway et al. 2008; hereafter G08) and new spectral models (Madej, Joss, & Rozanska 2004; Majczyna et al. 2005; Suleimanov, Poutanen, & Werner 2011b) have motivated fresh attempts to do this using photospheric radius expansion bursts (Özel 2006; Özel, Güver, & Psaltis 2009; Güver et al. 2010a, 2010b; Steiner et al. 2010; Suleimanov et al. 2011a, 2011b; Özel, Gould, & Güver 2011). In this approach, the peak luminosity of the burst (specifically at the "touchdown" point when the photosphere returns to the neutron star surface) is related to the Eddington luminosity, and the normalization of the burst spectrum is related to the emitting area. If some information about the distance to the source is available, constraints on the neutron star mass and radius can be derived. These works have highlighted and spurred debate about some of the systematic errors that must be taken into account, such as uncertainty in identifying the moment at which the photosphere touches down (Galloway, Özel, & Psaltis 2008; Steiner et al. 2010; Suleimanov et al. 2011a,b; Güver, Özel & Psaltis 2011), and differences in derived radii when using bursts at different accretion rates from the same source (Suleimanov et al. 2011a,b; Güver, Psaltis, & Özel 2011).

GS 1826-24 is a unique X-ray burster that shows remarkable agreement with theoretical models of recurrence times, energetics, and lightcurves (Galloway et al. 2004; Heger et al. 2007; in 't Zand et al. 2009). The observed recurrence time (typically 3–5 hours) in a given epoch is the same from burst to burst to within a few minutes (Cocchi et al. 2001), and the burst lightcurves in a given epoch are very uniform (Galloway et al. 2004), implying the same conditions on the neutron star surface from burst to burst, and a regular limit cycle. Heger et al. (2007) compared the observed lightcurves to the theoretical models of Woosley et al. (2004). By choosing a model with approximately the same recurrence time as the data, and by varying the distance only (which scales the observed peak flux to match the model peak luminosity), the theoretical lightcurve fit most of the observed lightcurve well, except for deviations during the burst rise and at late times in the cooling tail. This is of great interest because the long ~ 100 second tails of these bursts are powered by the rp-process (Wallace & Woosley 1981), and offer a way to test the nuclear physics input, such as masses of proton rich heavy nuclei and their reaction rates, both of which are usually highly uncertain (e.g. Schatz et al. 1998; Schatz 2006). Even more remarkably, in 't Zand et al. (2009) extracted the observed lightcurve out to more than 1000 seconds by combining multiple bursts. The late time cooling observed matched the late time cooling in the theoretical model of Heger et al. (2007), which arises from heat initially conducted inwards to deeper layers that then emerges on long timescales.

In this chapter, we take the comparison between observations and theory for GS 1826-24 one step further. We first determine the constraints on neutron star mass and radius that can be derived from the lightcurve comparison carried out by Heger et al. (2007). The basic idea here is that even though the X-ray bursts from GS 1826-24 do not reach the Eddington limit, we can still determine the intrinsic luminosity of the bursts by comparing with the lightcurve models. This replaces the touchdown measurement used for PRE bursts with a different condition which we use to constrain M and R for GS 1826-24. In our analysis we take care to include the possible anisotropy in burst and persistent emission and show how that could affect the mass and radius determination. We then compare the spectral evolution during the tail of the burst with spectral models. The good understanding of bursts from GS 1826-24 suggests that they could be a good testing ground for spectral models. We show that in the initial cooling phase following peak luminosity the spectral evolution agrees well with the models of Suleimanov et al. (2011b), and we derive the associated constraints on M and R. In both cases, we look for constraints that are independent of distance and emission anisotropies since neither are well-constrained for GS 1826-24.

The outline of the chapter is as follows. The data analysis is described in §2.2. In §2.3, we discuss the possible anisotropy of the burst and persistent emission and review calculations of the expected degree of anisotropy in the literature. In §2.4, we use the model lightcurve from Heger et al. (2007) to set the luminosity scale of the observed bursts and show that this gives a distance-independent relation between the redshift and color correction factor f_c. Suleimanov et al. (2011a) argued that rather than using a single measurement of touchdown flux, the entire cooling track of the burst should be fit to spectral models. We do this in §2.5, and show that even though the peak flux is below Eddington, the fits provide a constraint on the value of F_{Edd} as well as the normalization of the spectrum. These two measurements translate into a distance independent upper limit on R_∞. We compare these two different constraints and discuss their implications in §2.6.

2.2 Data Analysis

We used data taken with the Proportional Counter Array (PCA; Jahoda et al. 1996) onboard the Rossi X-ray Timing Explorer (RXTE), from the catalogue of bursts detected over the mission lifetime (G08). Where not explicitly stated, the data analysis procedures are as in G08. Time-resolved spectra in the range 2-60 keV covering the burst duration were extracted on intervals as short as 0.25 s during the burst rise and peak, with the bin size increasing step-wise into the burst tail to maintain roughly the same signal-to-noise level. A spectrum taken from a 16-s interval prior to the burst was adopted as the background.

We re-fit the spectra over the energy range 2.5-20 keV using the revised PCA response matrices, v11.7[1], and adopted the recommended systematic error of 0.5%. The fitting was undertaken using XSPEC version 12. In order to accommodate spectral bins with low count rates, we adopted Churazov weighting. We modelled the effects of interstellar absorption, using a multiplicative model component (`wabs` in XSpec), with the column density N_H frozen at 4×10^{21} cm^{-2} (e.g. in 't Zand et al. 1999). In the original analysis carried out by G08, the neutral absorption was determined separately for each burst, from the mean value obtained for spectral fits carried out

[1]see http://www.universe.nasa.gov/xrays/programs/rxte/pca/doc/rmf/pcarmf-11.7

with the N_H value free to vary. This has a negligible effect on the fluxes, but can introduce spurious burst-to-burst variations in the blackbody normalisation.

The burst data used here has been corrected for "deadtime", a short period of inactivity in the detectors following the detection of a X-ray photon. There are however concerns regarding the absolute flux calibration of the PCA associated with variations in the flux from the Crab nebula and the effective area of the PCA. We will show that such absolute uncertainties will not influence our derived constraints.

2.3 Anisotropy of the burst and persistent emission

The possibility that the burst or persistent emission is not isotropic has been long discussed (e.g. Lapidus et al. 1985), but has not always been included in recent work using X-ray bursts to constrain neutron star mass and radius. For example, in Özel (2006), Steiner et al. (2010), and Suleimanov et al. (2011a) the burst emission is assumed to be isotropic. Here, we review the expected size of the anisotropy. We follow Fujimoto (1988) and define an anisotropy parameter ξ by the relation $4\pi d^2 F\xi = L$ between the observed flux F and the luminosity of the source L over the whole sky, where d is the distance to the source. When $\xi < 1$ (> 1), the radiation is beamed towards (away from) the observer. We write the anisotropy factor for the burst and persistent emission as ξ_b and ξ_p respectively.

Lapidus, Sunyaev & Titarchuk (1985) showed that if the accretion disk extends to the neutron star surface during the flash, it will intercept $\approx 1/4$ of the radiation from the burst, reflecting it preferentially along the disk axis. They provide the approximate expression

$$\xi_b^{-1} = \frac{1}{2} + |\cos i| \tag{2.1}$$

where i is the inclination angle ($i = 0°$ means the system is viewed face on, looking down the disk axis), which closely fits their more detailed results derived from solving the radiative transfer equations for a disk geometry (they found a maximum value of 1.39 rather than 1.5). The range of ξ_b^{-1} is from 0.5 (edge on) to 1.5 (face on), implying an uncertainty of a factor of 3 depending on inclination angle.

The anisotropy factor for the persistent emission is perhaps even more uncertain than that for the burst flux, depending on the specific model for the inner accretion disk, boundary layer, and corona etc. Lapidus et al. (1985) and Fujimoto (1988) derive opposite behaviors for the factor ξ_p as a function of inclination. The model presented in Fujimoto (1988) for the persistent emission assumes that radiation from the boundary layer, which encircles the neutron star in a "belt" about its equator, is largely screened by the inflated inner part of the accretion disk and scattered preferentially in a direction along the disk axis. In Lapidus et al. (1985), however, the inner part of the disk is assumed to be thin, and less than one half of the boundary layer radiation falls on the accretion disk and is re-scattered, again preferentially along the disk axis, while the remainder of the emission is beamed preferentially in the direction $i = 90°$ (along the plane of the disk). This difference in their modelling of the inner accretion disk is made apparent by fact that, while Fujimoto (1988) predicts no radiation to be emitted in the $i = 90°$ direction, Lapidus et al. (1985) find a substantial portion of the persistent emission will be beamed in that direction. The ratio ξ_p/ξ_b varies by up to a factor of $\sim$3 with inclination for both models, although while Fujimoto (1988) finds that the ratio is monotonically increasing with inclination, Lapidus et al. (1985) find the opposite trend. We note that these two models do not consider the effects of general relativity on the trajectories of photons near the neutron star surface. However, Lapidus et al. (1985) show that when considering this effect, a substantially larger proportion ($\sim$ 28% for a ratio of the neutron star radius to the Schwarzschild radius R/r_s of 3) of radiation falls on the accretion disk, further enhancing beaming along the disk axis.

The definition of ξ is such that it always appears with distance d in the combination $\xi^{1/2}d$. Therefore, the uncertainty in anisotropy factor acts in the same way as an additional uncertainty in the distance to the source. For GS 1826-24, Homer et al. (1998) suggest a limit $i < 70^\circ$ based on the low amplitude of the optical modulation at the orbital frequency, in which case equation (2.1) gives $0.84 \lesssim \xi_b^{-1} \lesssim 1.5$, or $0.85 < \xi_b^{1/2} < 1.1$. Therefore even if the distance to GS 1826-24 was perfectly known, anisotropy of the burst emission would represent an uncertainty of about $\pm 15\%$ in any quantity that depends on distance. For example, using spectral fits to determine R_∞ is subject to this uncertainty since the normalization of the spectrum depends on the solid angle $R_\infty^2/d^2\xi$. Given these uncertainties, in this chapter we look for constraints on M and R that are independent of distance and anisotropy.

2.4 Comparison between the observed and model burst lightcurves

We first ask what constraints on M and R arise from the comparison between the observed lightcurve and theoretical models of Heger et al. (2007). Photospheric radius expansion (PRE) bursts are often used in work to constrain neutron star properties from X-ray bursts, because the peak luminosity of the burst can then be taken to be the Eddington luminosity. This cannot be done for GS 1826-24 because the bursts do not show PRE, implying that they have a peak luminosity below Eddington. Instead, here we pursue the idea that the model lightcurves which fit the observed lightcurves so well tell us the peak luminosity of the bursts.

Heger et al. (2007) selected from their models one that had a similar recurrence time to the observed bursts in 2000 (the model had $t_{\rm recur} = 3.9$ hr as opposed to the observed $t_{\rm recur} = 4.07$ hr). They showed that, when the distance to GS 1826-24 (actually $\xi_b^{1/2} d$) is chosen to make the predicted peak flux match the observed lightcurve, the theoretical and observed burst lightcurves show remarkable agreement. They considered fixed values of M and R, but the choice of those two parameters also changes the mapping between observed and model burst fluxes. Therefore, rather than vary distance alone, we find the value of the ratio of the observed flux to the model flux

$$\frac{F_{\rm obs}}{F_{\rm model}} = \xi_b^{-1} \left(\frac{R}{d}\right)^2 \frac{1}{(1+z)^2} \tag{2.2}$$

that gives the best fit between the model and the data. Taking the peak values, $F_{\rm model,pk} = 1.29 \times 10^{25}$ erg cm^{-2} s^{-1} (computed from the redshifted peak luminosity quoted in Heger et al. 2007, with $R = 11.2$ km and $z = 0.26$) and $F_{\rm obs,pk} = 2.84 \times 10^{-8}$ erg cm^{-2} s^{-1}, we find $F_{\rm obs}/F_{\rm model} = 2.20 \times 10^{-33}$. Substituting this value into equation (2.2), we find

$$\frac{R}{\xi_b^{1/2} d} = 10.9 \text{ km}/6.0 \text{ kpc} \, \frac{1+z}{1.26} \left(\frac{F_{\rm obs}/F_{\rm model}}{2.2 \times 10^{-33}}\right)^{1/2}, \tag{2.3}$$

where we use the redshift assumed by Heger et al. (2007). Note that the model lightcurve is likely to be insensitive to the model gravity, so that the ratio $F_{\rm obs}/F_{\rm model}$ does not depend sensitively on the M and R used in the model. For example, the ignition column depth is weakly dependent on gravity in this burning regime (Bildsten 1998 derives $y_{\rm ign} \propto g^{-2/9}$). However, this is something that should be explored in further simulations. For now, we assume $F_{\rm obs}/F_{\rm model}$ is a constant, and take equation (2.3) as a joint constraint on R and $1+z$.

The theoretical uncertainty in $F_{\rm model}$ is at present unknown. The predicted lightcurves depend on the input nuclear physics, and prescription for convection and other mixing processes for example. These prescriptions vary from code to code, and currently only simulations from the KEPLER code (Woosley et al. 2004) have been compared to the observations of GS 1826-24. Further simulations and comparisons are required to determine what range of predicted peak fluxes still produce lightcurves with the correct shape to fit the data. For now, in order to put an error bar on the prefactor in equation (2.3), we assume that the theoretical uncertainty in $F_{\rm obs}/F_{\rm model}$ is $\pm 10\%$, and keep in mind the fact that this number is uncertain.

This raises the point that rather than use the peak flux only, we could also fit the entire lightcurve. In that case there is an extra parameter, the redshift $1 + z$ which stretches the lightcurve in time. In principle, this provides a constraint on $1 + z$. In practice, however, we find that the value of $1 + z$ obtained in the fit is sensitive to how much of the lightcurve is included in the fit. For example, fitting the entire lightcurve (until about 130s after the peak) we find best-fit values $1+z = 1.44$, $F_{\rm obs}/F_{\rm model} = 2.10 \times 10^{-33}$. If we fit the first 30 seconds only, which includes only the initial decline after the peak rather than the whole tail, we get a best fit of $1+z = 1.32$ and $F_{\rm obs}/F_{\rm model} = 2.17 \times 10^{-33}$. We show in Figure 2.1 the separate fits to the entire lightcurve and the first 30 seconds, and we also include the model lightcurve fitted only by matching the peak fluxes, with the value for the redshift of $1 + z = 1.26$, as assumed by Heger et al. (2007) . We see that while the redshift is sensitive to the details of the fitting, the normalization $F_{\rm obs}/F_{\rm model}$ is well-determined. Therefore, here we use the normalization, but leave fits to the shape of the entire lightcurve to future work when a greater number of simulations are available.

A second constraint comes from spectral fitting. Fitting the observed burst spec-

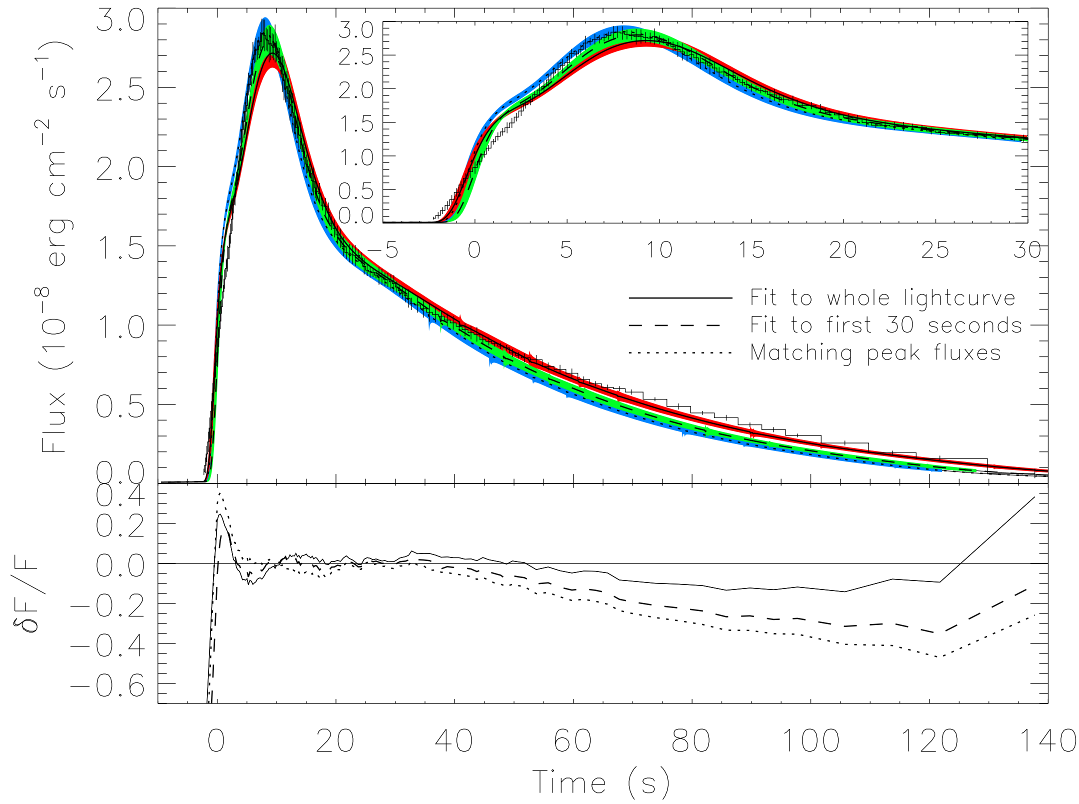

Figure 2.1 The average burst profiles with $t_{\rm recur} = 4.07$ hr compared with three separate fits of the mean theoretical model lightcurve from Heger et al. (2007) (model A3 which had a similar recurrence time) is shown in the upper plot, with an inset showing only the first 30 seconds. The model has been fit to the data by varying the overall normalization, start time, and redshift. The solid (with red band) and dashed (with green band) lines represent the fits to the entire lightcurve and the first 30 seconds, respectively, and the dotted line (with blue band) represents the lightcurve fitted only by matching the peak fluxes with a fixed redshift of $1+z = 1.26$. The bands show the range of luminosity variations from burst to burst in the theoretical model. The lower plot shows the difference between each of the fits and the average observed lightcurve, with a horizontal solid line at $\delta F/F = 0$ for clarity.

trum with a blackbody gives the total flux F_∞, color temperature $T_{c,\infty}$, and the blackbody normalization

$$K = \left(\frac{F_\infty}{\sigma T_{c,\infty}^4}\right) = \frac{R_\infty^2}{d^2 f_c^4}\xi_b^{-1}. \tag{2.4}$$

The color correction factor $f_c = T_c/T_{\rm eff}$ takes into account the hardening of the burst spectrum compared to a blackbody at the same effective temperature $T_{\rm eff}$. We plot K as a function of time in Figure 2.2 for two average burst profiles, for recurrence times 5.74 and 4.07 hr respectively. Following the burst rise, which lasts for approximately 5 seconds, the normalization levels off until ≈ 60 seconds into the burst, when the normalization drops dramatically over 100 seconds to only about 25% of its original value. We discuss the variation of K in the tail, and the difference in K for the two different recurrence times in the next section. For our purposes here we find the mean value of K for the $t_{\rm recur} = 4.07$ hr profile during the period following the peak where it is constant, giving $K = 110 \pm 2$ (km/10 kpc)^2. If we take into account the deadtime correction near the burst peak ($\approx 6\%$), the value we find is consistent with the more detailed analysis of blackbody normalization in these bursts carried out by Galloway & Lampe (2011).

Dividing equations (2.2) and (2.4), R/d and ξ_b drop out, giving

$$\begin{aligned} \frac{f_c}{1+z} &= K^{-1/4}\left(\frac{F_{\rm obs}}{F_{\rm model}}\right)^{1/4} & (2.5)\\ &= 1.17\left(\frac{K}{110\ ({\rm km/10kpc})^2}\right)^{-1/4}\left(\frac{F_{\rm obs}/F_{\rm model}}{2.2\times10^{-33}}\right)^{1/4}. & (2.6)\end{aligned}$$

We show model calculations of f_c from Suleimanov et al. (2011b) in the next section which typically have $f_c \approx 1.4$–1.5 during the phase where K is relatively constant. For $f_c = 1.4, 1.5$ we get $1 + z = 1.19, 1.28$. Note that as well as being independent

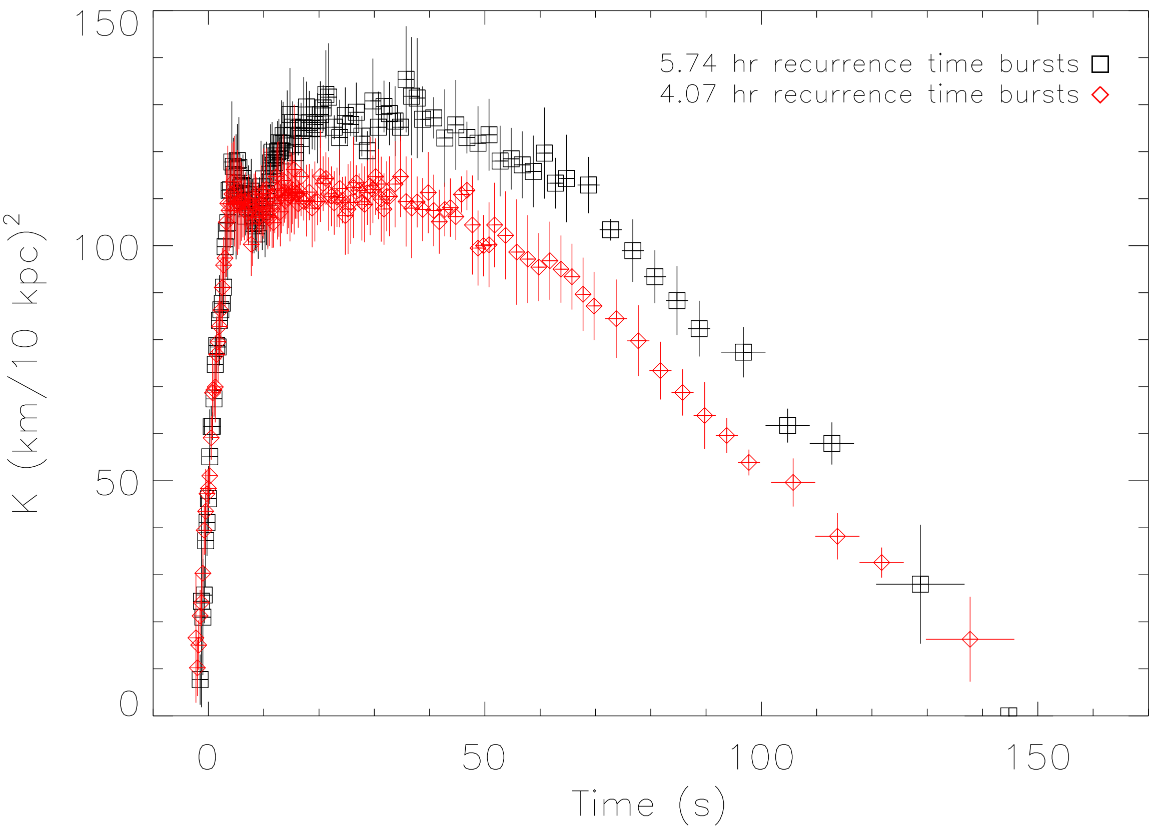

Figure 2.2 Blackbody normalization for average burst profiles with $t_{\rm recur} = 5.74$ (black squares) and 4.07 hr (red diamonds).

of d and ξ_b, the value of $1 + z$ determined in this way is not very sensitive to the values of K and $F_{\rm model}/F_{\rm obs}$ (proportional to the 1/4 power of each). For example, introducing an uncertainty in $F_{\rm model}/F_{\rm obs}$ of $\pm 10\%$ gives a prefactor in equation (2.9) of 1.17 ± 0.03 or $1 + z = 1.28 \pm 0.03$ $(f_c/1.5)$.

There is one more constraint which comes from the agreement between the measured and model recurrence times, which effectively measures the local mass accretion rate $\dot{m}$ onto the star. We define $\dot{m}$ to be the rest mass accretion rate at the stellar surface. Then the accretion flux as observed at infinity is

$$F_X = \dot{m} \left(\frac{R}{d}\right)^2 \xi_p^{-1} \frac{c^2 z}{(1+z)^2}. \tag{2.7}$$

Dividing equations (2.2) and (2.7) gives the observed quantity

$$\frac{F_X}{\dot{m}c^2}\frac{F_{\rm model}}{F_{\rm obs}} = \left(\frac{\xi_b}{\xi_p}\right) z, \tag{2.8}$$

a direct measure of redshift, independent of distance, but dependent on the anisotropy parameter ratio ξ_p/ξ_b. The accretion rate in model A3 of Heger et al. (2007) was $\dot{m} = 7980\ {\rm g\ cm^{-2}\ s^{-1}}$, and the measured persistent flux in 2000 was $F_X = 2.91 \pm 0.03 \times 10^{-9}\ {\rm erg\ cm^{-2}\ s^{-1}}$, giving

$$z = 0.18 \pm 0.02\ \left(\frac{\xi_p}{\xi_b}\right). \tag{2.9}$$

An alternative way to derive this result is to match the theoretical α value, the ratio of persistent fluence between bursts to burst fluence, to the observed value. The models of Heger et al. (2007) with recurrence time of 4 hours have a theoretical value $\alpha_{\rm model} = \Delta M c^2 z_{\rm model}/E_{\rm burst}(\xi_b/\xi_p) = 55\ (\xi_b/\xi_p)$, where $E_{\rm nuc}$ is the burst energy, ΔM the ignition mass, and a redshift $z_{\rm model} = 0.26$. The observed α at the same recurrence time is $\alpha_{\rm obs} \approx 37$ (Fig. 2 of Heger et al. 2007), giving $z = z_{\rm model}(\alpha_{\rm obs}/\alpha_{\rm model}) = 0.17(\xi_p/\xi_b)$, in agreement with the value in equation (2.9).

If the anisotropy parameters were known, equations (2.9), (2.2) and (2.4) uniquely determine the three quantities $1+z$, f_c and R/d. However, as noted in §2.3, the anisotropy parameters are not well-constrained. In particular, equation (2.9) for the redshift is not constraining once the large uncertainty in ξ_p/ξ_b is taken into account. The main result of this section is therefore the relation between $1+z$ and f_c in equation (2.5), since it is independent of d and ξ_b.

In the next section, we constrain the Eddington flux by fitting the burst cooling tracks to spectral models. We can use the model lightcurve to say something about the expected value of $F_{\rm Edd}$, the observed flux which corresponds to the Eddington flux at the surface of the star. In the model the Eddington flux locally is $F_{\rm Edd} = cg/\kappa = 0.882\times 10^{25} g_{14}$ erg cm^{-2} s^{-1} for $X = 0.7$, giving $F_{\rm model,pk}/F_{\rm model,Edd} = 1.46/g_{14}$. Scaling the observed peak flux, the Eddington flux as observed at infinity should be $1.95\times 10^{-8} g_{14}(1.7/1+X)$ erg cm^{-2} s^{-1}, or $F_{\rm Edd}/(10^{-8}\ {\rm erg\ cm^{-2}\ s^{-1}}) = 1.95, 3.89, 7.79$ for $\log_{10} g = 14.0, 14.3, 14.6$.

2.5 Comparison with spectral models

We now turn to fitting theoretical calculations of the color-correction factor f_c to the data. First we describe the fitting procedure and results (§2.5.1) and then the constraints on neutron star parameters, in particular an upper limit on R_∞ (§2.5.2). In §2.5.3 we discuss the variation of K with accretion rate (Fig. 2.2) in the context of the spectral models.

2.5.1 Fit for A and $F_{\rm Edd}$

Suleimanov et al. (2011b) calculated f_c as a function of $F/F_{\rm Edd}$ for a range of surface gravities and atmospheric compositions, and discussed how these models could be applied to data. We follow their analysis, and fit the theoretical f_c-$F/F_{\rm Edd}$ curves to the observed relation between $K^{-1/4}$ and flux F. The fitting parameters are $F_{\rm Edd}$ and $A = K^{-1/4}/f_c$. Comparing with equation (2.4), we see that

$$A = \left(\frac{R_\infty}{d}\right)^{-1/2} \xi_b^{1/4}. \tag{2.10}$$

If f_c was a constant independent of flux, and K was constant in the cooling tail of the burst, fitting for A would be equivalent to using the measured normalization K

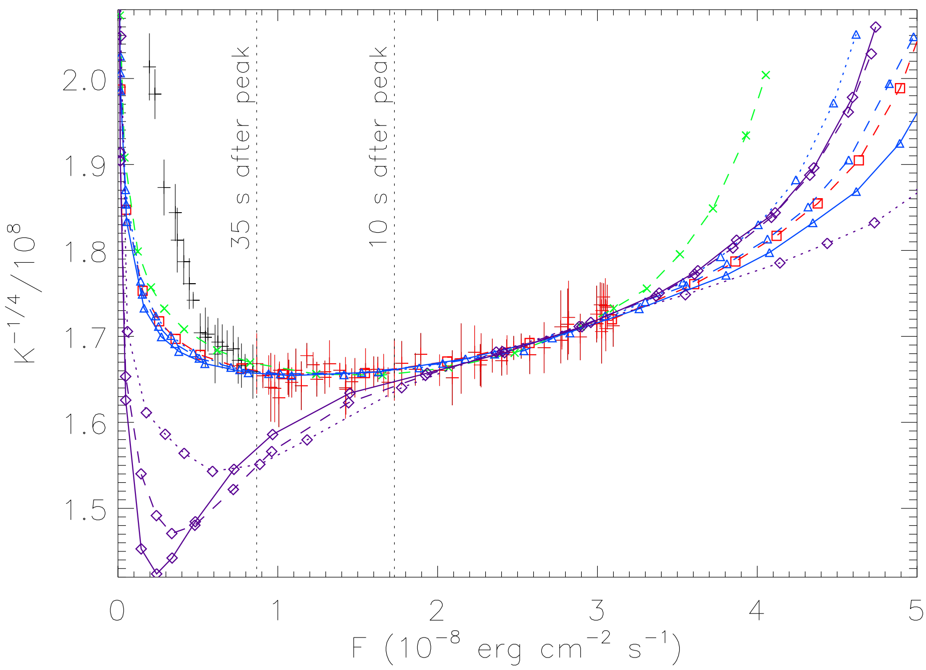

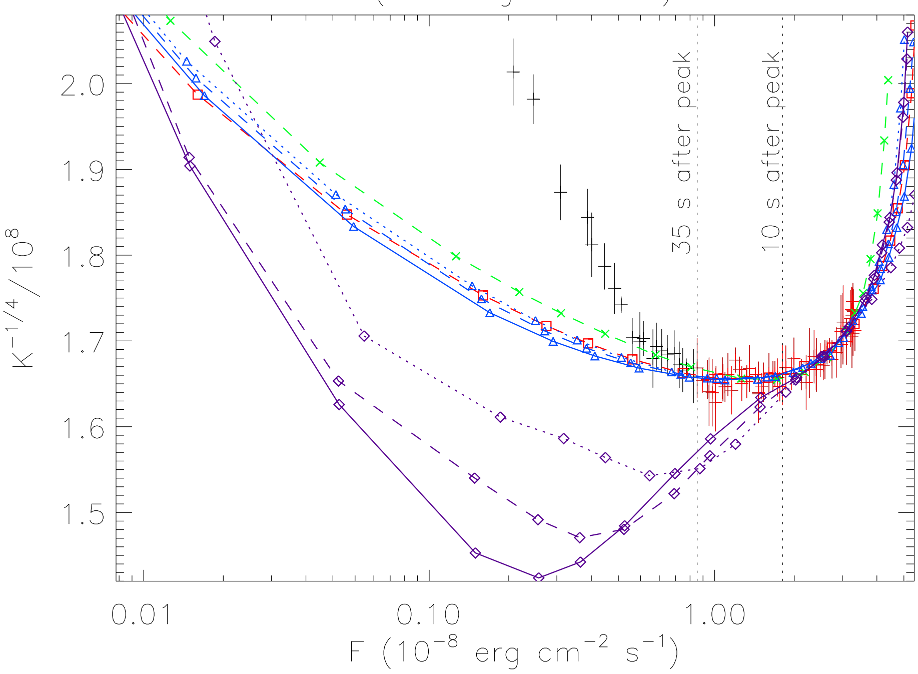

Figure 2.3 Best fits to the theoretical $f_c - F/F_{\rm Edd}$ curves for a range of compositions. The crosses represent the all the data points from the burst peak onwards, and those in red representing only the first 35 seconds after the peak. Two vertical dotted lines represent the fluxes at $t = 10, 35\,\rm s$ after the burst peak. The compositions are solar H/He abundance with solar metallicity (diamonds connected by purple lines) or 1% solar metallicity (triangles, blue lines), pure H (squares, red line) and pure He ($\times$ symbols, green line). Dotted, dashed and solid lines represent surface gravities of $\log_{10}(g) = 14.0$, 14.3 and 14.6, respectively.

and a value of f_c to extract R_∞/d. Instead, here we are using the entire cooling track to obtain A. In addition, by fitting the shape of the cooling track we can obtain the overall flux scale $F_{\rm Edd}$ even though the burst itself does not reach Eddington luminosity.

We start by fitting the data from GS 1826-24 with recurrence time 5.74 hr to the different models from Suleimanov et al. (2011b). Below we use the fits to obtain an upper limit on R_∞, which motivates us to start with the bursts with the largest value of K and therefore larger R_∞ values. At the end of this section, we discuss whether it is possible to include the 4.07 hr recurrence time bursts which have smaller values of K (Fig. 2.2) in a consistent picture. When fitting, for simplicity we calculate χ^2 based on comparing $K^{-1/4}$ and f_c, and do not include the errors in the flux measurement. This seems reasonable because the observational error in the overall flux scale is $\approx \delta F/\sqrt{N}$, where the individual flux error $\delta F \approx 10^{-9}$ erg cm^{-2} s^{-1}, smaller than the overall uncertainty in the parameter $F_{\rm Edd}$ that we obtain from our fits.

Suleimanov et al. (2011b) calculate spectral models for pure H and pure He atmospheres, and solar H/He fractions with different metallicity. Based on the lightcurve comparison and energetics, Galloway et al. (2004) and Heger et al. (2007) concluded that the accreted layer has solar metallicity and a substantial amount of hydrogen (a solar H/He ratio in their models). Here we fit to the full range of models from Suleimanov et al. (2011b) to investigate how changing composition affects our derived limits on neutron star parameters. Also, the photospheric abundances could be different from the abundances near the base of the layer where the X-ray burst ignites. For example, the metallicity in the burning layer could be enhanced by partially burned fuel left over from a previous burst. The hydrogen fraction in the accreted material could be lower than solar, and so it is useful to consider the pure He limit as a limiting case when the hydrogen fraction at the photosphere is reduced.

Figure 2.3 shows example fits to the 5.74 hr recurrence time bursts. By varying A and $F_{\rm Edd}$, we are able to obtain good fits for fluxes down to approximately 1/3 of the peak flux. At lower fluxes, the behavior of the model and observations is qualitatively similar, in that f_c rises rapidly at low fluxes, but the detailed behavior does not match the models. At late times or low fluxes, $K^{-1/4}$ rises more rapidly than predicted. We therefore confine the fit to the initial part of the cooling tail and use it to derive A and $F_{\rm Edd}$. To do this, we fit $\Delta t_{\rm fit}$ seconds of data starting at the time of peak flux. The time $\Delta t_{\rm fit}$ is chosen so that as much data is included in the fit as possible while still giving an adequate fit (with the late time data excluded, we find reduced χ^2 values in the range 0.23–0.47 for the models listed in Table 2.1). For all except the solar metallicity models we take $\Delta t_{\rm fit} = 35$ s, corresponding to fluxes down to $\approx 1/3$ of the peak flux. The solar metallicity models begin to deviate from the data after $\Delta t_{\rm fit} = 10$ s (about 1/2 of the peak flux) because of the dip in f_c at low fluxes.

The results of the fits for different spectral models are listed in Table 2.1. We used Markov Chain Monte Carlo implemented with the Metropolis-Hastings algorithm (Gregory 2005, Chap. 12) to sample the parameter space and find the distributions for the fitting parameters, A and $F_{\rm Edd}$. Those distributions were then each fitted by a Gaussian profile in order to derive their respective central values and 1σ uncertainties. In certain cases, as noted in Table 2.1, the distributions were not well described by a single Gaussian profile, due to the presence of more than one peak. In those cases, we fit a Gaussian profile to the peak at the lowest values of $F_{\rm Edd}$ and A. Note that these parameters are correlated since an increase (decrease) in A, which moves the model curves upwards (downwards) with respect to the observations, can be offset by a corresponding increase (decrease) in $F_{\rm Edd}$ which moves the curves rightwards (leftwards). The range of $F_{\rm Edd}$ for all the fitted models is from 4.1 to 7.4×10^{-8} erg cm^{-2} s^{-1}, which lies within the range of $F_{\rm Edd}$ from the Heger et al. (2007) models used in section §2.4. Excluding the $0.1Z_\odot$, $\log_{10} g = 14.0$ model, the range of $F_{\rm Edd}$ is relatively narrow; 4.1 to 5.9×10^{-8} erg cm^{-2} s^{-1}.

The behavior at low fluxes is shown in more detail in the second panel of Figure 2.3 which has a logarithmic flux axis. The slope of the increase in f_c with decreasing flux is steeper in the data than in the models for low metallicity models. For solar metallicity models, the slopes are similar. This would enable a good fit of the whole data set to those models, particularly at low fluxes, but only if $F_{\rm Edd}$ is in the range 15–25×10^{-8} erg cm^{-2} s^{-1}. In fact, even with the restriction of using only 10 seconds of data following the burst peak we found other adequate fits, as separate local χ^2 minima, in that range of $F_{\rm Edd}$. This is much larger than expected and as can be seen from the relations derived below, would give very small limits on R_∞, and so we do not consider these fits further.

2.5.2 Upper limit on distance and R_∞

A measurement of A and $F_{\rm Edd}$ translates into typically two values for M and R as follows. When the flux at the surface of the star is at the local Eddington flux cg/κ, the observed flux is

$$F_{\rm Edd} = \frac{GMc}{\kappa d^2}\frac{1}{1+z}\xi_b^{-1}, \tag{2.11}$$

where we take the opacity to be $\kappa = 0.2$ cm^2 g^{-1} $(1 + X)$, as used in Suleimanov et al. (2011b). Following Steiner et al. (2010) we define the quantities

$$\alpha \equiv \frac{\kappa d}{c^3} F_{\rm Edd} A^2 \xi_b^{1/2} = \frac{u}{2}(1-u) \tag{2.12}$$

Table 2.1. Fits of spectral models to the burst cooling tail

Composition	$\log_{10} g$	$\Delta t_{\rm fit}$[a] (s)	A (10^8)	$F_{\rm Edd}$ (10^{-8} erg cm^{-2} s^{-1})	$\chi^2_{\rm reduced}(d.o.f)$	$d\xi_b^{1/2}$ (kpc)	Upper limits R_∞ (km)	$M_{\rm max}(M_\odot)$[b]	$R_{M>M_\odot}$ (km)[c]
Pure H	14.3	35	1.144±0.002	5.15±0.20	0.27 (59)	4.3	10.2	1.3	8.2
Pure He	14.3	35	1.186±0.002	4.14±0.09	0.26 (59)	9.7	21.5	2.8	19.8
$0.01Z_\odot$[d]	14.0	35	1.138±0.002	4.71±0.14	0.24 (59)	5.5	13.2	1.7	11.3
$0.01Z_\odot$[d]	14.3	35	1.154±0.002	5.08±0.15	0.23 (59)	5.0	11.6	1.5	9.7
$0.01Z_\odot$[d]	14.6	35	1.167±0.002	5.43±0.19	0.26 (59)	4.6	10.5	1.4	8.4
$0.1Z_\odot$[d]	14.0	35	1.170±0.003	7.35±0.66	0.47 (59)	4.0	9.0	1.2	6.8
$0.1Z_\odot$[d]	14.3	35	1.168±0.004	5.80±0.41	0.45 (59)	4.5	10.2	1.3	8.1
$0.1Z_\odot$[d]	14.6	35	1.174±0.003	5.75±0.31	0.36 (59)	4.4	9.9	1.3	7.8
$Z_\odot$[d,]	14.0	10	1.178±0.020	5.92±1.22	0.36 (31)	5.3	12.4	1.6	10.6
$Z_\odot$[d,]	14.3	10	1.159±0.017	4.81±1.08	0.29 (31)	5.6	13.2	1.7	11.3
$Z_\odot$[d,]	14.6	10	1.164±0.011	4.84±0.52	0.25 (31)	5.4	12.6	1.6	10.7

[a]We fit to data from the time of peak luminosity until $\Delta t_{\rm fit}$ seconds later.

[b]The maximum neutron star mass consistent with the upper limit on $R_\infty = R(1+z)$.

[c]The upper limit on radius assuming a lower limit on mass $M > 1\ M_\odot$.

[d]The composition is solar H/He abundance plus the indicated proportion of solar metallicity.

[e]These fits yielded more than one local χ^2 minima. Here, we report only the minima located at the lowest values of $F_{\rm Edd}$ and A. See text for more details.

$$\gamma \equiv \frac{c^3}{\kappa} \frac{1}{A^4 F_{\rm Edd}} = \frac{R}{(u/2)(1-u)^{3/2}} \tag{2.13}$$

where $u = 2GM/Rc^2$. These definitions differ slightly from those of Steiner et al. (2010) in that they include the anisotropy parameter ξ_b. Then

$$u = \frac{1}{2} \pm \frac{1}{2} \left(1 - 8\alpha\right)^{1/2} \tag{2.14}$$

$$R = \alpha\gamma \left(1 - u\right)^{1/2}. \tag{2.15}$$

To calculate α and γ from A and $F_{\rm Edd}$ obtained from the fits, we require distance d and composition X. A given α and γ then give two solutions for M and R.

We treat the A and $F_{\rm Edd}$ values as given independently of the derived M and R. In fact the derived A and $F_{\rm Edd}$ values depend on the gravity assumed for the spectral models. The color correction f_c decreases with increasing gravity in the models of Suleimanov et al. (2011b) (see their Fig. 5). This implies an increasing A with gravity, which we find in our results for the $Z = 0.01Z_\odot$ models. A similar trend is not seen in the $Z = 0.1Z_\odot$, $Z_\odot$ models. The color correction still decreases with gravity, but the shapes of the models change in such a way as to favor smaller values of $F_{\rm Edd}$, which, given the correlation between the two fitting parameters, leads to values for A that are smaller than expected for the higher gravities. The value of $F_{\rm Edd}$ also increases with gravity for the $Z = 0.01Z_\odot$ models, because the slope of f_c with $F/F_{\rm Edd}$ steepens with increasing gravity, requiring a larger value of $F_{\rm Edd}$ to agree with observed $K^{-1/4}$–F slope.

Overall, we found that the fits are sensitive to the detailed shape of the atmosphere models. This could be due to some small irregularities in the model slopes attributable to the coarseness of the flux grid on which the color corrections are evaluated, and the limited range of fluxes spanned by the bursts we are analyzing.

Table 2.1 shows that for a given metallicity, varying the surface gravity from $\log_{10} g = 14.0$ to 14.6 changes A by up to $\approx 3\%$ for low metallicity, and $F_{\rm Edd}$ by up to $\approx 20\%$. The resulting changes in the limit on R_∞ are $\approx 30\%$ for low metallicity models. This gives a measure of the error introduced by not carrying out a self-consistent fit in which the gravity of the spectral model used and derived M and R are consistent.

Equation (2.12) shows that real-valued solutions for u require $\alpha \leq 1/8$ (Steiner et al. 2010). As emphasized by Suleimanov et al. (2011a, 2011b), this gives an upper limit on the distance for which solutions are possible,

$$\xi_b^{1/2} d \leq \frac{1}{8}\frac{c^3}{\kappa}\frac{1}{F_{\rm Edd}A^2} \tag{2.16}$$

$$= 5.6\ {\rm kpc}\left(\frac{A_8}{1.2}\right)^{-2}\left(\frac{F_{\rm Edd,-8}}{4.0}\right)^{-1}\left(\frac{1+X}{1.7}\right)^{-1}, \tag{2.17}$$

where $A_8 = A/10^8$ and $F_{\rm Edd,-8} = F_{\rm Edd}/(10^{-8}\ {\rm erg\ cm^{-2}\ s^{-1}})$. It also provides a limit on $R_\infty = R(1+z)$. To see this, note that the neutron star radius is[2]

$$R_\infty = R(1+z) = \alpha\gamma \tag{2.18}$$

$$= 12.0\ {\rm km}\left(\frac{\alpha}{1/8}\right)\left(\frac{A_8}{1.2}\right)^{-4}\left(\frac{F_{\rm Edd,-8}}{4.0}\right)^{-1}\left(\frac{1+X}{1.7}\right)^{-1}. \tag{2.19}$$

where the definition of γ from equation (2.13) was used and $(1-u)^{1/2}$ was substituted with $(1+z)^{-1}$. An upper limit on R_∞ is obtained by setting $\alpha = 1/8$ in equation

[2]Note that Zamfir et al. (2012) had a typo in their version of the second line of this equation; the variable α should have been divided by 1/8. It is shown in its correct form here.

(2.19).

The upper limits on $\xi_b^{1/2}d$ and R_∞ are given in Table 2.1. To calculate them we use equations (2.16) and (2.19) with 95% lower limits on the quantities $A^2F_{\rm Edd}$ and $A^4F_{\rm Edd}$ derived from our fits. A slightly different procedure is used for the cases where the fits yielded multiple χ^2 minima. To derive the most conservative upper limits on $\xi_b^{1/2}d$ and R_∞, we consider only the χ^2 local minimum located at the lowest value of $F_{\rm Edd}$ and A, manifested as a distinct, Gaussian-like peak in the respective distributions for the quantities $A^2F_{\rm Edd}$ and $A^4F_{\rm Edd}$. Considering only the part of the Gaussian-like distribution lying below the peak value, we find the 90% lower limits for $A^2F_{\rm Edd}$ and $A^4F_{\rm Edd}$. This is equivalent to taking the 95% lower limit of the whole peak, but has the advantage of allowing us to isolate the χ^2 minimum of interest from the rest of the distribution. As a check, we applied this procedure to model fits showing a single χ^2 minimum, and found very small differences ($< 1\%$) in the derived upper limits when compared to those found by considering the entire distributions.

An upper limit on R_∞ implies an upper limit on the neutron star mass $M_{\rm max} = c^2R_\infty/3^{3/2}G$ (at that mass the radius is $R_\infty/\sqrt{3}$), also given in Table 2.1. Note that the upper limits on R_∞ and d are correlated. Since $\xi_b^{1/2}d_{\rm lim} = \gamma A^2/8$ (compare eqs. [2.13] and [2.16]), we can rewrite equation (2.19) as

$$R_\infty < 12.0\ {\rm km}\ \left(\frac{\xi_b^{1/2}d_{\rm lim}}{5.6\ {\rm kpc}}\right)\left(\frac{A_8}{1.2}\right)^{-2}, \tag{2.20}$$

a larger distance limit allows larger radii.

For solar abundance of hydrogen at the photosphere, we find $\xi^{1/2}d \lesssim 4.0$–5.6 km and $R_\infty < 9.0$–13.2 km. This represents quite stringent limits on the neutron star mass and radius. For this range of R_∞, the maximum neutron star mass is in the range 1.2 to 1.7 $M_\odot$. If we consider a lower mass limit of 1 $M_\odot$, the neutron star radius must be smaller than $R(1\ M_\odot) = 6.8$–11.3 km (the individual values for each model are given in Table 2.1).

2.5.3 Variation of K with accretion rate

Figure 2.2 shows that the bursts with recurrence times of 4.07 hr have significantly smaller values of K than the 5.74 hr bursts, by $\approx 20\%$ (see Galloway & Lampe 2011 for a detailed discussion of the variation of K in the sample of bursts from GS 1826-24). Variations in K between bursts has been seen in other sources. For example, Damen et al. (1989) found that the blackbody temperature (evaluated at a fixed flux level) depended on burst duration. They suggested that variations in chemical composition at the photosphere and the resulting changes in color correction might explain the changing blackbody temperature (and therefore normalization).

We investigate two possible composition variations: changing metallicity with solar H/He abundance, and changing the hydrogen fraction. First, we consider solar H/He abundance and changing metallicity. Suleimanov et al. (2011b) show that f_c drops with increasing metallicity. Therefore we fit the solar metallicity model to the 5.74 hr bursts to determine values of A and $F_{\rm Edd}$ (as given in Table 2.1). These values are then used to compare a low metallicity model to the 4.07 hr data. This comparison is shown in the top panel of Figure 2.4. The low metallicity model lies below the 4.07 hr data, showing that the difference in K cannot be explained by a decrease in metallicity from solar to a fraction of solar.

Second, we consider a change in hydrogen fraction at the photosphere. The lower panel of Figure 2.4 shows the pure He atmosphere fit for the 5.74 hour bursts (see Table 2.1), and a low metallicity solar H/He abundance model for the 4.07 hr bursts

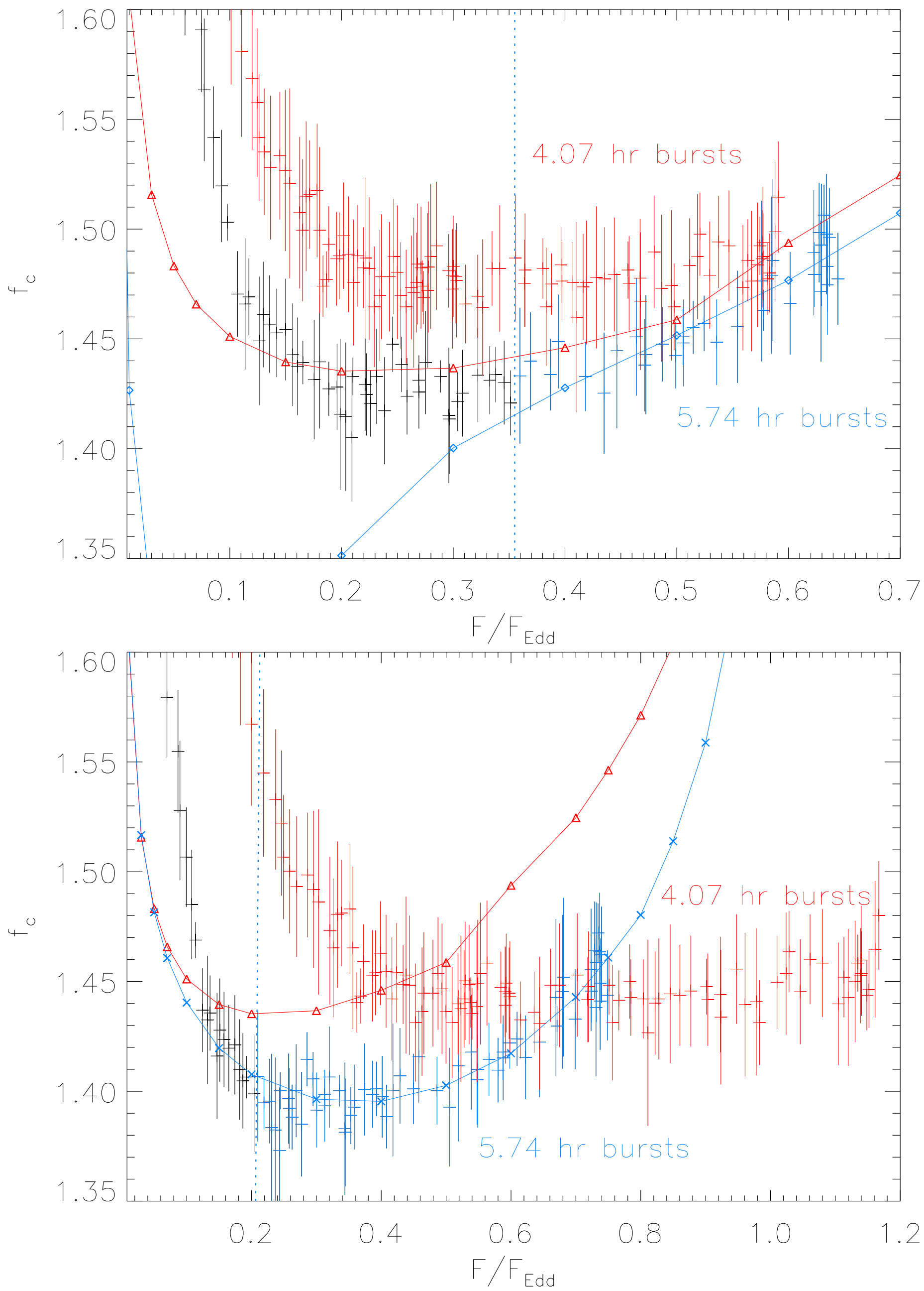

Figure 2.4 Top panel: The solar metallicity fit ($\log_{10} g = 14.3$, linked blue diamonds) that reproduces the first part of the cooling track for the $t_{\rm recur} = 5.74$ hr bursts (blue crosses, and delimited from the data exluded from the fit by a dotted vertical blue line) is plotted together with the data for the $t_{\rm recur} = 4.07$ hr bursts (red crosses) and the low metallicity $Z = 0.01 Z_\odot$ model (linked red triangles) at the same A and $F_{\rm Edd}$ as the solar metallicity model. Bottom panel: A pure He spectral model (linked blue $\times$ symbols) fit to the 5.74 hr bursts (blue crosses) and a low metallicity solar H/He composition model (linked red triangles) at the same A and $F_{\rm Edd}$ adjusted for the different hydrogen fraction. In both panels, the respective symbols show the points where the atmospheric models were calculated.

in which we use the same value of A determined by the pure He atmosphere fit, but decrease the derived $F_{\rm Edd}$ by a factor of $1+X=1.7$ to account for the difference in Eddington flux with composition. This plot shows that the change in f_c in going from pure He to solar H composition is enough to account for the variation in K observed. However, the solar composition model does not match the 4.07 hr data in terms of location on the $F/F_{\rm Edd}$ axis. Another way to say it is that if we fit the 4.07 hr data with a solar composition model, the required $F_{\rm Edd}$ would be larger than for the 5.74 hr data, instead of being a factor $1+X$ times smaller, as is required for simultaneous fits. Furthermore, we see in the lower panel of Figure 2.4 that reducing the derived $F_{\rm Edd}$ by a factor of $1+X=1.7$ for the 4.07 hr bursts implies that the peak flux for those bursts exceeds the Eddington limit, which is known not be the case. Therefore a consistent explanation of the variation in K in terms of changing H fraction at the photosphere is not possible.

2.6 Summary and Discussion

We have compared lightcurve and spectral models with observations of Type I X-ray bursts from GS 1826-24. Here we summarize the main conclusions and discuss our results further.

A general point is that anisotropy in the burst emission enters as an additional uncertainty in any derived quantity that depends on distance. Since it changes the relation between the source luminosity and observed flux, the anisotropy parameter ξ_b (defined in §2.3) always enters in combination with distance as $\xi_b^{1/2}d$. Even in cases where distance to a source can be accurately determined, the anisotropy introduces an effective uncertainty of up to a factor of 20-30%. Anisotropy could be a smaller effect for PRE bursts if the inner disk is disrupted during the burst and intercepts a

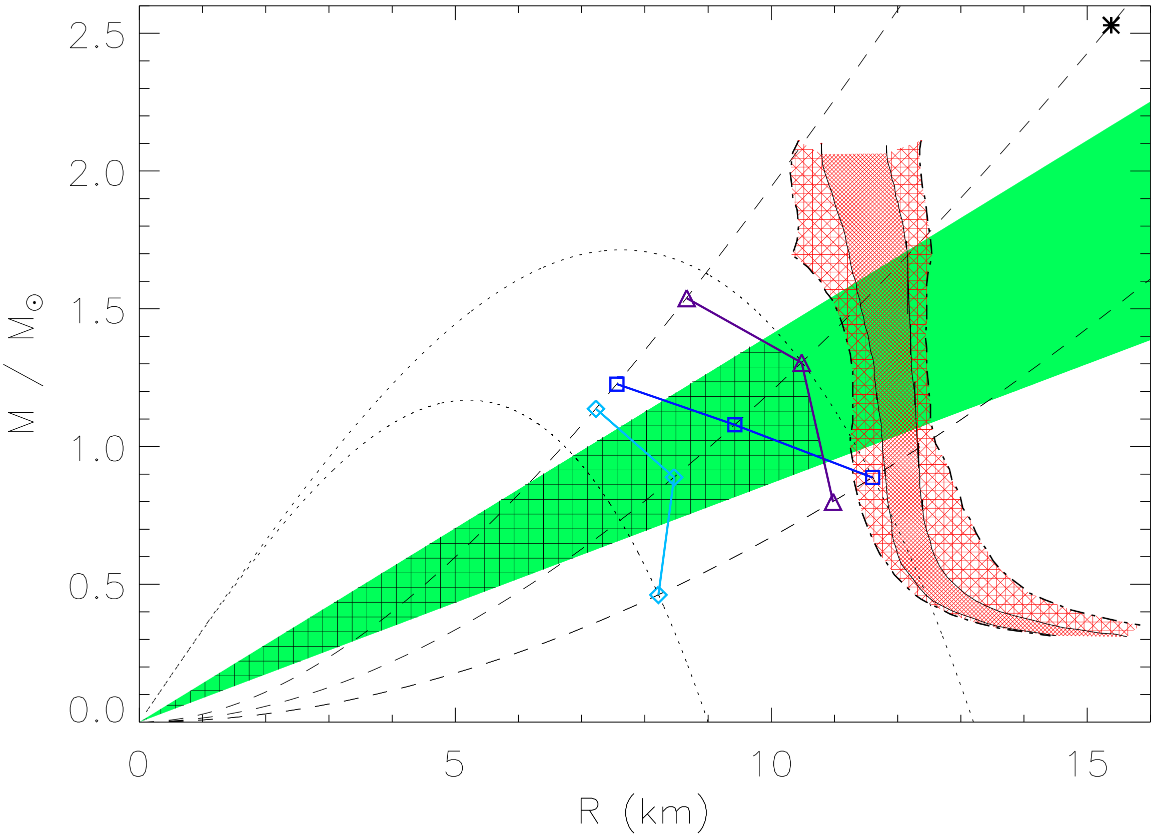

Figure 2.5 Summary of distance-independent constraints in the neutron star mass-radius plane. The dashed curves are lines of constant surface gravity $\log_{10}(g) = 14.0, 14.3, 14.6$ (bottom to top), values at which the spectral models were evaluated. In green, we show the redshift from eq. (2.5) for $f_c = 1.4$–1.5 and an assumed 10% uncertainty in $F_{\rm obs}/F_{\rm model}$. The squares (dark blue), diamonds (light blue) and triangles (purple) represent the upper limits on R_∞ computed from fits to the solar H/He abundance models with $0.01Z_\odot$, $0.1Z_\odot$ and $Z_\odot$ metallicities, respectively, each at a specific surface gravity. The upper limit on R_∞ for the pure Helium atmosphere model (log $= 14.3$) is also shown as a black asterisk. Two constant R_∞ curves are plotted as dotted lines for the highest and lowest values found within solar H/He abundance models. The region hashed in black represents what is allowed by the combination of the constraints derived from the fit to the burst lightcurve and spectral fits to solar H/He abundance models. These constraints are independent of the source distance and anisotropy parameters ξ_b, ξ_p. The region in red represents the mass-radius relation derived by Steiner et al. (2010) (based on the $r_{\rm ph} \gg R$ assumption), with the 1σ and 2σ regions delimited by solid and dot-dashed lines, respectively.

smaller amount of radiation than a disk extending all the way to the stellar surface. Nonetheless, it remains a source of systematic error on derived neutron star radii that needs to be investigated further. For GS 1826-24, the limit $i < 70°$ from Homer et al. (1998) gives $\xi_b^{-1/2} = 0.9$–1.2. Given this uncertainty and the fact that the distance to GS 1826-24 is not well constrained, we focused on deriving limits on M and R that are independent of distance and anisotropy.

The first of these constraints comes from using the model lightcurve from Heger et al. (2007) to fix the overall luminosity scale of the observed bursts. We showed that this leads to a distance and anisotropy independent relation between the redshift $1 + z$ and color correction factor f_c (eq. [2.5]) that depends weakly on the measured normalization K and the ratio of observed and model peak fluxes. For a color correction between 1.4 and 1.5, which spans the range of values in Fig. 2 of Suleimanov et al. (2011) for example, the inferred redshift is between $z = 0.19$ and 0.28.

The second constraint comes from comparing the spectral evolution during the cooling tail with the spectral models of Suleimanov et al. (2011b), which determines the Eddington flux $F_{\rm Edd}$ and the quantity $A = K^{-1/4}/f_c$. As noted by Suleimanov et al. (2011b), for a given set of measured $F_{\rm Edd}$, A parameters, there is an upper limit to the distance of the source beyond which there is no solution for M and R. We point out here that measuring A and $F_{\rm Edd}$ also places an upper limit on $R_\infty = R(1 + z)$ (and therefore upper limits on M and R for a given source). This limit is independent of distance and anisotropy and depends only on the measured values of A and $F_{\rm Edd}$ and the surface hydrogen fraction. For GS 1826-24, atmospheric models with solar hydrogen fractions give $R_\infty < 9.0$–13.2 km (Table 2.1) which implies a neutron star mass $M < 1.2$–$1.7\ M_\odot$ and $R < 6.8$–11.3 km assuming a lower mass limit of 1 $M_\odot$. The corresponding distance limits are $d < 4.0$–5.6 kpc $\xi_b^{-1/2}$.

Uncertainties associated with absolute flux calibration do not affect our results; they are equivalent to an incorrect measurement of the distance to the source, which our constraints are independent of.

The constraints on M and R are summarized in Figure 2.5. We show the upper limits on R_∞ from Table 2.1 for all the solar hydrogen composition models each plotted at the respective surface gravity and the pure Helium model with $\log g = 14.3$, and the redshift range $1+z = 1.16$–1.31 from equation (2.5) with $f_c = 1.4$–1.5 and a 10% uncertainty in the ratio $F_{\rm obs}/F_{\rm model}$. The limits on radii for the solar hydrogen composition are comparable to but a little lower than current theoretical expectations based on dense matter calculations which have radii of 10–13 km for neutron star equations of state that reach a maximum mass $> 2M_\odot$ (Hebeler et al. 2010; Gandolfi, Carlson, & Reddy 2011). The mass-radius relation found in Steiner et al. (2010), derived from a set of photospheric radius expansion X-ray bursts and hydrogen atmosphere fits for transiently accreting neutron stars in quiescence, also lies at slightly larger radii than our R_∞ limits for solar composition. It should be noted that Suleimanov et al. (2011a) call into question the results of Steiner et al. (2010) by suggesting that "short" PRE bursts should be excluded from analysis as they show smaller blackbody normalizations in the burst tail and also do not follow the theoretically expected spectral evolution. The implication is that the mass-radius relation derived in Steiner et al. (2010) would shift to higher radii as a result of using the more reliable "long" PRE bursts, and thus farther away from our derived upper limits.

A smaller hydrogen fraction at the photosphere in GS 1826-24 would increase the R_∞ limits and make them consistent with the theoretical calculations and the mass-radius curve from Steiner et al. (2010). We can get an impression of what the upper limit on R_∞ would be for an atmosphere with a reduced hydrogen fraction by first looking at the extreme case of the pure helium atmosphere, and its derived upper limit of 21.5 km for $\log_{10}(g) = 14.3$ (see Figure 2.5). Such an upper limit is consistent with theoretical calculations and the results from Steiner et al. (2010). We can go one step farther and estimate the hydrogen fraction we would require to have such a consistency with previous results using Equation 2.19. Assuming a surface gravity of $\log_{10}(g) = 14.3$, an upper limit on R_∞ of $\sim$16 km or more would be required. Using values for $F_{\rm Edd}$ and A averaged across the solar H/He model fits with $\log_{10}(g) = 14.3$, we estimate that a hydrogen fraction of $X \approx 0.5$ or less would be needed. We are assuming that such a spectral model would not differ too greatly in shape from the solar H/He models. Galloway et al. (2004) find that the theoretical variations in burst properties with persistent flux between ignition models with X=0.7 and X=0.5 are largely indistinguishable. However, more burst lightcurve simulations would be necessary to establish whether agreement with observed lightcurves is still possible with a reduced accreted hydrogen fraction.

Given that the upper limit on R_∞ depends on the color correction as f_c^4 (via A in equation 2.19), even a small 5% increase in the value of f_c would yield a $\sim$ 22% increase in the upper limit on R_∞. Furthermore, Suleimanov et al. (2011b) discuss large color correction factors of $f_c = 1.6$–1.8 (cf. also Suleimanov & Poutanen 2006) possibly arising from a spreading layer associated with accretion onto the neutron star equator. Perhaps in GS 1826-24 something similar is happening, although the increase in color correction required is not as large. It is worth noting that changing the visible area, for example by blocking one hemisphere of the neutron star with the accretion disk during the burst, does not change the inferred limits on radius because the limit on R_∞ is independent of the anisotropy factor ξ_b (isotropic emission from only half the area is equivalent to setting $\xi_b = 2$).

There are several points to keep in mind when looking at our derived constraints on M and R. First, the constraints are only partly self-consistent in the sense that the lightcurve model used to fit the data does not have the same gravity as the derived M and R. Heger et al. (2007) (and Woosley et al. 2004) used a specific choice of gravity in their X-ray burst simulations. As we argue in §2.4, the lightcurve probably does not depend too sensitively on gravity, but additional simulations are needed to check this, and to calculate the uncertainty in the predicted model flux which enters in equation (2.5) relating f_c and $1+z$. On the other hand, for the comparison to spectral models, in Figure 2.5, the upper limits on R_∞, represented by the solid colored curves, are placed in such a way as to coincide with the appropriate curve of constant surface gravity, consistent with the atmosphere spectral models used to derive those upper limits.

A second issue is that the upper limit on R_∞ from the spectral models is based on fitting the initial part of the cooling tail only. We found that at first the slope of $K^{-1/4}$ with flux agrees well with the theoretical models of f_c. In the latter part of the burst, however, at lower fluxes, the agreement breaks down. For $F/F_{\rm Edd} \lesssim 0.2-0.3$, $K^{-1/4}$ increases with decreasing flux, but more rapidly than expected based on the predicted f_c values, particularly those given by the solar metallicity models. Some other explanation is required for the rapid increase in f_c and corresponding decrease in blackbody normalization in the tail of the burst. In 't Zand et al. (2009) suggest that this decrease could be due to incorrect subtraction of the persistent emission, in particular, the subtraction of a thermal component that comes from the neutron star surface during accretion which is no longer present during the burst. Van Paradijs & Lewin (1986) pointed out that this effect should become important during the tail of the burst, when the burst flux becomes comparable to that of the accretion. Looking at Figure 2.3, the observations and the low metallicity (solar metallicity) models begin to deviate at fluxes below $\sim 5 \times 10^{-9}$ erg cm^{-2} s^{-1}($\gtrsim 10^{-8}$ erg cm^{-2} s^{-1}) compared to the persistent flux of 2.1×10^{-9} erg cm^{-2} s^{-1}.

The disagreement between the observations and models begins sooner following the burst peak for solar metallicity than for low metallicity models because the former have a depression in f_c at low fluxes $F/F_{\rm Edd} \lesssim 0.3$ (see Figure 2.3), arising from absorption edges in partially-ionized Fe (Suleimanov et al. 2011b). There is no sign of such a dip in the observations of GS 1826-24. This suggests a low metallicity in the photosphere, contrasting with the conclusions of Galloway et al. (2004) and Heger et al. (2007) who argued that the metallicity was solar, based on burst lightcurves and energetics. A way to reconcile these disparate results is to consider the possibility that Fe, whose presence has a significant influence on the spectrum but not on the burst energetics, may be absent from the atmosphere during bursts. If accretion halts during the burst, then Fe will rapidly sink through the atmosphere (Bildsten, Chang, Paerels 2003). On the other hand, since bursts from GS 1826-24 are all sub-Eddington, accretion may continue during the burst, resupplying Fe to the photosphere. Furthermore, while disk accretion only deposits mass near the equator, the accreted mass spreads faster latitudinally ($\lesssim 0.1$ s; Inogamov & Sunyaev 1999; Piro & Bildsten 2007) than the timescale for Fe to sink through the atmosphere of ~ 1 s. Proton spallation could also destroy a substantial amount of the accreted Fe (Bildsten, Chang, Paerels 2003). It should be noted that X-ray bursts produce a wide range of elements in their ashes which could significantly alter the spectrum. However, mixing of burned material to the photosphere is thought not to occur due to the substantial entropy barrier (Joss 1977; Weinberg, Bildsten, & Schatz 2006).

Another important unresolved issue is the changing spectral normalization K with accretion rate. The blackbody normalization K is $\approx 20\%$ smaller for the 4.07 hr recurrence time bursts than the 5.74 hr recurrence time bursts. We cannot explain this difference by changing the composition at the photosphere and therefore changing f_c (see discussion in §2.5.3). Also, it seems unlikely that a major change in composition would occur with only a $\approx 50\%$ change in accretion rate and smaller change in burst energy and lightcurves. As mentioned previously in §2.6, Suleimanov et al. (2011b) discuss large color correction factors associated with accretion onto the neutron star equator, which they suggest accounts for the variations in measured K for the different spectral states of 4U 1724-307. Whether the 50% increase of accretion rate seen in GS 1826-24 could result in the amount of hardening of the spectrum observed needs to be investigated. If disk accretion onto the star significantly hardens the burst spectrum, it considerably complicates inference of the mass and radius from burst observations, and means that the range of f_c included when calculating errors on mass radius determinations should allow for a larger range of values than given by spectral models.

We have found that, even though they do not reach Eddington luminosity, the bursts from GS 1826-24 show enough dynamic range in flux as they cool to significantly constrain $F_{\rm Edd}$ by comparing with spectral models. A promising source to look at further is KS 1731-254 which shows both mixed H/He bursts with similar spectral evolution to GS 1826-24 (Galloway & Lampe 2011) and photospheric radius expansion bursts. Analysis of these different bursts, which occur at different persistent fluxes and involve different fuel compositions (based on their energetics, peak luminosities and durations), would give a stringent test of the spectral models and help to constrain any additional spectral components.

3

The Role of Composition in Mixed H/He Burning in GS $1826-24$

3.1 Introduction

Type I X-ray bursts in accreting X-ray binaries can provide valuable clues about neutron star physical parameters. Recently, multizone time-dependent calculations of lightcurves have been used to constrain the distance, accretion composition (Heger et al., 2007a), and the neutron star mass and radius (Chapter 2), in the X-ray binary GS $1826-24$. Such comparisons to multizone time-dependent calculations, if well understood, have the potential to reveal a wealth of information about known X-ray burst sources. As mentioned in Chapter 1, X-ray bursts also offer valuable constraints on neutron star parameters from their emission spectra.

GS $1826-24$ is an ideal source for comparison to burst models for a number of reasons. It has exhibited a range of accretion rates, with the persistent flux varying by a factor of two over all observations. This allows us to see clear evolutions in the burst lightcurve morphology which can be compared to models. Furthermore, at a given accretion rate, the burst lightcurve shapes show a narrow range of scatter, from burst to burst. The distributions of recurrence times also show very little scatter.

For example, bursts seen in 1997 and 1998 respectively had a spread of within five minutes FWHM each (Cocchi et al., 2000), implying a very steady bursting behaviour. GS $1826-24$ burst energetics, recurrence times and lightcurve shapes are all as expected for bursts igniting in the mixed H/He regime (Bildsten, 2000; Heger et al., 2007a).

In this chapter, we focus on the two comparisons made in Chapter 2 between GS $1826-24$ observations and, firstly, theoretical models of burst lightcurves, and secondly, burst spectra. The theoretical models of burst spectra, which were used to compare colour correction factors (f_c) in the cooling tail of bursts, have since been recomputed. The new calculation uses a fully relativistic treatment of Compton scattering in the atmosphere, but more importantly for our analysis, they also calculate the Eddington flux using an accurate expression for the electron scattering opacity (Suleimanov et al., 2012). This has shifted values of f_c upwards by about 1%, across all models, and has increased value of the Eddington flux by $\simeq 10\%$. This warrants an updated analysis of GS $1826-24$ bursts following the technique described in Chapter 2, with the new spectral models. We also re-evaluate the comparison of the observed burst lightcurves to KEPLER simulations, extending the comparison to different recurrence rates. What was initially shown to be a very good agreement at a recurrence time of ~ 4 hours between the observed bursts from GS $1826-24$ and a model having roughly solar metallicity (Heger et al., 2007a), will be shown to break down at longer recurrence rates.

The study of GS $1826-24$ lightcurves, with their long tails, are a new way to test rp-process physics as well as neutron star properties (e.g. in't Zand et al. 2009). The excellent agreement found by Heger et al. (2007a) in the comparison of simulated and observed lightcurves is an exciting development in that respect, but requires additional work to establish a robust understanding of these bursts. Here, we take some initial steps in this direction, finding that there is a need for additional burst simulations to accurately describe the lightcurves of GS 1826 − 24 and their evolution with accretion rate.

In the following section (§3.2), we examine the lightcurve comparison used by Heger et al. (2007a) as well as in Chapter 2, and extend it to other recurrence times. In §3.3, we use the updated spectral models from Suleimanov et al. (2012) to derive new mass and radius constraints on GS 1826 − 24. Lastly, in §3.4 we summarize and discuss.

3.2 Comparison between observed and model lightcurves

Lightcurves generated by KEPLER, a stellar evolution code (Woosley et al., 2004), were compared to those of GS 1826 − 24 in Heger et al. (2007a). They used observations performed in the year 2000, during which GS 1826 − 24 showed bursts with a recurrence time of around 4 hours. Choosing a model which they referred to as "A3", with a roughly solar composition and an accretion rate yielding bursts with a recurrence time matching that of the 2000 observations, they found excellent agreement with the observed lightcurve shape. Their figure 2 (reproduced here as Figure 3.1) shows that the $Z = 0.02$ model reproduces the GS 1826 − 24 lightcurve very well, including the characteristic long tail produced by rp-process burning. A second lightcurve is also shown, from another model ("B3") with roughly the same solar-like H & He mass fractions and recurrence time, but a lower metallicity mass fraction, $Z = 0.001$. This second lightcurve has the wrong shape, having a smaller peak luminosity with a tail that is too luminous and that decays too slowly. Using the model lightcurve to determine the true luminosity of the burst, Heger et al. (2007a) were able to constrain the distance to the source, finding $d = 6.07 \pm 0.18\,\mathrm{kpc}\,\xi_b^{-1/2}$, where ξ_b is the parameter which accounts for anisotropic burst emission (see Chapter 2 §2.3).

In this section, we re-evaluate the comparison described above, and extend it to different recurrence times. To do so, we use a large set of kepler models, computed at different accretion rates and compositions, which are described in §3.2.1. In §3.2.2, we compare lightcurve shapes from kepler simulations to observations of GS 1826-24 at different accretion rates and show that the agreement in shape near $t_{\mathrm{rec}} = 4\,\mathrm{hours}$ breaks down for longer recurrence times. In §3.2.3, we argue that a metal-poor, helium-enriched accreted composition would yield simulated lightcurves which would better describe the variations in peak flux shown by GS $1826-24$. We first establish an empirical relation between peak flux and the average helium mass fraction at ignition (§3.2.3.1), and show that the comparison of this relation to GS $1826-24$ observations implies a low-metallicity accretion (§3.2.3.2).

3.2.1 Description of kepler simulations

In this section, we present the burst properties in the kepler simulations, and show that they are in good agreement with expectations for mixed H/He bursts.

As described in Chapter 1, helium burning operates via rapid triple-alpha reactions, while hydrogen typically burns via the relatively slower CNO cycle, being gated by beta-decay timescales. Hydrogen burning can also break out of the CNO cycle and proceed via the rp-process, but the high temperatures required for this are only reached during a thermal runaway. Above temperatures of $\sim 8\times10^7\,\mathrm{K}$, the CNO cycle burning rate saturates, as proton captures occur much faster than beta-decays. This is called the "hot" CNO cycle, and its rate is limited only by the well-known beta-

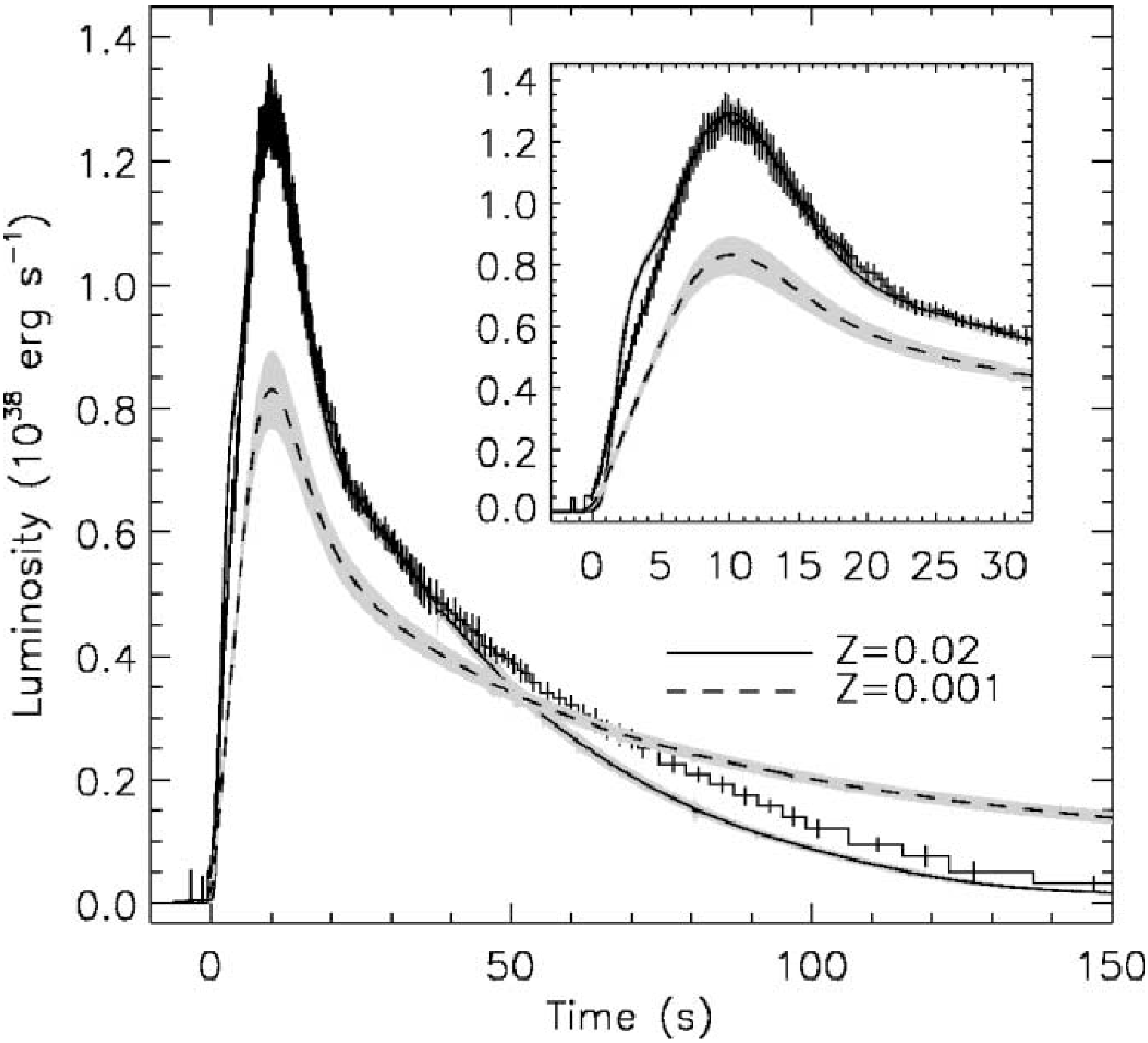

Figure 3.1 A comparison of an average observed lightcurve, represented by the histogram, from bursts observed by RXTE in 2000, with two burst models having different accreted compositions. Model A3 is represented by the black solid curve (with $Z = 0.02$). The inset plot is a magnification of the early portion of the burst. Reproduced from Heger et al. (2007a).

decay rates of O^{14} and O^{15}, which allows us to find a timescale for all the hydrogen in a fluid element to burn away (Cumming 2004 and references therein),

$$t_{\rm CNO} = 11\,{\rm h}\left(\frac{0.02}{Z}\right)\left(\frac{X}{0.7}\right). \tag{3.1}$$

Note that in this expression, the metallicity mass fraction Z is assumed to be composed entirely of CNO elements. Between bursts, as a freshly accreted mixture of hydrogen and helium accumulates onto the neutron star surface, hydrogen is slowly converted to helium on a timescale $t_{\rm CNO}$. The amount of hydrogen and helium present at the onset of a burst will have a strong influence on the lightcurve shape. For example, a large amount of helium will create very short and very bright bursts. The abundance of hydrogen, on the other hand, will affect the shape of the cooling tail of the lightcurve. A large amount of hydrogen, which burns via the rp-process, will cause the lightcurve cooling to be delayed.

For a given accretion rate and composition, long sequences of bursts were produced using the KEPLER code and then used to generate an average lightcurve and recurrence time. The peak luminosity, $L_{\rm peak}$, and burst energy, E_b, were determined from the averaged lightcurves (Lampe et al. 2014, in prep.). The shape of the lightcurves are thus quantified using these two parameters. This greatly simplifies the comparison of modeled to observed lightcurves, which will be carried out in the following sections. Another quantity commonly used to quantify burst shape is τ, the burst timescale (e.g. Galloway et al. 2008), and is calculated by taking $E_b/F_{\rm peak}$. While τ is an intuitive quantity (representing the normalized "width" of the burst lightcurve), being composed of the ratio of E_b to L_{peak}, a good agreement with the latter two parameters implies a good agreement with τ. Therefore, a direct comparison to τ gives no additional information.

A prescription was used to determine the compositional proportions of the accreted matter in the simulations; a mass fraction of metals (Z_0[1]) was first chosen, then the accreted helium mass fraction was calculated according to the following relation $Y_0 = 0.24 + 2Z_0$ (A. Heger, priv. comm.). Such a choice is reasonable based on galactic chemical evolution models (e.g. Timmes et al. 1996), in which the helium fraction and metallicity increase in tandem as subsequent generations of stars enrich the interstellar medium. Finally the hydrogen mass fraction was determined using $X_0 = 1 - Y_0 - Z_0$. For our comparisons, we chose a suite of models which fall in the regime of mixed H/He bursts (e.g. see Bildsten 2000).

Sequences of models are shown in figure 3.2, for five fixed accreted compositions, with varying accretion rates. Models which share the same accreted composition, but with different accretion/burst rates, are linked by solid black lines. The vertical axis in the top panel is peak luminosity $L_{\rm peak}$, and in the bottom panel it is the burst energy E_b, which is defined as the integral of the luminosity over the duration of the burst.

By estimating the burst energy as $E_b = y_{\rm ign}Q_{\rm nuc}$, where $y_{\rm ign}$ is the column depth at the burst ignition and $Q_{\rm nuc}$ is the nuclear energy yield per unit mass, we can roughly understand the vertical offsets of the different E_b curves simply by considering the accreted compositions. Since the ignition depth in mixed H/He bursts is expected to remain close to constant with accretion rate (Bildsten, 1998), variations in $Q_{\rm nuc}$ will determine the behaviour of E_b. Because hydrogen burning has a nuclear yield that is many times larger than helium burning, for the same mass, models which have a higher content of hydrogen will yield more energetic bursts.

[1]We will use the “0” subscript to denote accretion compositions from this point forward. For example, Y_0 represents the accreted helium mass fraction, as opposed to Y which represents the local helium fraction at a particular depth in the accreted layer.

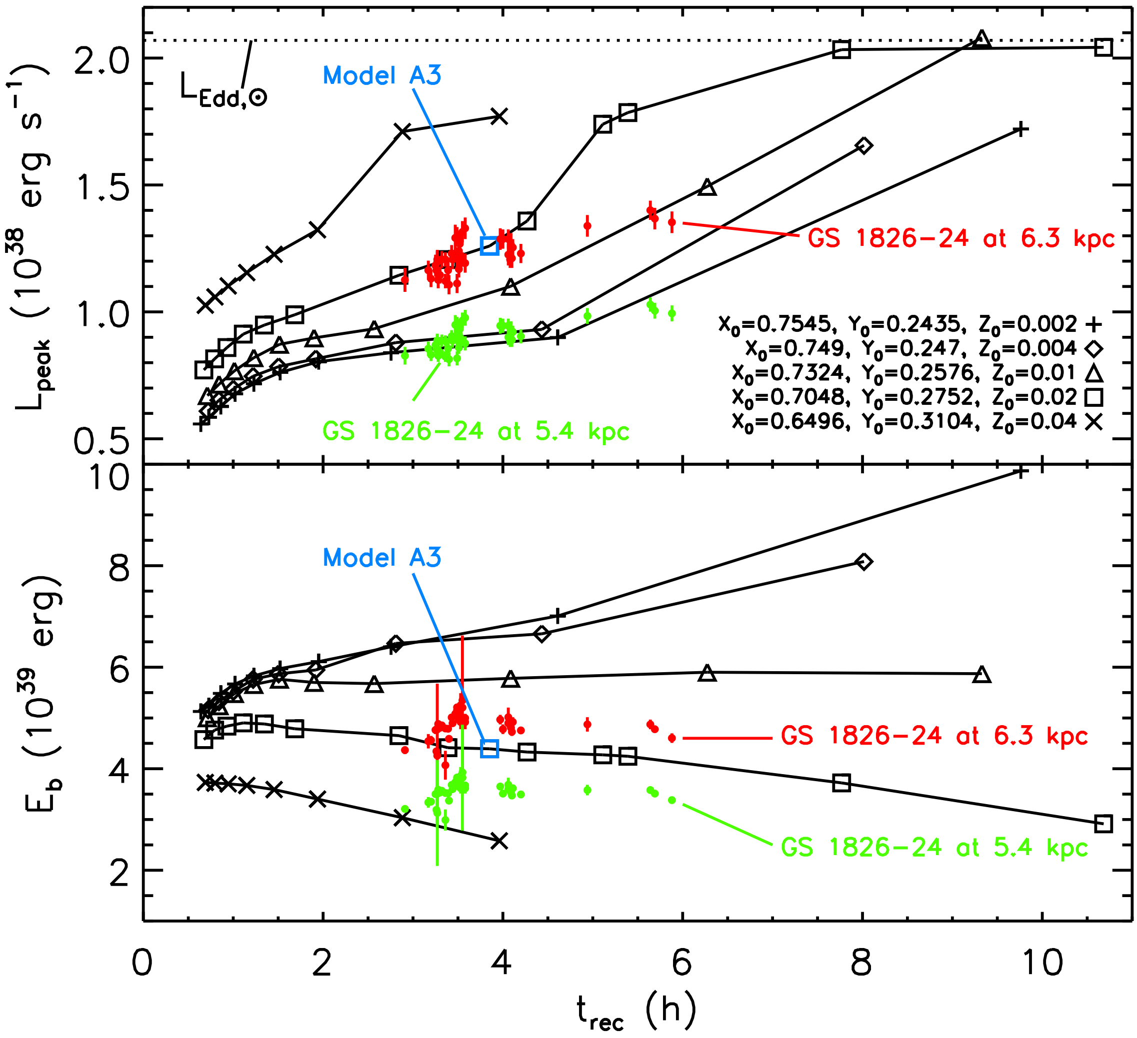

Figure 3.2 A comparison of peak luminosity and burst energy (integrated luminosity) for several KEPLER models and GS 1826-24 data. The solar value ($X_0 = 0.7$) of the Eddington luminosity is shown as a horizontal dotted line. A neutron star radius of $R = 11.2\,\mathrm{km}$ with a redshift of $z = 0.26$ was used find the KEPLER luminosity, observed at infinity. The distance was adjusted to 6.3 kpc, close to the value found in Heger et al. (2007a) of 6.1 kpc. Model A3, whose lightcurve is shown in figure 3.1, is highlighted in blue. We omitted one model since it was a clear outlier to the trend set by neighbouring models with the same composition. This particular model was calculated using a different version of the KEPLER code.

The slopes of the curves for E_b are also related to the amount of hydrogen in the layer, but it is the conversion rate, via CNO cycle burning, of hydrogen to helium which sets the steepness. The models with the highest metallicity have the highest rate of CNO burning, and thus show the steepest decrease in E_b with recurrence time $t_{\rm rec}$. As the accreted metallicity is lowered, the slope of E_b with $t_{\rm rec}$ becomes gentler, reaching nearly zero for $Z_0 = 0.01$. The slope of $dE_b/dt_{\rm rec}$ becomes positive for $Z_0 < 0.01$, which is unexpected. By estimating the column depth at ignition as $y_{\rm ign} = \dot{m}t_{rec}$ in the KEPLER simulations, we determined that the upward trend in E_b is due to an increasing $y_{\rm ign}$. We found that models with $Z_0 \geq 0.01$ show variations $y_{\rm ign} \lesssim 10\%$, roughly consistent with a constant ignition depth. On the other hand, models with $Z_0 < 0.01$ show an increase across the range of recurrence times of roughly 50%. This increase corresponds to approximately an additional $5 \times 10^7\,{\rm g\,cm^{-2}}$, for a typical ignition depth of $10^8\,{\rm g\,cm^{-2}}$. Using the following expression for the nuclear energy yield, $Q_{\rm nuc} = 1.6 + 4.0X$ (Galloway et al., 2004, see also Fujimoto et al. 1987b), we can estimate the expected additional contribution to E_b from a 50% increase in ignition column depth to be $\approx 3 \times 10^{39}$ erg. This agrees well with the increase in E_b for the low metallicity ($Z_0 < 0.01$) models, shown in the lower panel of figure 3.2.

The peak luminosity increases monotonically with recurrence time for all compositions. Looking at models with the same composition in the top panel, it appears that as the layer becomes more helium rich, the peak flux becomes larger. For models having an accreted metallicity $Z_0 \geq 0.01$, this implies bursts which are brighter and shorter, from the downward trends in E_b. This is the expected behaviour for bursts as they become helium enriched (e.g. see Galloway et al. 2008).

An interesting feature of the peak luminosity curve for the $Z_0 = 0.02$ models is the flattening seen at recurrence times $\gtrsim 8$ hrs. The peak luminosity remains nearly unchanged between the two highest recurrence times. This feature is attributable to the fact that the luminosity cannot exceed the Eddington limit, which is shown as a horizontal dotted line. The value of the Eddington luminosity is calculated for a solar-like composition, that is, with $X = 0.7$, and follows the prescription from the appendix of Keek & Heger (2011).

3.2.2 Extending the comparison of lightcurves to different recurrence times

In this section, we examine the lightcurve comparisons between GS $1826-24$ and KEPLER models sharing the same accreted composition as "A3" ($X_0 = 0.7$, $Y_0 = 0.28$, $Z_0 = 0.02$), but at different recurrence times. We show that while there is a good agreement near $t_{\mathrm{rec}} = 4$ hours (as demonstrated by Heger et al. (2007a), and can be seen in Fig. 3.1), the agreement breaks down when we extend this comparison to different recurrence times.

In Figure 3.2, the peak luminosity and burst energy, calculated from observations of GS $1826-24$ (taken from the Galloway et al. 2008 catalog), are shown in a comparison to several KEPLER models. The KEPLER model symbolized with a blue square at a recurrence time of 3.9 h is A3, whose lightcurve is shown in figure 3.1. The agreement in peak luminosity between that model and bursts clustered around the 4 hour recurrence time is very good. The same comparison in the lower panel shows a small disagreement in the burst energy of roughly 0.5×10^{39} erg, which is about 10% of the observed value. Figure 3.1 shows that in the tail of the $Z_0 = 0.02$ lightcurve, the model underestimates the observed luminosity for a duration of over 100 s. If we take the disagreement between the observed and $Z_0 = 0.02$ lightcurves to be on the order of $5 \times 10^{36}\,\mathrm{erg\,s^{-1}}$, over 100 s, this accounts for a difference in burst energy of 0.5×10^{39} erg, which agrees with gap in E_b between red clump of bursts near $t_{\rm rec} = 4$ hrs and the blue square representing model A3.

Comparing the GS 1826-24 data to different models sharing the same composition as A3, we find similarly good agreements at recurrence times below 4 hours. However there is clear divergence in the trends for recurrence times greater than 4 hours, particularly when looking at the peak luminosity. The observed trend has a smaller slope compared to the KEPLER $Z_0 = 0.02$ models. At the highest recurrence times of nearly 6 hours, the gap in $L_{\rm peak}$ widens to almost 40% of the KEPLER value. Since the KEPLER models with $Z_0 = 0.02$ do not accurately reproduce the observed trend, this challenges the notion of a solar composition accretion in GS $1826 - 24$.

The slope of $dL_{\rm peak}/dt_{\rm rec}$ in GS 1826-24 being fairly small, it more closely resembles that of the lowest metallicity model, $Z_0 = 0.002$. If we adjust the presumed distance to GS $1826 - 24$ from $d = 6.3$ kpc down to $d = 5.4$ kpc, we can align the $L_{\rm peak}$ data points with the $Z_0 = 0.002$ models and find a reasonable agreement (shown as the green points, compared to the black crosses, in the top panel of Fig. 3.2). However, lowering the distance to $d = 5.4$ kpc also implies moving the E_b data points downwards as shown in the lower panel of Figure 3.2, again by the green points. The problem is that the models representing $Z_0 = 0.002$ on the E_b panel of Fig. 3.2 are much higher than the data, making a consistent fit not possible. To summarize, low metallicity models have less hydrogen burning during accumulation, therefore have fairly constant peak fluxes with respect to the recurrence time, which matches the GS $1826 - 24$ trend. However, the burst energies for these low metallicity models are predicted to be larger than the observations by nearly a factor of ~ 2.

3.2.3 A low metallicity, helium-enriched accretion in GS 1826-24?

We are unable to capture the behaviour of GS 1826-24 using the models at our disposal. This may in part be due to the rigid rule used to determine the composition of the models. They all lie on a common $X_0 - Z_0$ trend, where, for example, the helium mass fraction is forced to scale with the metallicity. This trend, which may be appropriate for the galactic chemical evolution averaged over a stellar population, is likely not appropriate for a star undergoing mass transfer in a binary system. The helium-metallicity relation for the donor companion star, if not fully convective, will depend on the location within the star.

In this section, we first develop a simplified theory of how the burst peak flux depends on the accreted composition and recurrence time (§3.2.3.1). We then use this to suggest an alternative composition for the accretion in GS $1826-24$, one that has a low metallicity, and is enriched in helium (§3.2.3.2).

3.2.3.1 The relation between peak luminosity and helium mass fraction

Fujimoto et al. (1981) argued that the extent of the convection zone, which starts at the ignition depth, scales inversely with the nuclear heating timescale. Since the triple-alpha reaction rate is very sensitive to the helium mass fraction ($\epsilon_{3\alpha} \propto Y^3$), a layer which is helium enriched will very efficiently transport heat outwards to the surface, causing the burst peak to be large. This was confirmed in Hanawa & Fujimoto (1986) in time-dependent burst simulations.

Fujimoto et al. (1987b) argued that the relevant quantity for determining the peak flux should be the average helium mass fraction $\overline{Y}$ in the fuel layer, and not the value of Y at the base where ignition occurs. This is justified by the fact that convection appears early in the onset of a thermal runaway, which mixes a large portion of the accreted fuel layer.

Motivated by these arguments, here we attempt to find a relation between the peak flux given by the KEPLER models, and an estimate of the average helium mass fraction of the layer at ignition. To find $\overline{Y}$, we begin by estimating the average hydrogen mass fraction $\overline{X}$ in the layer. From the continuity equation, we have that $dX/dy = -\epsilon_{\rm CNO}/\dot{m}E_{\rm CNO}$, where $\epsilon_{\rm CNO}$ is the hydrogen burning rate via hot CNO cycle burning, and $E_{\rm CNO}$ is the energy release per unit mass. Since the hot CNO cycle burns hydrogen at a constant rate, this expression is easily integrated, giving the hydrogen mass fraction profile

$$X(y) = \begin{cases} X_0\,[1 - y/y_d] & \text{for } y \leq y_d, \\ 0 & \text{for } y \geq y_d, \end{cases} \tag{3.2}$$

where X_0 is the accreted hydrogen mass fraction, and y_d is the depth at which hydrogen becomes depleted via CNO-cycle burning. This depth is given by $y_d = \dot{m}E_{\rm CNO}/\epsilon_{\rm CNO}$, or simply $y_d = \dot{m}t_{\rm CNO}$, where $t_{\rm CNO}$ is given by equation (3.1). We evaluate the average hydrogen mass fraction in the fuel layer with

$$\overline{X} = \frac{1}{y_b}\int_0^{y_b} X(y)dy, \tag{3.3}$$

where the integration extends down to the base of the accreted fuel layer, $y_b = \dot{m}t_{\rm rec}$. Evaluating this expression depends on whether the accreted column y_b is larger or smaller than the depletion depth y_d, or in other words, if the recurrence time is longer or shorter than $t_{\rm CNO}$:

$$\overline{X} = \begin{cases} X_0\,[1 - t_{\rm rec}/2t_{\rm CNO}] & \text{if } t_{\rm rec} \leq t_{\rm CNO}, \\ X_0 t_{\rm CNO}/2t_{\rm rec} & \text{if } t_{\rm rec} \geq t_{\rm CNO}. \end{cases} \tag{3.4}$$

From this, the average helium mass fraction is obtained from $\overline{Y} = 1 - \overline{X} - Z$, where we assume that Z is a constant throughout the layer.

An important effect that is naturally included in time-dependent simulations is compositional and thermal inertia (Taam, 1981; Woosley et al., 2004). Compositional inertia is manifested by the ignition of a burst inside in the ashes of a previous burst, which are enriched in metals, such as CNO nuclei. This affects the burst properties, for example, by acting to reduce the sensitivity to the accreted metallicity (Woosley et al., 2004). To account for this, we include a metallicity contribution $Z_{\rm inertial}$, the "inertial" metallicity, such that the total metallicity in the accreted layer is $Z = Z_0 + Z_{\rm inertial}$.

Most of the models shown in Fig. 3.2 fall in the regime of $t_{\rm rec} \leq t_{\rm CNO}$, but we include both cases in our calculation of $\overline{Y}$, enabling us to extend our predictions to recurrence times $t_{\rm rec} > t_{\rm CNO}$. The average helium mass fraction for the $t_{\rm rec} < t_{\rm CNO}$ regime is approximately

$$\overline{Y} = Y_0 + \frac{1.6 t_{\rm rec}(Z_0 + Z_{\rm inertial})}{X_0}, \text{ for } t_{\rm rec} < t_{\rm CNO}. \tag{3.5}$$

The average helium mass fraction in the case of $t_{\rm rec} > t_{\rm CNO}$ is

$$\overline{Y} = Y_0 + X_0 \left[1 - \frac{0.16}{t_{\rm rec}(Z_0 + Z_{\rm inertial})}\right], \text{ for } t_{\rm rec} > t_{\rm CNO}. \tag{3.6}$$

For any burst recurrence time and accreted composition, these two expressions for

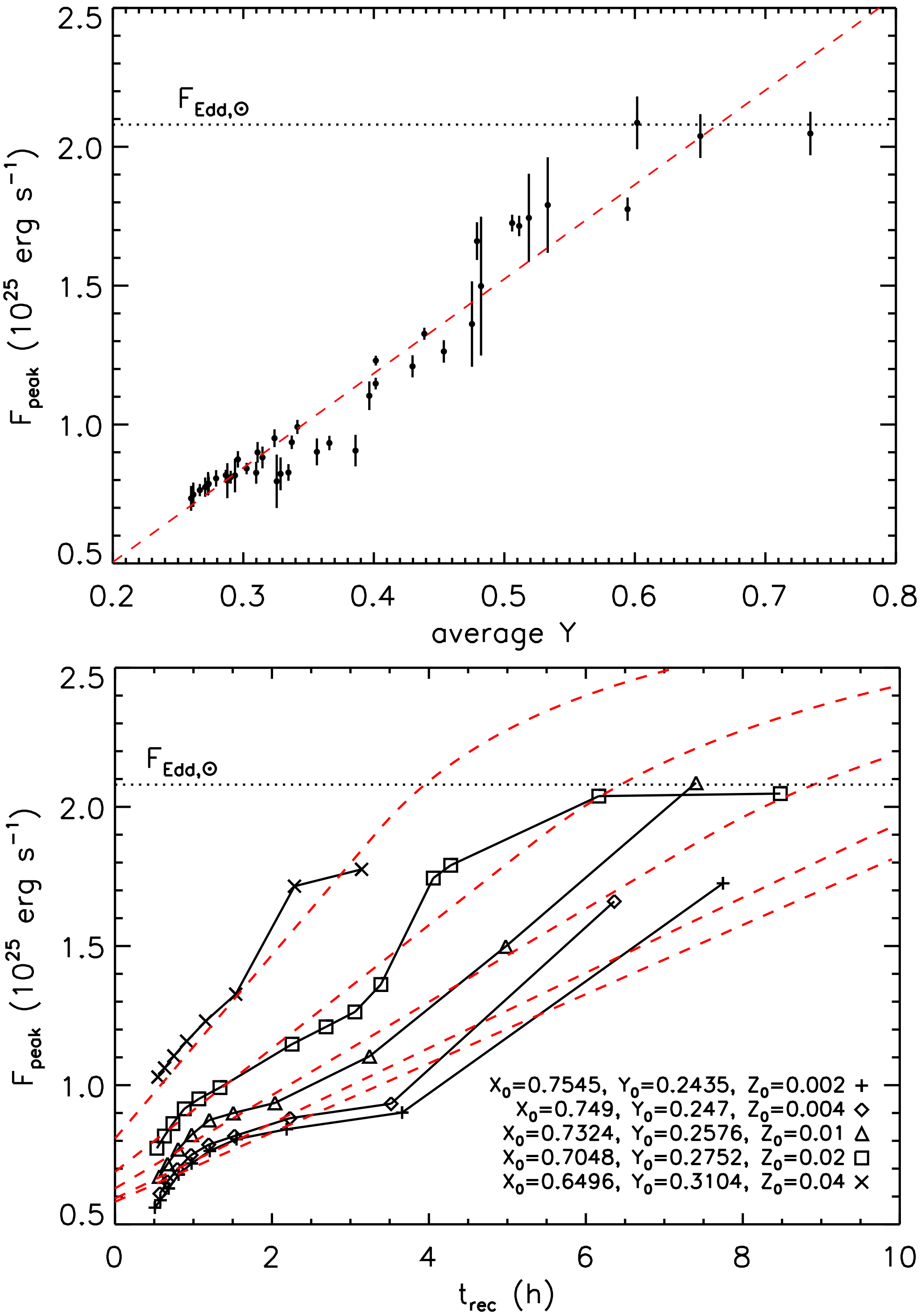

Figure 3.3 In the top panel, a linear fit (red dashed curve) to a suite of KEPLER simulations (shown by black points with vertical error bars) for $F_{\rm peak}$ against $\overline{Y}$. The solar value ($X_0 = 0.7$) of the Eddington flux is also shown as a horizontal dotted line. In the bottom panel, we show separate fits to individual KEPLER simulations for F_{peak} against t_{rec}, using the linear relation shown in the top panel, with compositions adjusted to match the individual KEPLER models. The Eddington flux is displayed again.

$\overline{Y}$ allow us to estimate the helium mass fraction at ignition. Using this, we look for a correlation between $F_{\rm peak}$ and $\overline{Y}$ across the suite of KEPLER models at our disposal. The value of $Z_{\rm inertial}$ is treated as a free parameter, which we vary to minimize the scatter in the $L_{\rm peak} - \overline{Y}$ trend. In the top panel of Figure 3.3, we show a plot of the peak flux against $\overline{Y}$ for all the KEPLER models, where we used $Z_{\rm inertial} = 0.021$. The errors shown are derived from the burst-to-burst scatter in a given KEPLER model, for a fixed accretion rate and composition. We fit a straight line through the KEPLER models, and find an empirical relation between $F_{\rm peak}$ and $\overline{Y}$:

$$F_{\rm peak,\,25} \;=\; 3.4\overline{Y} - 0.18, \tag{3.7}$$

where $F_{\rm peak,\,25} = F_{\rm peak}/(10^{25}\,{\rm erg\,cm^{-2}\,s^{-1}})$. This relation reproduces any given KEPLER data point in the top panel of Figure 3.3 to an accuracy of within $\simeq$20%.

The derived fit suggests that when the average helium mass fraction in the accreted layer is greater than $\overline{Y} \simeq 0.66$, the peak flux will be limited by the Eddington flux. This is similar to the result quoted in Fujimoto et al. (1987b), who find the necessary average abundance to be $\overline{Y} = 0.5$.

We can verify how well the derived $F_{\rm peak} - \overline{Y}$ linear relation reproduces the individual KEPLER models shown in Fig. 3.2. Using equations (3.5) and (3.6), we transform equation (3.7) into a $F_{\rm peak} - {\rm t}_{\rm rec}$ relation which depends on accreted composition. By setting the appropriate compositions, we compare to the individual KEPLER curves, as shown in the second panel of Fig. 3.3. The estimates reproduce the general features of the KEPLER models, with some disagreements. For models with $Z \leq 0.01$, the approximations underestimate the peak flux of the KEPLER simulations with $t_{\rm rec} > 6\,$hrs, showing disagreements of up to 15%. Our estimates did not include the fact that the flux will be subject to the Eddington limit, which is illustrated by the disagreement in the $Z = 0.02$ model, at the highest recurrence time. Overall, our derived relation between $F_{\rm peak}$ and $\overline{Y}$ is able to approximately reproduce the features of the KEPLER simulations.

The comparison shown in the second panel of Fig. 3.3 also implies that, depending on the accreted metallicity, we can determine the recurrence rate at which we expect to see Eddington-limited bursts (PRE). For $Z = 0.04$, this is $\simeq 4$ hours, $\simeq 6$ hours for $Z = 0.02$ and $\simeq 9$ hours for $Z = 0.01$. This agrees well with the expectation that a larger metallicity will diminish the time required for the average helium mass fraction to reach $\overline{Y} \simeq 0.66$.

3.2.3.2 Application to GS $1826-24$ observations

The relation we derived for $F_{\rm peak} - \overline{Y}$ is calibrated against the KEPLER models which lie on a particular $Y_0 - Z_0$ relation. In this section, we assume that the relation holds for other combinations of Z_0 and Y_0 and look for a composition that matches the observed properties of the GS $1826-24$ bursts.

From the linear relationship between $\overline{Y}$ with $F_{\rm peak}$ (equation 3.7), we find that the slope of $dF_{\rm peak}/dt_{\rm rec}$, in the regime of $t_{\rm rec} \leq t_{\rm CNO}$, is

$$\frac{dF_{\rm peak,\,25}}{dt_{\rm rec}} = \frac{5.1(Z_0 + Z_{\rm inertial})}{X_0}, \tag{3.8}$$

which shows that the slope is proportional to the total metallicity $Z_0 + Z_{\rm inertial}$, while the overall normalization of the $F_{\rm peak} - t_{\rm rec}$ trend is proportional to the accreted helium mass fraction Y_0. The slope also has a dependence on X_0, which in theory introduces a degeneracy in the slope between X_0 and Z_0. In practice, since the vertical offset is set by Y_0, this fixes X_0.

For GS $1826-24$, we will be able to constrain the metallicity from the slope of the $F_{\rm peak}$ observations. However, since the distance is unknown, and without simultaneously fitting to E_b, determining the accreted helium mass fraction is not possible.

We attempt to fit the GS $1826-24$ observations by varying the composition in our empirically derived $F_{\rm peak}-{\rm t}_{\rm rec}$ relation and find a good fit using $Z_0 = 0.001$, as shown in Figure 3.4. We illustrate the degeneracy in the fit between the accreted helium mass fraction and distance by finding adequate fits to observations set at three different distances, $d = 6.1$, 6.9, 7.6 kpc, by modifying the accreted helium mass fraction to $Y_0 = 0.3$, 0.4, 0.5, respectively. However, as we previously showed in Figure 3.2, a low-metallicity model with an accreted helium mass fraction of $Y_0 \approx 0.25$ cannot provide a consistent fit to GS $1826-24$ observations. Therefore, the degeneracy between distance and accreted helium mass fraction can, in practice, be broken by the additional comparison of observed and theoretical burst energy, as will be discussed later in this section.

The fact that GS $1826-24$ bursts do not show PRE does not significantly constrain the accreted composition. Figure 3.4 shows the solar value (with $X_0 = 0.7$) of the Eddington luminosity, as well as the value corresponding to a $Y_0 = 0.5$ accretion (using $X_0 = 0.5$, which neglects the small contribution from Z_0), as two horizontal dotted lines. The comparison that uses an accreted helium mass fraction of $Y_0 = 0.5$ implies that the bursts are intrinsically brighter. The brightest of those bursts reaches the Eddington limit for a *solar* composition. However, the appropriate Eddington limit is found by reducing the hydrogen mass fraction to be consistent with $Y_0 = 0.5$. The brightest GS $1826-24$ bursts, at a distance of $d = 7.6$ kpc have peak luminosities

$\simeq 15\%$ below the appropriate ($X_0 = 0.5$) Eddington limit.

Lowering the metallicity below $Z_0 = 0.001$ does not noticeably affect the slope of $dF_{\rm peak}/dt_{\rm rec}$ in our fit to GS 1826 − 24. This is because the slope is determined by the total metallicity, as shown in equation (3.8). Since $Z_{\rm inertial} = 0.021$, it effectively sets a lower bound on the initial part ($t_{\rm rec} < t_{\rm CNO}$) of the $dF_{\rm peak}/dt_{\rm rec}$ slope. This allows us to put a constraint on the upper limit of Z_0. Using the distance values shown in Figure 3.4, we find that for observations at $d = 6.1\,$kpc the upper limit on Z_0 is stringent: $Z_0 \lesssim 0.002$. For $d = 6.9\,$kpc, we require that $Z_0 \lesssim 0.006$, while for $d = 7.6\,$kpc, the estimate fits the data reasonably until $Z_0 \lesssim 0.01$. Note that for the latter two fits ($d = 6.9$ and $d = 7.6\,$kpc), at the upper limit values of Z_0, the respective accreted helium mass fractions had to be lowered by $\sim 10\%$, with respect to the values shown in Figure 3.4. For values of Z_0 greater than the upper limits quoted above, the slope of our estimate becomes too steep to give a good fit to the data.

We can get a sense of how simultaneously analyzing E_b, in conjunction with $F_{\rm peak}$, would enable us to constrain the distance and the accreted helium mass fraction, thus breaking the degeneracy outlined above. Firstly, from Fig. 3.2, it is clear that using a $Z_0 = 0.001$, $Y_0 = 0.25$ model with a distance of 5.4 kpc will not reproduce the GS 1826 − 24 lightcurve shape since E_b will be dramatically overestimated by the models. A lightcurve having a recurrence time of around 4 hours, with $Z_0 = 0.001$ and $Y_0 = 0.25$, is shown in Figure 3.1. In order for this lightcurve to agree with the observed peak luminosity, we must decrease the assumed distance to the source in order for the lightcurve peaks to align. However, it is clear that there would be a significant disagreement between the observed and simulated lightcurves since the latter would overestimate the observed luminosity in the tail by a substantial

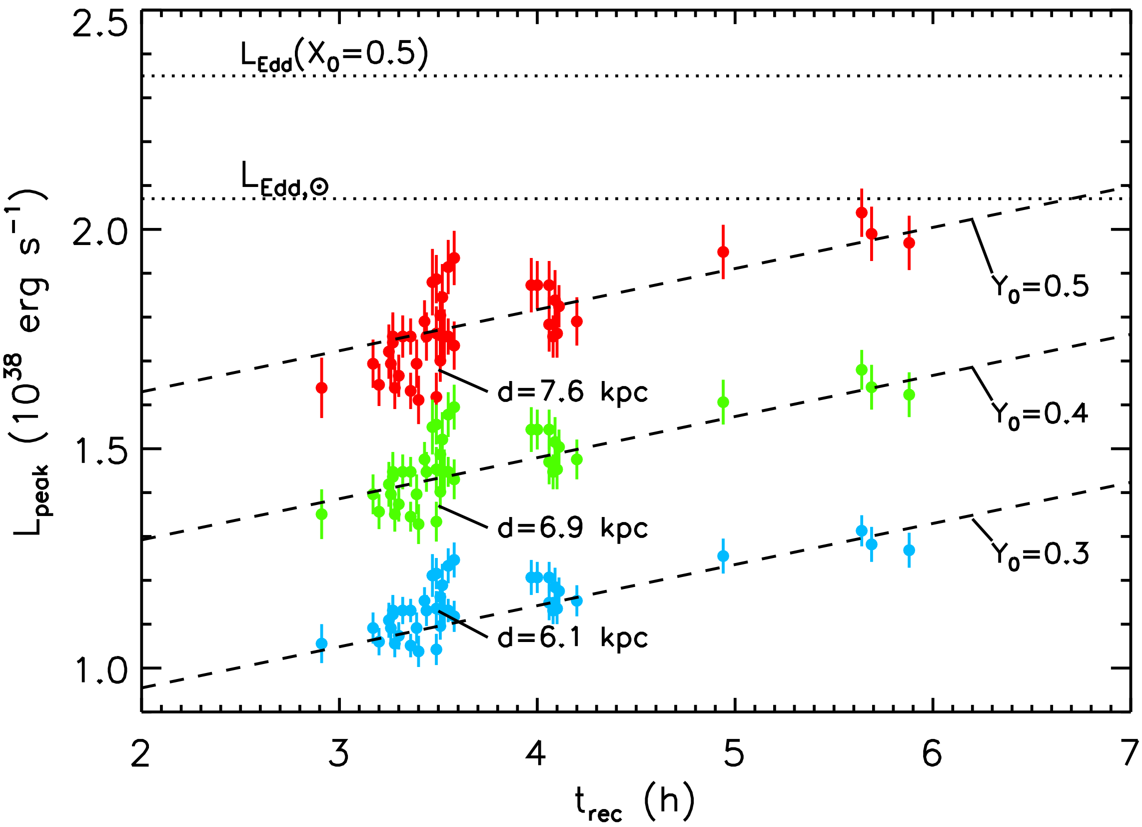

Figure 3.4 Fitting the empirical $F_{\mathrm{peak}} - t_{\mathrm{rec}}$ relations to GS 1826 − 24 observations. The observations were set at three distances ($d = 6.1,\ 6.9\ 7.6\,\mathrm{kpc}$), which required three specific accreted helium mass fractions ($Y_0 = 0.3,\ 0.4,\ 0.5$) in order to fit. To plot the KEPLER values of peak luminosity, we assumed a neutron star radius of 11.2 km and a redshift $z = 0.26$. Two dotted horizontal lines represent the Eddington luminosities computed with a solar composition ($X_0 = 0.7$) in one case, and with $X_0 = 0.5$ in the other, which is roughly consistent with a $Y_0 = 0.5$ accretion (we neglected a small contribution from Z_0).

margin. If we could, while holding this metallicity ($Z_0 = 0.001$) constant, decrease the hydrogen mass fraction of the layer (and thus increase the helium mass fraction), this would lead to less rp-process burning in the tail, and an overall lower burst energy possibly bringing the models into agreement with the observations. From this, we can see that by comparing both the peak flux and the burst energy, we could constrain both the composition and distance.

The comparison described above, however, is only possible once we have determined the accreted metallicity from the *slope* of $dF_{\rm peak}/dt_{\rm rec}$ in the GS $1826-24$ observations. Comparing lightcurves at a single recurrence time is insufficient to fully constrain the accretion composition and the distance. This is understandable, since there are three independent parameters we wish to constrain; distance, and two of the three composition components, since the third is obtainable using $1 = X_0 + Y_0 + Z_0$. At a given recurrence time, there are only two lightcurve parameters that we are constraining, $F_{\rm peak}(Y_0, Z_0, d)$ and $E_b(Y_0, Z_0, d)$. The additional constraint necessary comes from comparisons of the variation, or slope, of $F_{\rm peak}$ with $t_{\rm rec}$. In addition, the problem can be overdetermined if the observed variations in E_b are also compared to the theoretical simulations.

As such, by comparing the lightcurve shape at single recurrence time (~4 hours), and not surveying a larger set of simulations with compositions having independently varying Y_0 & Z_0, Heger et al. (2007a) did not identify the possibility that the problem of constraining composition and distance was underdetermined, which hypothetically would enable many different combinations of composition and distance to match the $t_{\rm rec} = 4\,$hour GS $1826-24$ lightcurve.

3.3 New spectral fits to GS 1826-24 bursts

We closely follow the procedure described in §2.5 of Chapter 2 for fitting theoretical curves of f_c to observations of GS $1826-24$ to obtain constraints on the mass and radius that are independent of distance and emission anisotropy. However, here we use the updated calculations of burst spectra from Suleimanov et al. (2012), which improved upon the models from Suleimanov et al. (2011b) by employing an exact treatment for Compton scattering in the atmosphere, and by calculating the Eddington flux using a more accurate expression for the electron scattering opacity (Suleimanov et al., 2012).

In Table 3.1, we show our results from the fits of spectral models with different compositions and surface gravity values to GS $1826-24$ burst data. The two parameters which are varied to obtain a fit are $A = (R_\infty/d)^{-1/2}\xi_b^{1/4}$, where $R_\infty = R(1+z)$ and ξ_b is the burst anisotropy parameter, and the observed Eddington flux $F_{\rm Edd} = GMc/\kappa d^2\xi_b(1+z)$, where κ is the Thomson opacity $0.2(1+X)\,{\rm cm}^2\,{\rm g}^{-1}$. The best-fit values of A and $F_{\rm Edd}$ are quoted in Table 3.1, with their respective $1-\sigma$ uncertainties, as well as the corresponding reduced χ^2.

In addition to displaying the updated upper limits on $d\xi_b^{1/2}$ and R_∞, Table 3.1 also shows derived upper limits on $M_{\rm max}$, the maximal mass consistent with the respective upper limit on R_∞, and in the last column, $R_{M>M_\odot}$, the upper limit on the neutron star radius, assuming a lower limit mass of one solar mass. We calculate $M_{\rm max}$ by finding the peak values of mass from the respective R_∞ curves. Two curves of constant R_∞ are shown in Fig. 3.5 as dotted black lines, and since they are concave (frowning) functions of the neutron star radius, R, it is simple to determine the maximum mass, $M_{\rm max}$. The upper limit $R_{M>M_\odot}$ is calculated again by considering the respective

Table 3.1. New fits of spectral models to the burst cooling tail in GS 1826 − 24

Composition	$\log_{10} g$	$\Delta t_{\rm fit}$[a] (s)	A (10^8)	$F_{\rm Edd}$ (10^{-8} erg cm^{-2} s^{-1})	$\chi^2_{\rm reduced}(d.o.f)$	Upper limits $d\xi_b^{1/2}$ (kpc)	Upper limits R_∞ (km)	Upper limits $M_{\rm max}(M_\odot)$[b]	Upper limits $R_{M>M_\odot}$ (km)[c]
Pure H	14.3	35	1.130±0.002	4.80±0.15	0.25 (59)	4.7	11.4	1.5	9.4
Pure He	14.3	35	1.171±0.002	3.85±0.09	0.26 (59)	10.7	24.2	3.1	22.6
$0.01Z_\odot$[d]	14.0	35	1.123±0.002	4.34±0.12	0.24 (59)	6.1	15.1	2.0	13.3
$0.01Z_\odot$[d]	14.3	35	1.139±0.002	4.67±0.15	0.25 (59)	5.6	13.3	1.7	11.4
$0.01Z_\odot$[d]	14.6	35	1.153±0.002	5.02±0.18	0.27 (59)	5.1	11.9	1.5	10.0
$0.1Z_\odot$[d]	14.0	35	1.154±0.004	5.77±0.45	0.47 (59)	4.9	11.5	1.5	9.5
$0.1Z_\odot$[d]	14.3	35	1.154±0.004	5.33±0.38	0.43 (59)	5.0	11.7	1.5	9.8
$0.1Z_\odot$[d]	14.6	35	1.161±0.003	5.33±0.29	0.36 (59)	4.8	11.1	1.4	9.1
$Z_\odot$[d,]	14.0	10	1.193±0.022	4.65±0.37	0.35 (31)	6.1	14.8	1.9	13.0
$Z_\odot$[d,]	14.3	10	1.154±0.030	4.53±0.31	0.31 (31)	6.1	14.6	1.9	12.8
$Z_\odot$[d]	14.6	10	1.155±0.012	4.57±0.52	0.26 (31)	6.0	14.2	1.8	12.4

[a] We fit to data from the time of peak luminosity until $\Delta t_{\rm fit}$ seconds later.

[b] The maximum neutron star mass consistent with the upper limit on $R_\infty = R(1+z)$.

[c] The upper limit on radius assuming a lower limit on mass $M > 1\ M_\odot$.

[d] The composition is solar H/He abundance plus the indicated proportion of solar metallicity.

[e] These fits yielded more than one local χ^2 minima. Here, we report only the minima located at the lowest values of $F_{\rm Edd}$ and A. See text for more details.

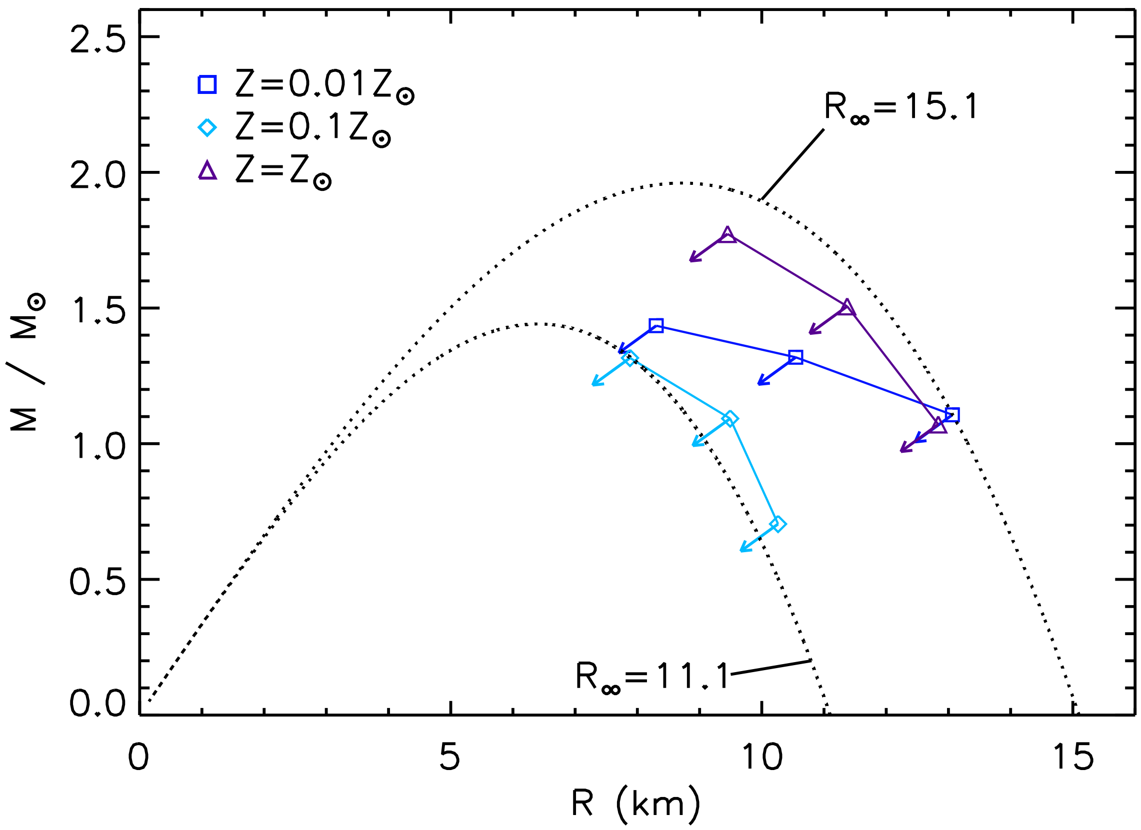

Figure 3.5 Updated mass and radius constraints for GS 1826−24 using the latest spectral models from Suleimanov et al. (2012). This is effectively an update of Figure 2.5. The squares (dark blue), diamonds (light blue) and triangles (purple) represent the upper limits on R_∞ computed from fits to the solar H/He abundance models with $0.01Z_\odot$, $0.1Z_\odot$ and $Z_\odot$ metallicities, respectively, for three values of surface gravity ($\log g$ = 14.0, 14.3, 14.6). The coloured arrows are meant to show the mass and radius parameter space allowed by a given constraint. To visualize the implication on mass and radius from an upper limit on R_∞, two curves of constant R_∞ are plotted as dotted lines for the highest and lowest values found within solar H/He abundance models. These constraints are independent of the source distance and anisotropy parameters ξ_b, ξ_p.

R_∞ curve for a given model, and finding the maximum value of R which lies above $M = M_\odot$.

As in Chapter 2, we also found multiple peaks in the distributions of the fitting parameters (A, $F_{\rm Edd}$), for models with $Z = Z_\odot$. When we encountered multiple peaks, we only fit Gaussian profiles to the lowest peak in the respective distributions for A and $F_{\rm Edd}$, as was done in Chapter 2. This was only necessary for the two models which have a surface gravity $\log_{10} g = 14.0$, 14.3, as denoted in Table 3.1 by the "e" superscript.

In this updated analysis, we find values for the upper limit on R_∞ that are all higher than those found in the analysis that used the spectral models from Suleimanov et al. (2011b). Across all compositions and surface gravities, the values R_∞ have increased by roughly $10 - 20\%$. We can attempt to understand what accounts for this increase by considering an expression for R_∞ as a function of the fitting parameters, A and $F_{\rm Edd}$, taken from Chapter 2 (equation 19),

$$R_\infty \; = \; 12.0 \text{ km} \, \left(\frac{\alpha}{1/8}\right) \, \left(\frac{A_8}{1.2}\right)^{-4} \left(\frac{F_{\rm Edd,-8}}{4.0}\right)^{-1} \left(\frac{1+X}{1.7}\right)^{-1}. \tag{3.9}$$

The increase in upper limits on R_∞ is large when compared to the modest increase of roughly 1% in the values of f_c, for $F/F_{Edd} < 0.7$, in the new spectral models relative to the old ones (Suleimanov et al., 2012). Since $A \propto f_c^{-1}$, if the only modification in the models was a 1% increase in f_c for all surface fluxes, we would expect to only have a modest $\sim 4\%$ increase in the upper limit on R_∞. However, by using a relativistic treatment for the scattering opacity, the value for the Eddington flux has increased, by $6{-}10\%$, depending on surface gravity. This has the effect of making the slope of the model f_c curves gentler, which causes the GS $1826-24$ data "stretch out" to higher values of $F/F_{\rm Edd}$[2], implying a lower value for $F_{\rm Edd}$. Across all spectral models, the values of $F_{\rm Edd}$ have been lowered by roughly 10%. Since the above expression shows that R_∞ is inversely proportional to $F_{\rm Edd}$, this change yields roughly an additional 10% increase in R_∞. This together with the small increase in the values of f_c yields an estimated increase in R_∞ of $\sim 14\%$, which is consistent with our results.

3.4 Summary and Discussion

We have revisited the lightcurve and spectral model comparisons presented in Chapter 2, where these comparisons were used to constrain the neutron star mass and radius in the regular bursting X-ray binary GS $1826-24$.

The source GS $1826-24$ has been claimed to be a textbook example of mixed H/He bursts, with an overall excellent agreement with theory (Bildsten, 2000; Heger et al., 2007a). Here we have extended the comparison of lightcurve shapes to a wider range of recurrence times and shown that our understanding of this source and its behaviour is incomplete.

We considered a suite of KEPLER models which were expected to fall in the regime of mixed H/He bursts, and found that for the most part, their behaviour followed the theoretical expectations. The only unexpected aspect was the 50% change in the ignition column depth across all recurrence times shown by the lowest metallicity models. Using these KEPLER simulations, we showed that while GS $1826-24$ lightcurves are well described by the solar composition model ($X_0 = 0.7,\ Y_0 = 0.28,\ Z_0 = 0.02$) for recurrence times of 4 hours or less, at longer recurrence times, the trends in peak flux

[2] The models from Suleimanov et al. (2012) are calculated on a grid of $F/F_{\rm Edd}$, where $F_{\rm Edd}$ is the Eddington flux based on the *Thomson* opacity. Therefore their grid extends to values that are $F/F_{Edd} > 1$, without exceeding the actual Eddington limit, which is calculated using the Klein-Nishina cross-section.

show a distinct disagreement. Namely, the peak flux in the KEPLER simulations rises more steeply with recurrence time than what is observed in GS 1826 − 24.

Motivated by the arguments of Fujimoto et al. (1981) regarding the scaling of peak flux in a burst with the average helium mass fraction in the layer at ignition, we looked for and found such a correlation in the suite of mixed H/He KEPLER models. From this correlation, we were able to establish an empirical "law" allowing us to predict the peak flux given an accreted composition and a recurrence time. We used this to argue that the accreted metallicity in GS 1826 − 24 must be lower than previously estimated (Galloway et al., 2004; Heger et al., 2007a), finding $Z_0 \lesssim 0.002 - 0.01$ for a range of $Y_0 = 0.3 - 0.5$. We did not explicitly compare the evolutions in E_b with recurrence time, but argued that a helium-enriched component to the accretion composition is necessary to reproduce the relatively low values of E_b measured in GS 1826 − 24 (see Fig. 3.2). We also argued that the full composition and distance could in practice be constrained from a simultaneous comparison of $F_{\rm peak}$ and E_b.

We found that a low metallicity was needed to reproduce the small slope of $F_{\rm peak}$ with $t_{\rm rec}$ seen in for GS 1826 − 24 bursts. The fact that even the lowest metallicity KEPLER models show upward trends in $F_{\rm peak}$ can be understood as an effect of chemical inertia, which sets an minimum effective metallicity that a model will have. This inertial metallicity is what causes the lowest metallicity models to still have an increasing trend of $F_{\rm peak}$ with $t_{\rm rec}$, albeit lower than models which directly accrete more metals. Galloway et al. (2004) found, using the ignition models of Cumming & Bildsten (2000), that a solar metallicity accretion was required to fit the variations in the parameter α (defined as $\alpha \equiv \int F_{\rm pers} dt / \int F_{\rm burst} dt$, where $F_{\rm pers}$ is the flux during persistent emission) with persistent flux for observations of GS 1826 − 24, but that a metallicity of $Z = 0.001$ was necessary to describe the observed variations of fluence and recurrence time with persistent flux. In Heger et al. (2007a), it was argued that due to thermal and chemical inertia in the KEPLER simulations, a solar metallicity accretion could in fact explain the variations in fluence and recurrence times with respect to accretion rate. What we find is that chemical inertia is sufficiently strong ($Z_{\rm inertial} \simeq Z_{\rm solar}$) that it can provide the necessary metallicity to describe GS 1826−24 lightcurves, without much additional metallicity in the accretion. In fact, accreting an additional amount of solar metallicity leads to an elevated rate of CNO burning, causing the bursts to become too bright in comparison to GS 1826 − 24, which is what we found in §3.2.2.

In §3, we derived new constraints on the mass and radius, from the comparison of updated models of burst spectra (Suleimanov et al., 2012) to observations of GS 1826−24. We found an increase in the derived upper limits on R_∞ by about $10-20\%$, compared to the results of Chapter 2, where we used a previous calculation of burst spectra (Suleimanov et al., 2011a).

In §2, the use of the two burst parameters $F_{\rm peak}$ and E_b enabled us to quantify the shapes of the lightcurves, and enabled a straightforward comparison of simulations to observations. Of course, this is an imperfect approach, as information about lightcurve shape is "lost", particularly for the calculation of the burst energy, E_b, which requires the integration of the luminosity over the duration of the burst. It would be useful to evaluate how well these two parameters characterize the lightcurve shape. For example, while $F_{\rm peak}$ is a unique parameter for a lightcurve, there are many different lightcurve shapes that could yield a similar value of E_b. However, since we restricted our attention to mixed H/He bursts, it may be that the variations in shape for a fixed E_b and $F_{\rm peak}$ are small.

It would also be interesting to verify if the validity of the assumptions that have gone into deriving the empirical relation between $F_{\rm peak}$ and $\overline{Y}$ bear out in the KEPLER simulations. This is left for future work. For example, one could check whether the average helium mass fraction actually scales with recurrence time and composition according to equations (3.5) and (3.6), or whether the amount of mixing of ashes from previous bursts into freshly accreted fuel agrees with the value we found for the parameter $Z_{\rm inertial}$. It is important to note, however, that even if our assumptions do not hold, the trend we have found between $F_{\rm peak}$ and $\overline{Y}$ (eq. 3.7) can still be valuable as an empirical law.

The discrepancy we found in the evolution of the lightcurve shape between KEPLER simulations with $Z_0 = 0.02$ and observations of GS 1826$-$24 is particularly relevant to the results of Chapter 2, where the presumed agreement found by Heger et al. (2007a) was exploited to obtain constraints on the mass and radius of GS $1826-24$. Since this agreement breaks down at different burst recurrence times, it casts doubts on the accuracy of the constraint of the gravitational redshift, $1+z = 1.28 \pm 0.03(f_c/1.5)$ (represented by the green band in Figure 2.5 of Chapter 2).

We can attempt to estimate how this result will affect the constraint on z derived in Chapter 2. Using equations (3.5) and (3.7), our prediction for the peak flux given by a KEPLER simulation with $Z_0 = 0.001$ is

$$F_{\rm peak,25}(t_{\rm rec}, X_0, Y_0) \ = \ 3.4Y_0 + 0.12t_{\rm rec}(1-Y_0)^{-1} - 0.18 \qquad (3.10)$$

where we assumed $t_{\rm rec} \leq t_{\rm CNO}$. In our Chapter 2 derivation, we used a measurement for the blackbody normalization for bursts with a 4 hour recurrence time. To maintain consistency, we must also use this recurrence time in the above expression. From our previous arguments about simultaneous fits to both $F_{\rm peak}$ and E_b, we know the helium mass fraction must be at least higher than $Y_0 = 0.25$. Using the relation $1 = X_0 + Y_0 + Z$, we find that the peak flux for $Y_0 = 0.3$, 0.4, 0.5 will be $F_{\rm peak,25} = 1.5$, 2.0, 2.5, respectively. This increase in the model flux will have the effect of increasing our estimate on the redshift. The value $F_{\rm peak}$ used in Chapter 2 is 1.29×10^{25}erg cm^{-2} s^{-1}, therefore a $\simeq$ 20, 50, 90% increase in the model peak flux would yield a 5, 11 and 17% increase in the redshift, respectively. This estimate suggests that an accreted helium mass fraction of $Y_0 = 0.5$ would imply to a redshift measurement of $z = 1.49$, implying a very compact neutron star.

In this chapter, all the model comparisons were done using $t_{\rm rec}$ as an independent variable. The mapping of accretion rate to persistent flux (or vice versa), is inherently uncertain, making the comparison of simulations to observations difficult. Notably, the conversion is subject to the highly uncertain persistent anisotropy parameter ξ_p (see equation 2.7). Fujimoto (1988) found that ξ_p^{-1} ranges from 0 to 2 across all inclinations. In Lapidus & Sunyaev (1985), a similar range of values was found, however the prediction for the variation of ξ_p with inclination was opposite to what was found in Fujimoto (1988) (see §2.3 of Chapter 2 for a brief overview). Furthermore, the determination of α involves the ratio of ξ_p/ξ_b (see §2.4), which has an even wider range of possible values, varying by up to a factor of 3 (§2.3, Chapter 2). The uncertainty in α and the persistent flux associated with the anisotropy parameters is "multiplicative", in the sense that it can "stretch" or "contract" a set of observations, thereby changing the slopes. For example, in the top panel of Fig. 4 in Galloway et al. (2004), if the persistent emission for the data is increased, the observations could possibly be fit a higher metallicity model curve, instead of the $Z = 0.001$ curve. Due to the uncertainties in comparing modelled and observed persistent emission, we chose to use $t_{\rm rec}$ as an independent variable, since its measurement is very certain. Our analysis is also subject to an uncertainty from the burst anisotropy factor ξ_b, associated with the measurements of $F_{\rm peak}$ and E_b. However, the systematic uncertainty associated with ξ_b can be interpreted as an added uncertainty on the distance, which we have not fixed or attempted to constrain.

We have argued that the accretion composition in GS $1826-24$ is sub-solar in metallicity. This offers another way to resolve a puzzle that is outlined in the Chapter 2 discussion. In Figure 2.3, we showed a comparison of the evolution of $K^{-1/4}$, where K is the blackbody normalization, to spectral model calculations of f_c, the spectral colour correction, during the cooling phase of GS $1826-24$ bursts. There is a notable difference in the observed trend compared to the models with $Z = Z_\odot$, which show a depression in f_c at low fluxes, $F/F_{\rm Edd} \lesssim 0.3$, which is attributed to absorption edges from partially ionized iron in the atmosphere (Suleimanov et al., 2011a). Our result, of a low metallicity accretion in GS $1826-24$, is consistent with a lack of a depression in the observed $K^{-1/4}$ trend. Note however, that the appearance of this depression in observations has recetly been associated with the burst source being in a soft spectral state. Reconciling why the soft state yields spectral evolutions suggestive of a high metallicity composition is an ongoing puzzle (Kajava et al., 2014).

4

The Thermal Stability of Helium Burning in Accreting Neutron Stars

This chapter was published as: M. Zamfir, A. Cumming, C. Niquette, *The Thermal Stability of Helium Burning in Accreting Neutron Stars*. MNRAS, vol. 445, 3278, 12/2014.

4.1 Introduction

Thermonuclear burning of hydrogen (H) and helium (He) on the surface of an accreting neutron star is expected to undergo a transition from being thermally-unstable to thermally-stable at a critical accretion rate $\dot{M}_{\rm crit} \approx 10^{18}$ g s^{-1} (close to the Eddington accretion rate) (Hansen & van Horn, 1975; Fujimoto et al., 1981). The transition occurs because the temperature-dependence of the He burning reactions becomes less steep at higher burning temperatures, so that at a high enough accretion rate the reactions are no longer temperature-dependent enough to overcome the stabilizing radiative cooling of the layer.

Observationally, unstable nuclear burning is seen as Type I X-ray bursts, bright flashes in X-rays with a typical duration of 10–100 seconds that recur on timescales of hours to days (Lewin et al., 1993). Consistent with the idea that the burning stabilizes, the rate of Type I X-ray bursts drops dramatically in several sources above a persistent luminosity $L_X \approx 2 \times 10^{37}$ erg s^{-1} (Cornelisse et al. 2003; see also Clark et al. 1977), and the burst energetics clearly point to most of the accreted fuel burning in a stable manner (van Paradijs et al., 1988; Galloway et al., 2008). Other observed phenomena also point to stable burning at high accretion rates. Stable H/He burning is required in models for superbursts to produce the carbon fuel that is believed to drive those events (Schatz et al., 2003; Woosley et al., 2004; Stevens et al., 2014), and is manifested in the energetics of Type I X-ray bursts observed from superburst sources (in't Zand et al., 2003). The mHz QPOs observed in some sources (Revnivtsev et al., 2001; Altamirano et al., 2008; Linares et al., 2012) have been identified with an oscillatory mode of nuclear burning that emerges when the burning is marginally-stable, i.e. transitioning between stable and unstable (Heger et al., 2007b; Keek et al., 2014).

Despite this qualitative agreement, a long-standing puzzle has been that the observed accretion rate at which the onset of stable burning occurs is $\dot{M} \sim 10^{17}$ g s^{-1}, an order of magnitude lower than theory predicts. Several mechanisms have been suggested to account for this discrepancy, including a change in burning mode to slowly propagating fires around the neutron star surface (Bildsten, 1995), partial covering of the accreted fuel (Bildsten, 1998), mixing of fuel driven by rotational instabilities (Fujimoto et al., 1987b; Piro & Bildsten, 2007; Keek et al., 2009), and strong heating of the layer associated with spin-down and spreading of the fuel following disk accretion (Inogamov & Sunyaev, 1999, 2010).

The proposal that the unstable burning is quenched by heating is intriguing because evidence has accumulated that the outer crust and ocean of accreting neutron stars are strongly heated by an unknown shallow heat source. One piece of evidence is from superbursts, whose observed ignition properties require temperatures of $\approx 6\times10^8$ K be achieved at column depths of $\approx 10^{12}$ g cm^{-2} in the neutron star ocean, requiring an additional source of heat be added to models (Brown, 2004; Cumming et al., 2006). This problem has been exasperated recently with observations of superbursts in transient systems (Keek et al., 2008; Altamirano et al., 2012). The second piece of evidence is from modelling of the thermal relaxation of transiently-accreting neutron stars in quiescence. Brown & Cumming (2009) found that the temperatures observed in KS 1731-260 and MXB 1659-29 approximately one month into quiescence required an inwards heat flux into the neutron star crust and a corresponding strong shallow heat source. Degenaar et al. (2013) reached a similar conclusion based on rapid cooling of XTE J1709-267 after a short 10 week outburst. Schatz et al. (2014) showed that a strong neutrino cooling source may operate in the outer crust, emphasizing the need for additional heating at shallow depths. Finally, modelling of X-ray burst recurrence times in a number of sources has suggested that outwards fluxes of ~ 0.3 MeV per nucleon[1] or more heat the accumulating H/He layer (Cumming, 2003; Galloway & Cumming, 2006).

Determining the dependence of $\dot{M}_{\rm crit}$ on the base flux is critical to assess whether shallow heating could also be the reason for stabilization of Type I X-ray bursts at observed accretion rates $\dot{M} \gtrsim 10^{17}$ g s^{-1}. Most calculations of the critical accretion rate $\dot{M}_{\rm crit}$ in the literature are for a fixed base flux, typically $Q_b \approx 0.1$ MeV per nucleon (taken from models of the global thermal state of the neutron star, e.g. Brown 2000) for which $\dot{M}_{\rm crit} \approx 10^{18}$ g s^{-1} (e.g. Heger et al. 2007b; Keek et al. 2014). Bildsten (1995) calculated the effect of a flux from deep carbon burning on the stability of the

[1] Throughout the chapter we will measure the heat flux in units of the equivalent energy per accreted nucleon Q_b in MeV per nucleon, so that the flux is $F = Q_b\dot{m}$, where $\dot{m}$ is the local accretion rate $\dot{m} = \dot{M}/4\pi R^2$.

helium shell using a one-zone approach and Fushiki & Lamb (1987a) also included the base temperature as a parameter in their one-zone study. Keek et al. (2009) calculated the stability boundary for pure helium accretion using detailed multizone models for several different base fluxes, showing that an increased heating rate decreases $\dot{M}_{\rm crit}$. They found that a base luminosity of $L_{\rm crust} \approx 10^{35}$ erg s^{-1} (approximately 1 MeV per nucleon at 0.1 Eddington) lowered the critical accretion rate to $\approx 10^{17}$ g s^{-1}. Analogous simulations varying base flux for H/He accretion have not been carried out. When the accreted material contains a significant amount of hydrogen, the burning proceeds via the rp-process involving hundreds of nuclei (Wallace & Woosley, 1981) and so calculations are much more numerically-intensive and so far have been carried out only for specific choices of base flux (Schatz et al., 1998; Woosley et al., 2004; Keek et al., 2014).

In this chapter, we take some further steps towards calculating and understanding the variation of $\dot{M}_{\rm crit}$ with base flux. For simplicity, we consider only pure helium accretion, but with the goal of developing techniques that can be readily applied to the mixed H/He accretion case later. We first use the stellar evolution code MESA (Paxton et al., 2011, 2013) to confirm the results of Keek et al. (2009) for pure helium accretion. We then extend the one-zone model of Bildsten (1998) to include a base flux, which we use to understand the shape of the relation between $\dot{M}_{\rm crit}$ and Q_b, and to derive useful fitting formulae. In the second part of the chapter, we investigate two different methods that have been proposed to determine the stability of the nuclear burning based purely on a steady-state model at a given accretion rate, rather than running time-dependent simulations. This is potentially very powerful because steady-state models can be calculated quickly even when rp-process burning is included (e.g. see the large grid of steady-state models recently calculated by Stevens et al. 2014).

An outline of the chapter is as follows. The time-dependent simulations of helium accretion and one-zone analysis are presented in §4.2. In §4.3, we discuss the relation between the burning depth in steady-state models and the thermal stability of the model. In §4.4, we develop a linear stability analysis of steady-state models and compare to the time-dependent results from MESA. We conclude in §4.5, where we also discuss the application of our results to the ultracompact X-ray binary 4U 1820-30.

4.2 The effect of base heating on the stability boundary

We start in this section by calculating the critical accretion rate $\dot{M}_{\rm crit}$ for pure helium accretion as a function of the base flux Q_b. The results of our time-dependent simulations are presented in §4.2.1, and a one-zone model is developed in §4.2.2 to help to understand the results.

4.2.1 Time dependent calculations with MESA

One of the exciting developments in stellar astrophysics in recent years has been the release of the open source stellar evolution code MESA (Modules for Experiments in Stellar Astrophysics) (Paxton et al., 2011, 2013). MESA solves the equations of stellar evolution in a fully-coupled way, and includes the relevant microphysics for the outer layers of a neutron star relevant for Type I X-ray bursts. Indeed, a sequence of helium flashes on an accreting neutron star was modelled in Paxton et al. (2011), and accretion onto a neutron star is a standard test case in the MESA distribution. We apply MESA here to determine the stability boundary for pure helium accretion. We view this as a straightforward first step to developing MESA as a general tool to study X-ray bursts on accreting neutron stars. Here, we will present only our results on the

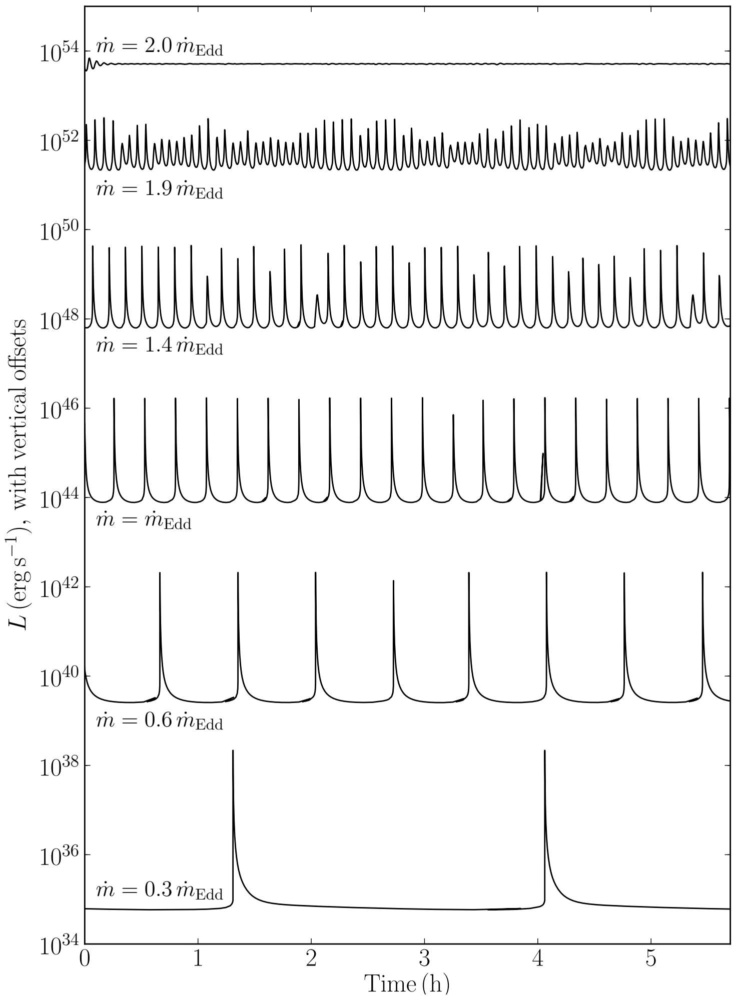

Figure 4.1 Lightcurve profiles generated by MESA showing stable burning and various bursting behaviours at different accretion rates. All models are computed with a base flux of $Q_b = 0.1\,\mathrm{MeV\,nuc^{-1}}$. In going from $\dot{m} = 1.9\dot{m}_{\rm Edd}$ to $\dot{m} = 2.0\dot{m}_{\rm Edd}$, the amplitude abruptly changes from $\Delta L/L \approx 10$ to roughly zero, illustrating the fact that modest variations to the instability criterion we used ($\Delta L/L > 2$) do not strongly affect the location of the stability boundary.

stability boundary, leaving a detailed analysis of burst sequences and the evolution of the burning layers during a burst for a future paper.

We used the MESA release 6596 for our simulations. To enable a meaningful comparison with one-zone models and linear stability analysis (§4.4), we used a simplified nuclear network that takes into account only the triple alpha reaction $3\alpha \rightarrow ^{12}\mathrm{C}$, so that only two species, He and carbon, were present. For determining the stability boundary, this is in fact a good approximation: we also tried using the approx21 network that includes a sequence of helium burning reactions to heavier elements, and found that the critical accretion rate changed by $\lesssim 10\%$ with the change of network. The reason for this is that the burning temperature at the stability boundary, $T \approx 3$–4×10^8 K, is small enough that the burning does not proceed significantly past carbon (e.g. Brown & Bildsten 1998).

From this point onwards, we will use local values for the accretion rate. We adopt a standard value for the local Eddington accretion rate, $\dot{m}_{\mathrm{Edd}} = 8.8 \times 10^4$ g cm^{-2} s^{-1} (the equivalent global accretion rate is $\dot{M}_{\mathrm{Edd}} = 1.11 \times 10^{18}$ g s^{-1} $= 1.74 \times 10^{-8}$ $M_\odot$ yr^{-1}). This corresponds to the Eddington rate for solar composition; we use it here as a standard value even though our simulations are for pure helium accretion. We assume a 1.4 $M_\odot$, 10 km neutron star, which has a surface gravity of $g = 1.9 \times 10^{14}\,\mathrm{cm\,s^{-2}}$. This is the Newtonian value for the surface gravity, and does not include the general relativistic correction; however the dependence of the critical accretion rate on gravity is weak (see §4.4.2).

To find the critical accretion rate, we followed these steps. For each choice of Q_b and $\dot{m}$, we first accrete a column 10^{10} g cm^{-2} of carbon, allowing the model to thermally adjust to the base luminosity. We then accrete an additional column of 10^{10} g cm^{-2} of pure helium. Since the burning depth is $\sim 10^8$ g cm^{-2}, this means that we accrete a column of roughly one hundred burning depths which allows the initial transient behaviour to die away at the beginning of the run. We then assess whether the burning has stabilized by looking at the range of luminosities in the last 10% of the lightcurve. If the luminosity variation is smaller than a factor of $\Delta L/L = 2$ then we classify the burning as stable. We have checked that our derived stability boundary does not significantly change if we use another value for $\Delta L/L$. For each Q_b, we start at a large accretion rate and run successive models with accretion rate reduced in steps of $\Delta \log_{10} \dot{m}/\dot{m}_{\rm Edd} = 0.025$, until the burning becomes unstable, which means that we have located the stability boundary. Figure 4.1 shows that, for a base flux $Q_b = 0.1\,{\rm MeV}$ per nucleon, the initially stable behaviour transforms to a sequence of bursts below $2\,\dot{m}_{\rm Edd}$, with the burst recurrence time and amplitude growing as the accretion rate is lowered further.

The stability boundary as a function of base flux is shown in Figure 4.2. We see a smooth decrease in $\dot{m}_{\rm crit}$ with Q_b, reaching 0.1 $\dot{m}_{\rm Edd}$ at $Q_b \approx 0.7$ MeV. The results of Keek et al. (2009) are shown as a comparison (note that Keek et al. 2009 present these results as luminosity against $\dot{m}$, see their Figure 11, here we have divided the luminosity by $\dot{m}$ to convert the luminosity to MeV per nucleon units). The agreement is good, with typical deviations of tens of percent, although the point at $Q_b \approx 0.8\,{\rm MeV}$ from Keek et al. (2009) is a factor of 2 higher than the MESA result.

4.2.2 One zone model

To understand the shape of the $\dot{m}_{\rm crit}(Q_b)$ relation, it is helpful to consider a one-zone model with a base flux included. In a one-zone treatment of the burning layer, we follow the layer temperature and column depth according to

$$c_P \frac{dT}{dt} = \epsilon_{3\alpha} - \epsilon_{\rm cool} + \frac{Q_b \dot{m}}{y}, \tag{4.1}$$

$$\frac{dy}{dt} = \dot{m} - \frac{\epsilon_{3\alpha}}{E_{3\alpha}} y \tag{4.2}$$

(Paczynski, 1983a; Bildsten, 1998; Heger et al., 2007b), where $\epsilon_{3\alpha}$ is the heating rate and $E_{3\alpha}$ is the energy per unit mass released from 3α reactions, and the one-zone cooling rate is $\epsilon_{\rm cool} \approx acT^4/3\kappa y^2$. Heating from beneath the layer is represented by the third term on the right side of equation (4.1) (Heger et al., 2007b).

To derive the stability boundary, we consider steady-state solutions of equations (4.1) and (4.2) and perturb them, taking the perturbations to be at constant pressure and column depth (since column depth $y = P/g$ in a thin layer). We follow Bildsten (1998) and assume an ideal gas equation of state, so that $\delta\rho/\rho = -\delta T/T$ at constant pressure. This gives

$$\begin{aligned} c_P \frac{d\delta T}{dt} &= \delta\epsilon_{3\alpha} - \delta\epsilon_{\rm cool} \\ &= \frac{\delta T}{T} \left[\epsilon_{3\alpha} \left(\nu - \eta\right) - \epsilon_{\rm cool} \left(4 - \kappa_T\right)\right] \end{aligned} \tag{4.3}$$

where we have expressed the heating rate as $\epsilon_{3\alpha} \propto \rho^\eta T^\nu$, and $\kappa_T = \partial \ln \kappa / \partial \ln T|_P$. For triple alpha burning, $\nu \approx (44/T_8) - 3$ and $\eta = 2$, where $T_8 = T/10^8$ K (Hansen & Kawaler, 1994).

When the base heat flux is much smaller than the energy generated inside the layer, the steady-state obeys $\epsilon_{3\alpha} \approx \epsilon_{\rm cool}$, and the condition for instability ($d\delta T/dt > 0$) is

$$\nu - \eta - 4 + \kappa_T = \frac{44}{T_8} - 9 + \kappa_T > 0 \tag{4.4}$$

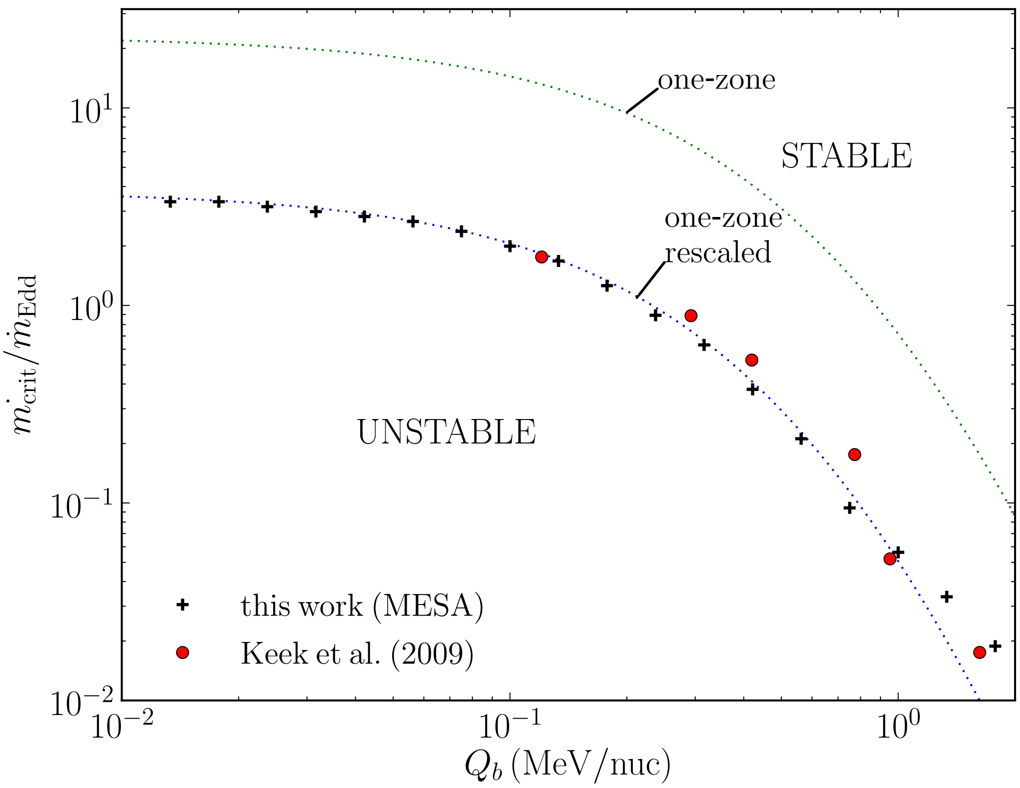

Figure 4.2 The stability boundary we find using MESA (black crosses) agrees well with the boundary found by Keek et al. (2009) (red circles). The analytically-derived one-zone estimate to the stability boundary (equation 4.9) is shown as a green dotted curve. The one-zone curve shares a similar shape to, but overestimates the values of the MESA data. By making small adjustments to equation (4.9) (see text), we obtain an analytic fit to the MESA results (equation 4.10), shown as the blue dotted curve.

(e.g. Bildsten 1995, 1998; Yoon et al. 2004). When the base flux is significant, $\epsilon_{3\alpha}$ is no longer equal to $\epsilon_{\rm cool}$, and in fact is smaller since the base flux Q_b now contributes to the heating of the layer. The instability condition is

$$\nu - \eta - \frac{\epsilon_{\rm cool}}{\epsilon_{3\alpha}} (4 - \kappa_T) > 0. \tag{4.5}$$

In steady-state, equation (4.1) gives $\epsilon_{\rm cool} = \epsilon_{3\alpha} + \dot{m}Q_b/y$, and the burning depth is given by equation (4.2) as $y/\dot{m} = E_{3\alpha}/\epsilon_{3\alpha}$. Therefore

$$\frac{\epsilon_{\rm cool}}{\epsilon_{3\alpha}} = 1 + \frac{Q_b}{E_{3\alpha}} = 1 + \frac{Q_b}{0.61\ {\rm MeV}}. \tag{4.6}$$

We see that when Q_b is significant, the cooling term in the instability criterion is enhanced. This implies that to trigger a burst in the presence of a base flux, the temperature in the layer must be lower than without the base flux, so that ν is larger and able to overcome the cooling term. The effect of Q_b is therefore to lower $\dot{m}_{\rm crit}$ compared to its $Q_b = 0$ value, as seen in the MESA results in Figure 4.2.

Setting the equality in equation (4.5) gives an expression for the critical temperature below which helium burning becomes unstable in the one-zone model,

$$T_{\rm crit,\,8} = 4.9\ \left[\frac{5}{9} + \frac{4-\kappa_T}{9}\left(1 + \frac{Q_b}{0.61\ {\rm MeV}}\right)\right]^{-1}. \tag{4.7}$$

Setting Q_b and κ_T to zero, we recover the critical temperature for stable helium burning found by Bildsten (1998), $T_{\rm crit,\,8} = 4.9$. Equation (4.7) confirms that the inclusion of a base heating flux reduces the critical temperature required for the onset of unstable burning. As Keek et al. (2009) noticed, $T_8 = 4.9$ is well above the burning temperature at marginal stability in multizone time-dependent calculations

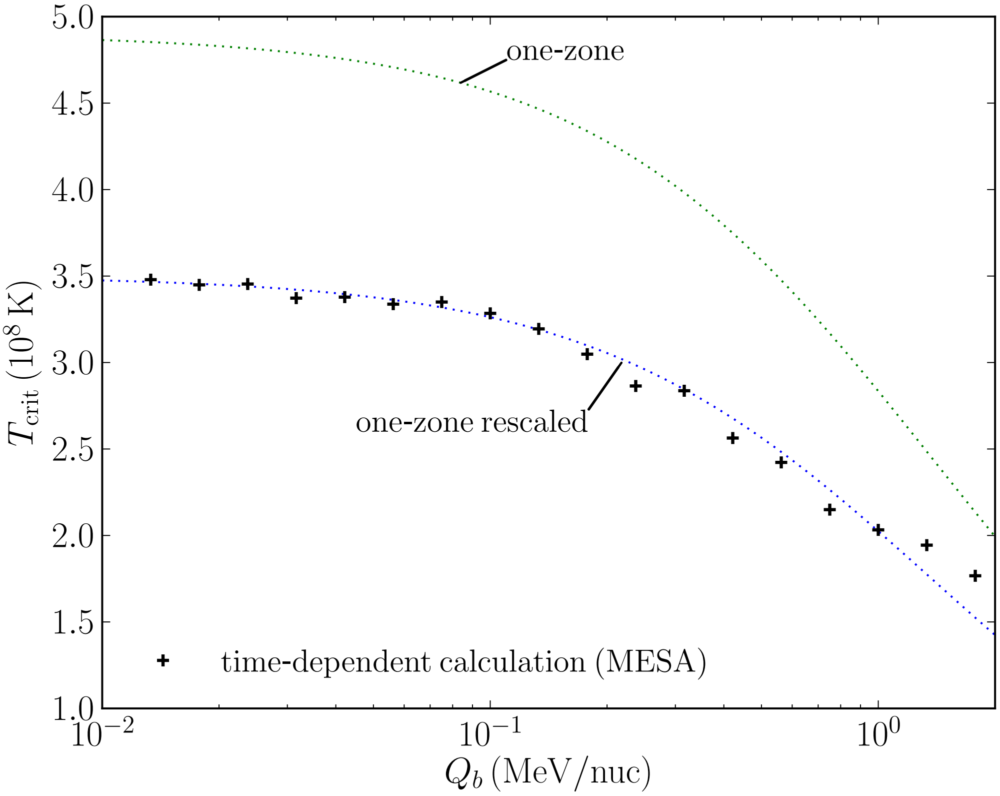

Figure 4.3 The temperature at the triple-alpha burning depth along the MESA stability boundary is shown in black crosses. Sharing a similar shape but with higher values, the one-zone analytical estimate to the critical temperature (equation 4.7) is shown as a dotted green line. By changing the prefactor in equation (4.7) from 4.9 to 3.5, we find a good fit to the MESA data, allowing us to establish a simple analytical expression for the burning temperature at the critical accretion rate.

(see Figure 4.3). However since the shapes of the one-zone and MESA curves agree well, we can adjust the prefactor in equation (4.7) from 4.9 to 3.5 to obtain a simple analytical expression that describes the burning temperature at the critical accretion rate in MESA (shown as a blue dotted curve in Figure 4.3).

We can now find $\dot{m}_{\rm crit}$ at a given Q_b by calculating the accretion rate at which the burning temperature is equal to the value in equation (4.7). To do so, we can use the following expression (Bildsten, 1998, equation 19) which gives the temperature at the helium burning depth in steady-state,

$$T_{\rm burn} = 2.8 \times 10^8 \ {\rm K} \ \left(\frac{\dot{m}}{\dot{m}_{\rm Edd}}\right)^{1/5} \left(1 + \frac{Q_b}{0.61 \ {\rm MeV}}\right)^{3/20}, \tag{4.8}$$

where we assume pure helium composition and other appropriate parameters ($\mu = 4/3$, $E_{18} = 0.58$, $g_{14} = 1.9$) and have written the flux heating the layer in terms of Q_b. The scalings in this expression indicate that a reduction in the critical temperature required for instability implies a reduction in the accretion rate, for a constant base flux. Equating the temperatures in equations (4.7) and (4.8), we find the critical accretion rate

$$\dot{m}_{\rm crit} = 16 \ \dot{m}_{\rm Edd} \ \left(1 + \frac{Q_b}{0.61 \ {\rm MeV}}\right)^{-3/4} \left(1 + \frac{Q_b}{1.37 \ {\rm MeV}}\right)^{-5}, \tag{4.9}$$

where we again set $\kappa_T = 0$.

We have checked equation (4.9) by running time-dependent one zone models, solving equations (4.1) and (4.2) in time. We include electron scattering, free-free, and conductive opacities following Schatz et al. (1999) and Stevens et al. (2014), the 3α burning rate from Fushiki & Lamb (1987b), and we used fitting formulae for the contributions of degenerate and relativistic electrons to the equation of state from Paczynski (1983b). We use a similar method to the MESA runs described in §4.2.1 to determine from the lightcurve whether the burning is stable or unstable. We find that the analytic expression in equation (4.9) underestimates the time-dependent one-zone $\dot{m}_{\rm crit}$ by 30–50% across the range of Q_b. These differences are mostly due to the assumptions of constant opacity $\kappa = 0.136 \ {\rm cm^2 \ g^{-1}}$ and ideal gas equation of state that go into equation (4.8). We have confirmed this by running time-dependent models that adopt the same assumptions. At low accretion rates and fluxes $Q_b \gtrsim 1$ MeV, another source of error is that the approximation $\exp(-44/T_8) \approx 2.22 \times 10^{-6}(T_8/3.38)^{13}$ used by Bildsten (1998) to expand the triple alpha burning rate as a power law begins to break down.

We find that adjusting the prefactor in equation (4.9) to 23 $\dot{m}_{\rm Edd}$ reproduces the full time-dependent one-zone model to within $10-20\%$, and this is plotted as a green dotted curve in Figure 4.2.

4.2.3 Analytic expression for $\dot{m}_{\rm crit}(Q_b)$

Comparing the one-zone result with the MESA calculation in Figure 4.2 shows that the overall shape of the curve is reproduced well by the one-zone model, but the magnitude of $\dot{m}_{\rm crit}$ is overestimated by a factor of approximately 5. This factor is similar to the difference between the $\dot{m}_{\rm crit} = 16\ \dot{m}_{\rm Edd}$ found by Bildsten (1995) and the $\dot{m}_{\rm crit} \approx 3\ \dot{m}_{\rm Edd}$ found by Keek et al. (2009). The inaccuracy of the one-zone model comes from the instability criterion equation (4.5) which overestimates the critical temperature for stable burning (eq. [4.7]). Equation (4.8) for the burning temperature of the layer, which comes from an analytic integration of the temperature profile in the layer, is quite accurate. For example, at the low flux stability boundary $\dot{m} = 3.5\ \dot{m}_{\rm Edd}$, equation (4.8) predicts $T_8 = 3.6$ which agrees well with the burning temperature (see Fig. 4.3).

To obtain an analytic fit to the MESA results, we rescaled equation (4.9) by adjusting the prefactor and making a small adjustment to the numerical constant inside the final term to improve the fit at intermediate values of Q_b. The final result, shown in Figure 4.2 as a blue dotted curve, is

$$\dot{m}_{\rm crit} = 3.8\,\dot{m}_{\rm Edd}\ \left(1 + \frac{Q_b}{0.61\ {\rm MeV}}\right)^{-3/4}\left(1 + \frac{Q_b}{0.95\ {\rm MeV}}\right)^{-5}, \tag{4.10}$$

which reproduces the MESA results to within $\lesssim 10\%$ for $Q_b \leq 1$ MeV.

4.3 The relation between the steady-state burning depth and stability

In this section we investigate the relation between the burning depth in steady-state models and thermal stability. Paczynski (1983a) pointed out that in one-zone models, the burning depth $y_{\rm burn}$ decreases with $\dot{m}$ for unstable models ($dy_{\rm burn}/d\dot{m} < 0$), but increases with $\dot{m}$ in stable models ($dy_{\rm burn}/d\dot{m} > 0$). The stability boundary is therefore at the turning point $dy_{\rm burn}/d\dot{m} = 0$. Narayan & Heyl (2003) argued that the same criterion should apply to multizone models also, but they only considered the case $Q_b = 0$. If this result is generally true, it would be a very powerful way to determine the stability boundary without doing any time-dependent calculations, and large grids of steady-state models already exist as functions of $\dot{m}$, Q_b and accreted composition (helium fraction) (Stevens et al., 2014).

We first discuss the one-zone case in §4.3.1, extending the arguments of Paczynski (1983a) to the case with $Q_b > 0$. We then consider multizone models in §4.3.2. We show that in both cases $dy_{\rm burn}/d\dot{m}$ is non-zero at marginal stability, and so $dy_{\rm burn}/d\dot{m} = 0$ can be used to locate the marginally stable point only for one-zone models with $Q_b = 0$.

4.3.1 The turning point and stability of one-zone models

First consider the case studied by Paczynski (1983a), a sequence of one-zone models with increasing $\dot{m}$, and $Q_b = 0$. From equations (4.1) and (4.2), these models must obey

$$\epsilon_{3\alpha} = \epsilon_{\rm cool}, \tag{4.11}$$

$$\dot{m} = \frac{\epsilon_{3\alpha}}{E_{3\alpha}} y, \tag{4.12}$$

in steady-state. At the accretion rate where $dy_{\rm burn}/d\dot{m} = 0$, two neighbouring steady-state models which differ in accretion rate by an amount $\Delta\dot{m}$ have the same burning depth, so $\Delta y_{\rm burn} = 0$. Equation (4.12) then gives $\Delta\dot{m} = (y/E_{3\alpha})\Delta\epsilon_{3\alpha}$. Since the column depth remains unchanged, the difference in accretion rates between the two models is accommodated by a change in the burning rate driven by a temperature difference at constant pressure (column depth), $\Delta\epsilon_{3\alpha} = (\nu - \eta)\epsilon_{3\alpha}\Delta T/T$. The temperature difference between the two models also implies a difference in cooling rates $\Delta\epsilon_{\rm cool} = (4 - \kappa_T)\epsilon_{\rm cool}\Delta T/T$, and so setting $\Delta\epsilon_{3\alpha} = \Delta\epsilon_{\rm cool}$ as must be the case for two steady-state models, we arrive at

$$(\nu - \eta) = (4 - \kappa_T)\,, \tag{4.13}$$

exactly the criterion for marginal stability (see eq. [4.4]). Therefore, we have shown that the steady-state model with $dy_{\rm burn}/d\dot{m} = 0$ is marginally stable.

When a base flux is included, equation (4.11) becomes

$$\epsilon_{3\alpha} + \frac{Q_b\dot{m}}{y} = \epsilon_{\rm cool}. \tag{4.14}$$

Two neighbouring models at $dy_{\rm burn}/d\dot{m} = 0$ are still related by $\Delta\dot{m} = (y/E_{3\alpha})\Delta\epsilon_{3\alpha}$ because equation (4.12) has not changed, but from equation (4.14), they must now satisfy

$$\Delta\epsilon_{3\alpha} + \frac{Q_b}{y}\Delta\dot{m} = \Delta\epsilon_{3\alpha}\left(1 + \frac{Q_b}{E_{3\alpha}}\right) = \Delta\epsilon_{\rm cool} \tag{4.15}$$

or

$$\epsilon_{3\alpha}\left(1 + \frac{Q_b}{E_{3\alpha}}\right)(\nu - \eta) - \epsilon_{\rm cool}\,(4 - \kappa_T) = 0. \tag{4.16}$$

But the steady-state model obeys $\epsilon_{3\alpha}(1 + Q_b/E_{3\alpha}) = \epsilon_{\rm cool}$ (eq. [4.6]), giving again

$$(\nu - \eta) = (4 - \kappa_T) \tag{4.17}$$

at the accretion rate where $dy_{\rm burn}/d\dot{m} = 0$. But for $Q_b > 0$ this is no longer the condition for marginal stability (see eq. 4.5). Therefore the turning point for $y_{\rm burn}$ no longer specifies the stability boundary when $Q_b > 0$.

It is curious that at the turning point for any value of Q_b, the criterion for marginal stability at $Q_b = 0$ (eq. [4.17]) is satisfied. This means that models where $dy_{\rm burn}/d\dot{m} = 0$ for any value of Q_b will have the same burning temperature $T_8 = 4.9$ at which equation (4.17) is satisfied.

4.3.2 The turning point and stability of multizone models

To locate the turning point $dy_{\rm burn}/d\dot{m} = 0$ in the multizone case, we constructed a set of steady-state models of the helium burning layer as a function of Q_b and $\dot{m}$. We solve for the temperature T, helium mass fraction Y, and flux F as a function of column depth y by integrating (see Brown & Bildsten 1998)

$$\frac{dT}{dy} = \frac{3\kappa F}{4acT^3} \tag{4.18}$$

$$\frac{dF}{dy} = -\epsilon_{3\alpha} + \frac{\dot{m}c_P T}{y}\left(\nabla - \nabla_{\rm ad}\right) \tag{4.19}$$

and

$$\frac{dY}{dy} = -\frac{12\epsilon_{3\alpha}}{\dot{m}Q_{3\alpha}}, \tag{4.20}$$

where $Q_{3\alpha} = 7.275$ MeV is the energy release from one triple-alpha reaction. We assume that helium burns to carbon only, with the triple-alpha generation rate $\epsilon_{3\alpha}$, opacity κ and equation of state calculated in the same way as in §4.2.2. The boundary conditions are $Y = 1$ at the top of the layer, and $F = Q_b\dot{m}$ at the base. The flux at the top has contributions from Q_b, the nuclear burning, and the compressional heating, described by the term involving $\nabla_{\rm ad} - \nabla$ on the right hand side of equation (4.19). Since the compressional heating depends on the temperature profile, it is necessary to iterate the solution until the assumed compressional heating is self-consistent.

For our steady-state models, we set the lower boundary at $y = 10^{11}$ g cm^{-2}. This is deep enough that helium burning is complete at the base. As Figure 4.4 shows, the helium burning depth is typically $10^8\,{\rm g\,cm^{-2}}$, but can reach $10^{10}\,{\rm g\,cm^{-2}}$ at $\dot{m} \sim 1\%\,\dot{m}_{\rm Edd}$ and $Q_b \lesssim 0.1\,{\rm MeV\,nuc^{-1}}$. Our inner boundary also lies above the depth where carbon is likely to burn (Brown & Bildsten, 1998). Furthermore, the temperature profile is expected to turn over at some point, with heat being transported into the crust and core. We stop our integrations at a depth shallower than both the temperature turn over point, and the carbon ignition depth. The value of Q_b should be interpreted as the outwards flux evaluated at the lower boundary depth, $y = 10^{11}\,{\rm g\,cm^{-2}}$.

The compressional heating gives some sensitivity to the choice of the location of the lower boundary. Beneath the helium burning depth, the layer is close to isothermal,

∇ is much smaller than $\nabla_{\rm ad}$, and $c_P T \nabla_{\rm ad}$ is roughly constant allowing an estimate of the contribution to the flux from compressional heating,

$$\frac{dQ_{\rm comp}}{d\log_{10} y} = 0.013\,\frac{\rm MeV}{\rm nuc}\,T_9 \left(\frac{c_p}{3.0\times 10^7\,{\rm erg\ g^{-1}\,K^{-1}}}\right)\left(\frac{\nabla_{\rm ad}}{0.4}\right), \tag{4.21}$$

where we take a typical value of c_P from our numerical models. Every additional decade in column depth included below the helium burning depth contributes an extra 0.013 MeV per nucleon. This means that models with small $Q_b \ll 0.1$ MeV per nucleon actually have a flux heating the helium burning layer that is substantially larger than Q_b. In other words, compressional heating in the ocean sets an effective lower limit on the base heating of the helium burning layer. The contributions to the total compressional heat flux are roughly evenly divided between depths below and above the helium burning depth. From equation (4.21), we estimate the contribution from below to be $\sim 0.04\,$MeV/nuc for a typical burning depth and our choice of lower boundary, which gives a total $Q_{\rm comp} = 0.08\,$MeV/nuc.

Figure 4.4 shows contours of the burning depth and temperature. We define the burning depth $y_{\rm burn}$ as the location where the 3α burning rate is maximal. The burning temperature $T_{\rm burn}$ is defined as the temperature at the depth $y_{\rm burn}$. The stability boundary as calculated in §4.2.1 is shown. Clearly, $dy_{\rm burn}/d\dot{m} < 0$ along the stability boundary. Interestingly, the locus of points where $dy_{\rm burn}/d\dot{m} = 0$ (where the blue contours turn over) follows closely the temperature contour where $\log_{10} T = 8.7$ or $T_8 = 5$, as the arguments from the one-zone model indicated. We conclude that the correspondance between $dy_{\rm burn}/d\dot{m} = 0$ and marginal stability does not carry over into multizone models for any value of Q_b.

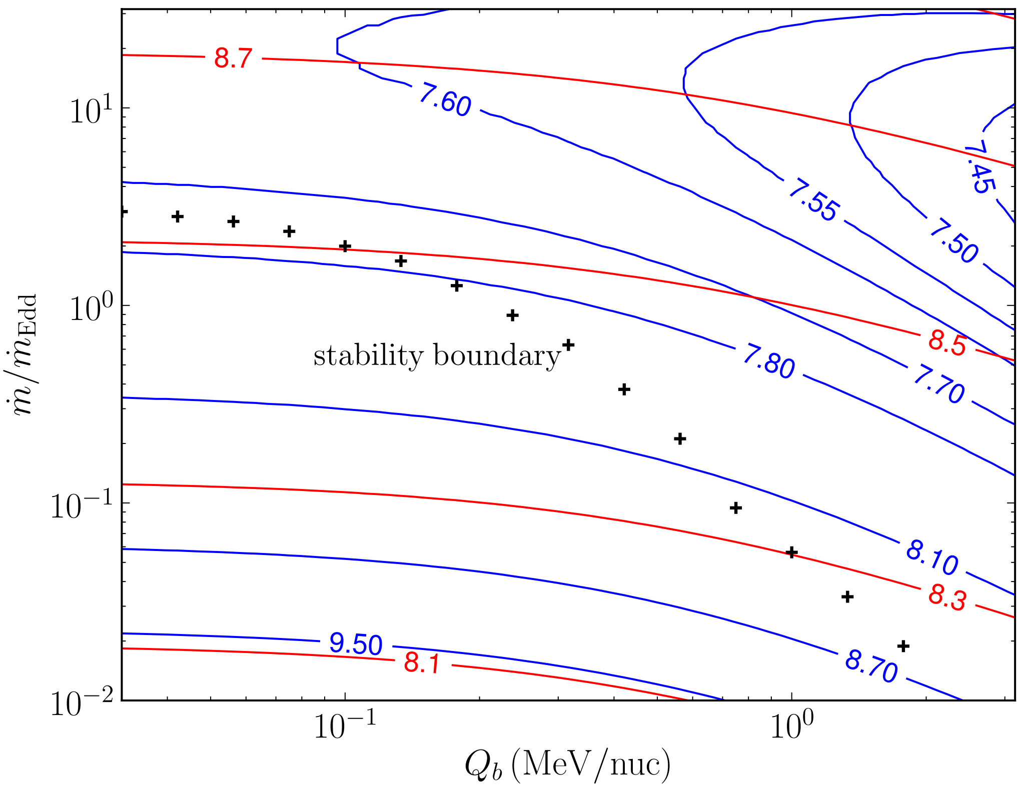

Figure 4.4 Contour lines for constant values of burning column depth ($y_{\rm burn}$; blue lines), that is, the depth at which the triple-α burning rate peaks, and temperature at the burning depth ($T_{\rm burn}$; red lines). The numbered labels on the contours show the base-10 logarithm of the respective quantities. Note that the $\log_{10} T_{\rm burn} = 8.7$ contour line appears to very nearly pass through the stationary points of the $y_{\rm burn}$ contour curves, that is, where $dy_{\rm burn}/d\dot{m} = 0$. This is addressed in §4.3.1.

4.4 Linear stability analysis

In this section, we carry out a linear stability analysis of the steady-state models described in §4.3.2. A similar technique was used by Narayan & Heyl (2003), although applied to artificially truncated steady state models in an attempt to calculate ignition conditions in the unstable regime. Here, we are interested in locating the stability boundary and so perturb full steady-state models that burn to completion. This technique should reproduce the stability boundary, since we will identify those values of $\dot{m}$ and Q_b where the steady-state model is unstable.

We first derive the perturbation equations and boundary conditions in §4.4.1, and present the results in §4.2.

4.4.1 Perturbation equations

For the perturbation analysis, we use pressure or equivalently column depth as the independent coordinate (pressure and column depth are related by $P = gy$ in a thin layer, where g is the constant gravity). At each pressure P, we set $T \rightarrow T + \delta T$ and $F \rightarrow F + \delta F$, where the perturbations have a time-dependence $e^{\gamma t}$. With the choice of pressure coordinates, we are adopting Lagrangian perturbations. In the Appendix, we derive the perturbation equations from an Eulerian approach, in which vertical displacements are followed explicitly. We assume that on the timescale of the thermal perturbation, the composition does not change $\delta Y = 0$, since only a small amount of helium need burn for a large change in temperature (see eqs. [4.1] and [4.2]).

Putting the time-dependent term $c_P \partial T/\partial t$ back into equation (4.19) and perturbing, we find

$$\frac{d}{dy}\delta F = \left(c_P\gamma - \frac{\epsilon_{3\alpha}\epsilon_T}{T}\right)\delta T \tag{4.22}$$

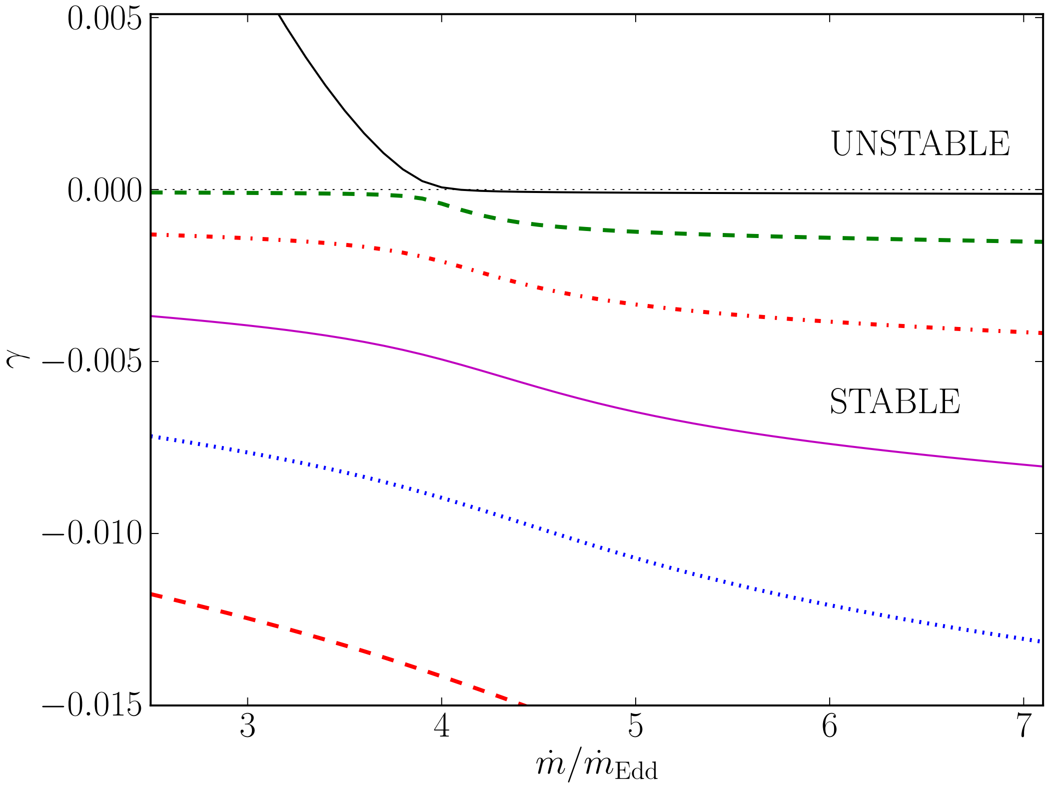

Figure 4.5 The change in eigenvalue γ with accretion rate for the first few eigenmodes using a $Q_{base} = 0.2$ MeV. The first eigenmode (black line) transitions from unstable ($\gamma > 0$) to stable as the accretion rate increases past $\sim 4\dot{m}_{\rm Edd}$. The other eigenmodes are stable across all accretion rates. A horizontal dotted black line is used to highlight the location of the transition, $\gamma = 0$.

where $\epsilon_T = \partial \ln \epsilon_{3\alpha}/\partial \ln T|_P$ and we have neglected the compressional heating term. The radiative diffusion equation (4.18) gives

$$\frac{d}{dy}\delta T = \frac{dT}{dy}\left(\frac{\delta F}{F} + \left[\frac{\kappa_T - 3}{T}\right]\delta T\right) \tag{4.23}$$

where $\kappa_T = \partial \ln \kappa/\partial \ln T|_P$. For a given steady-state model $(T(y), Y(y), F(y))$ obtained by integrating equations (4.18)–(4.20), the perturbation equations (4.22) and (4.23) form an eigenvalue problem for γ, i.e. the perturbation equations and their boundary conditions will be satisfied only for particular choices of the growth (or decay) rate γ.

At the top of the layer, the boundary condition comes from perturbing a radiative zero solution ($F = acT^4/3\kappa y$) for the outer layers, giving

$$\frac{\delta F}{F} = (4 - \kappa_T)\,\frac{\delta T}{T}, \tag{4.24}$$

where the choice of $\delta T/T$ at the top is arbitrary and sets the overall normalization. At the base of the layer, the usual approach would be to set $\delta T = 0$, which is appropriate when the thermal timescale at the base is much longer than the growth rate of the mode, γ^{-1}. At marginal stability, however, the growth timescale becomes very long and exceeds the thermal timescale at the base, in which case it is not clear how to set the lower boundary condition. In fact, we find that the results do not depend sensitively on the choice of lower boundary condition. For the results shown, we fix the flux at the base $\delta F = 0$. We find that changing the boundary condition from $\delta F = 0$ to $\delta T = 0$ at the base lowers $\dot{m}_{\rm crit}$ by $< 10\%$ for $Q_b < 0.5$ MeV per nucleon. The differences in $\dot{m}_{crit}$ become larger, roughly a factor of 2, for $Q_b > 1$ MeV per nucleon.

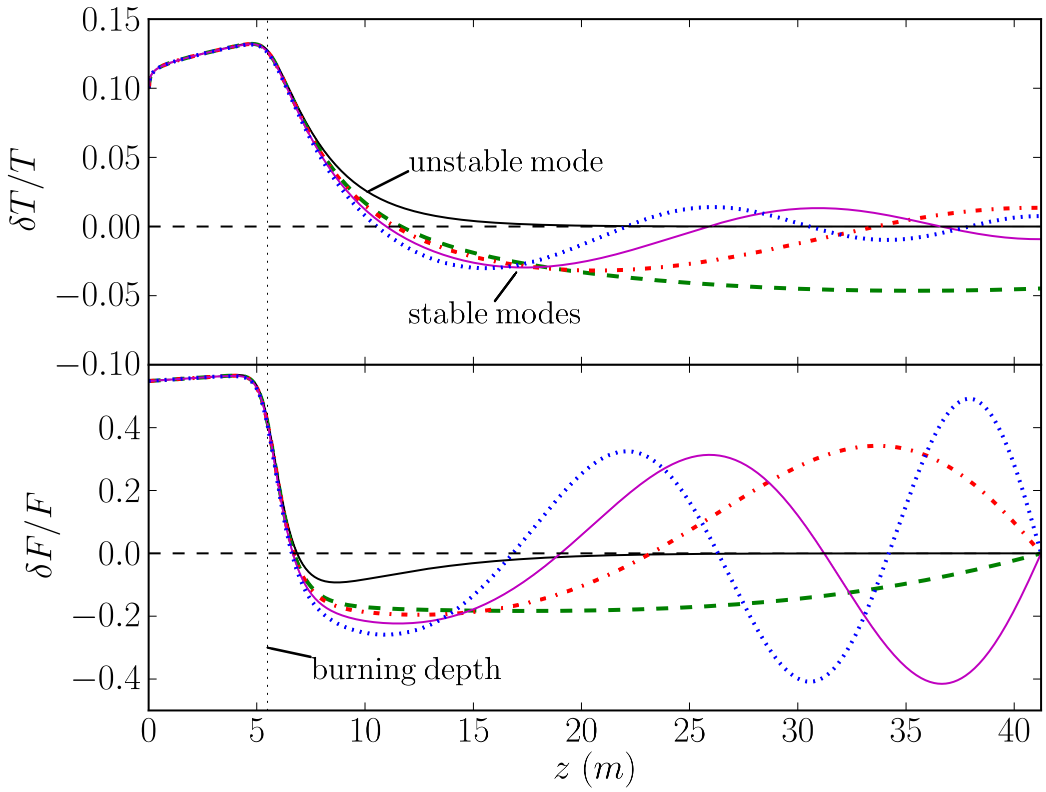

Figure 4.6 Example of the first few perturbed temperature (top panel) and flux (bottom panel) eigenmodes for $\dot{m} = 3\dot{m}_{\rm Edd}$ and $Q_{base} = 0.2$ MeV nuc^{-1}. The eigenmodes displayed have a correspondence with those shown in figure 4.5 at $\dot{m} = 3\dot{m}_{\rm Edd}$, sharing the same line styles and colours. The burning depth, that is, the location at which the triple-alpha burning rate is a maximum in the steady-state models, is represented by the vertical dotted line at roughly $z = 5$ m. A horizontal dashed black line is used to highlight the location of $\delta T/T = 0$ in the top panel, and $\delta F/F = 0$ in the bottom panel. The normalization is chosen so that $\delta T/T = 0.1$ at the top of the layer.

4.4.2 Results

At any given accretion rate and base flux, there are many stable ($\gamma < 0$) eigenmode solutions and at most one unstable mode. The unstable mode, if present, transitions to stability at a specific accretion rate — this defines the stability boundary. As an example, Figure 4.5 shows the values of γ as a function of $\dot{m}$ for the first six eigenmodes, for a base flux $Q_b = 0.2$ MeV per nucleon. The lowest order mode has $\gamma > 0$ (unstable) for $\dot{m} \gtrsim 4\ \dot{m}_{\rm Edd}$ and $\gamma < 0$ (stable) for $\dot{m} \lesssim 4\ \dot{m}_{\rm Edd}$. Figure 4.6 shows the eigenmodes at $\dot{m} = 3\ \dot{m}_{\rm Edd}$, just below the stability boundary in the unstable region, again for $Q_b = 0.2$ MeV per nucleon. The unstable mode has a single peak in δT at the triple-α burning depth, since this is the location at which the thermal runaway occurs during the onset of a burst. The stable (cooling) modes show oscillations, with an increasing number of nodes associated with decreasing (larger negative) values of γ. The cooling eigenmodes with the most negative γ decay most quickly, due to the $e^{\gamma t}$ time dependence of the perturbations.

Rather than searching for $\gamma = 0$ by varying $\dot{m}$, we locate $\dot{m}_{\rm crit}$ at each Q_b by setting $\gamma = 0$ and then treating $\dot{m}$ as the eigenvalue. The resulting stability boundary is shown in the top panel of Figure 4.7, as the solid green curve. We have also included stability curves for the same calculation but with different lower boundaries, $y_{\rm base} = 10^{10}$ and 10^{12} g cm^{-2}. This illustrates the effect of compressional heating: a deeper layer has additional compressional heating, increasing the flux heating the helium layer and stabilizing the burning, moving $\dot{m}_{\rm crit}$ to lower values. As can be seen, the effect is not large, with a $\approx 20\%$ change in $\dot{m}_{\rm crit}$ over the factor of 100 change in $y_{\rm base}$.

To correct for the effect of compressional heating on the stability boundary, in the lower panel of Figure 4.7 we show $\dot{m}_{\rm crit}$ against the sum of Q_b and $Q_{\rm comp}$, which

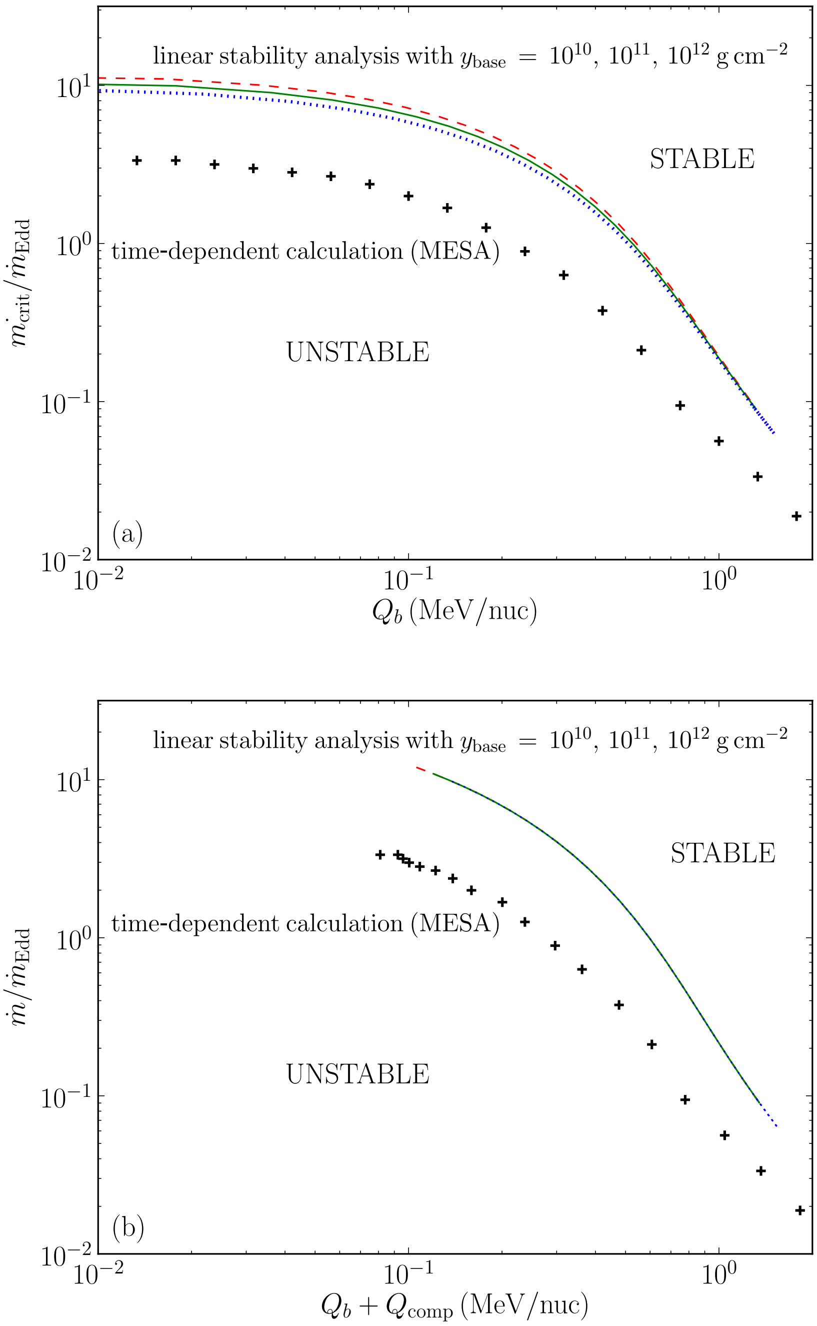

Figure 4.7 (a) The stability boundary for helium burning as found using linear stability analysis (§4.4) is shown as a green solid curve. In addition, the stability curves for the same calculation are shown, using different lower boundary depths, namely $y_{\rm base} = 10^{10}\,{\rm g\,cm^{-2}}$ (red dashed), $y_{\rm base} = 10^{12}\,{\rm g\,cm^{-2}}$ (blue dotted). The MESA stability boundary is represented by black crosses. (b) The same stability boundaries shown in (a), this time plotted against $Q_b + Q_{\rm comp}$, the sum of Q_b and the total contribution to compressional heating across the layer. The linear stability analysis curves with different base depths now overlap each other.

gives the total flux heating the helium burning layer, plus a contribution to $Q_{\rm comp}$ coming from depths shallower than helium burning. The linear stability curves now lie on top of one another for all choices of $y_{\rm base}$. This plot also emphasizes that compressional heating in the ocean sets a minimum value for the effective base flux of $\sim 0.1\,{\rm MeV/nuc}$, similar to the estimate of the total compressional heating that we found in §4.3.2.

Recall that in arriving at equation (4.22), we did not include perturbations of the compressional heating terms from equation (4.19). We checked the effect of including these terms on the stability boundary, and found only a small $6-7\%$ increase in the value of the critical accretion rate. In addition, we also evaluated the effect of changing the surface gravity. A surface gravity of $g_{14} = 1.0\,{\rm cm\,s^{-2}}$ yielded an $\sim 30\%$ decrease in the value of the critical accretion rate, while $g_{14} = 3.0\,{\rm cm\,s^{-2}}$ yielded a $\sim 25\%$ increase. These results agree very well with the $\dot{m}_{\rm crit} \propto g_{14}^{1/2}$ scaling found by Bildsten (1998).

Figure 4.7 shows that the $\dot{m}_{\rm crit}$ calculated with linear stability analysis is a factor of ≈ 3 greater than the $\dot{m}_{\rm crit}$ determined from the time-dependent MESA simulations. The reason for this discrepancy is not clear. We have compared our steady-state models with MESA for values of $\dot{m}$ and Q_b at which MESA achieves a steady solution, while our linear stability analysis predicts instability, and find excellent agreement (see Fig. 4.8). There are small differences in the opacity profile and κ_T (lower panel of Fig. 4.8), but these differences make only a small change in the growth rate. For example, we calculated the linear growth rate for a model with $\dot{m} = 4\dot{m}_{\rm Edd}$ and $Q_b = 0.1$ MeV per nucleon using the κ_T profile from MESA, and compared it to the growth rate found using the κ_T profile from our steady-state models, but found only a small difference, $\gamma = 0.016\ {\rm s^{-1}}$ compared to $\gamma = 0.018\ {\rm s^{-1}}$. Therefore the difference in κ_T profile is not the reason that the model is stable in MESA but unstable according to the linear stability analysis. Lastly, while the profiles for ϵ_T diverge dramatically at depths $y \lesssim 10^5\,\mathrm{g\,cm^{-2}}$, this parameter is irrelevant at these depths since the helium burning rate is negligible. Another possible reason for the difference could be that we have not allowed changes in composition in our linear stability analysis, setting $\delta Y = 0$. However, we do not expect these extra terms to significantly change the results, since the thermal timescale is shorter than the timescale to change composition by a factor $\approx Q_{3\alpha}/C_P T \approx 10$ for $T_8 \approx 3$.

4.5 Summary and Discussion

The main result of the chapter is a new calculation of the critical accretion rate $\dot{m}_{\rm crit}$ at which helium burning stabilizes on accreting neutron stars. We used the MESA stellar evolution code to calculate $\dot{m}_{\rm crit}$ as a function of the base flux heating the helium layer, written in terms of the energy per nucleon Q_b ($F = \dot{m}Q_b$). Equation (4.10) gives an analytic expression for $\dot{m}_{\rm crit}(Q_b)$ in units of the local Eddington rate $\dot{m}_{\rm Edd} = 8.8 \times 10^4$ g cm^{-2} s^{-1}, which should be useful for applications.

In agreement with Keek et al. (2009), we find that the critical accretion rate at low fluxes, $\dot{m}_{\rm crit} \approx 4\ \dot{m}_{\rm Edd}$ is substantially smaller than the rate $\dot{m}_{\rm crit} \approx 20\ \dot{m}_{\rm Edd}$ predicted by one-zone models (Bildsten, 1995, 1998). The difference arises because the one-zone instability criterion (eq. [4.5]) overestimates the burning temperature at marginal stability, which is close to 3.5×10^8 K in multizone models but predicted to be 5×10^8 K in a one-zone model.

We also investigated whether the critical accretion rate can be determined by examining steady-state models only, without running a time-dependent simulation. Paczynski (1983a) showed that a one-zone model with $Q_b = 0$ has a turning point

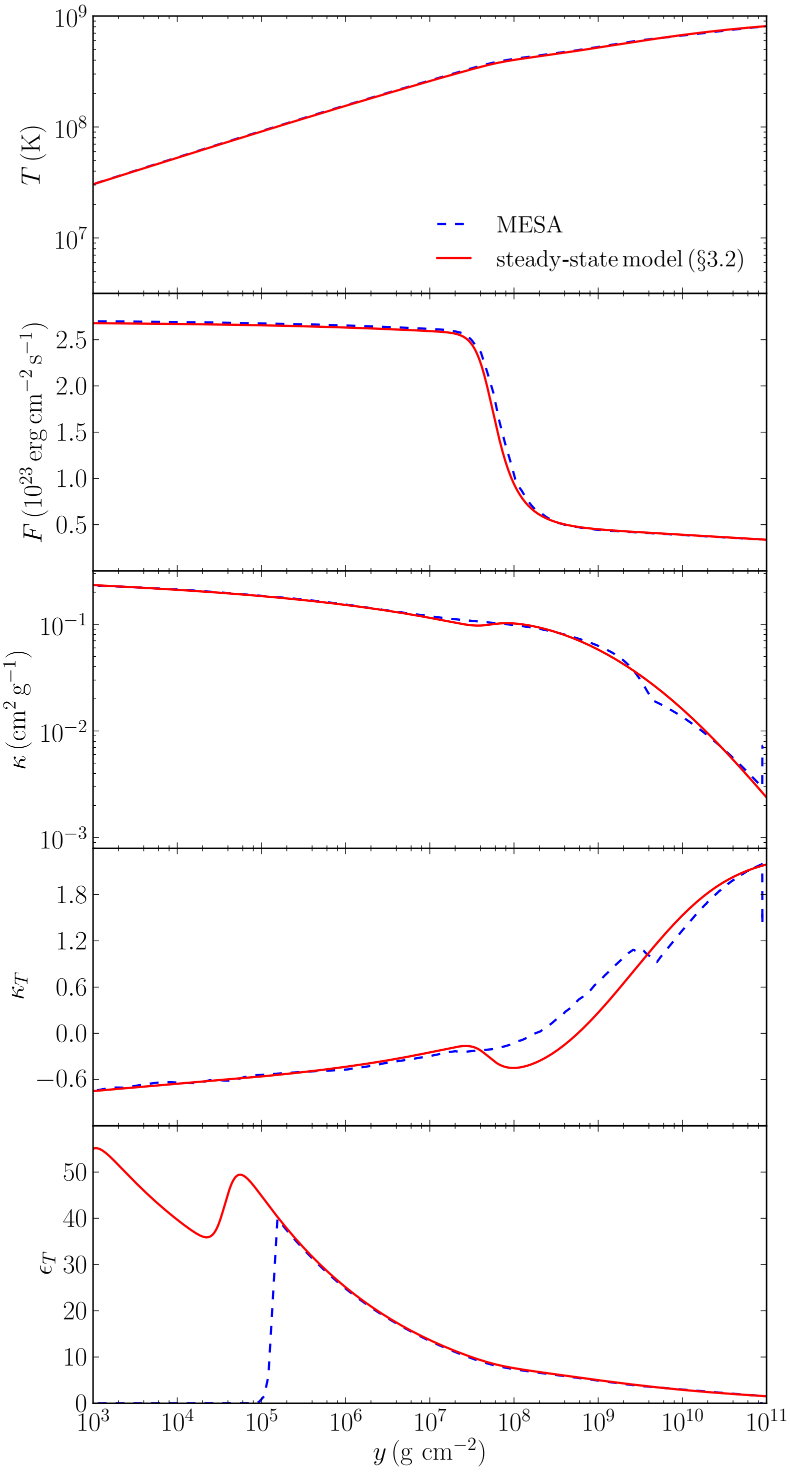

Figure 4.8 A comparison of steady burning model calculations using MESA (blue) and the model presented in §4.3.2, with $\dot{m} = 4\dot{m}_{\mathrm{Edd}}$ and $Q_b = 0.1\,\mathrm{MeV\,nuc^{-1}}$. At this accretion rate and base flux, the MESA simulation indicates that this model is stable, while our linear stability analysis (§4.4.1) indicates that the model is unstable. Profiles for the temperature, flux, opacity, and opacity and burning rate derivatives κ_T, ϵ_T (both taken at constant pressure) are shown.

in the burning depth $dy/d\dot{m} = 0$ at marginal stability. We find that this result does not hold in one-zone models when a base flux is included, and does not hold for any value of Q_b in multizone models. This is contrary to the findings of Narayan & Heyl (2003), who studied multizone models with $Q_b = 0$.

We then carried out a linear stability analysis of steady-state burning models to determine the stability boundary. Linear stability analysis has been applied to nuclear burning on neutron stars before (e.g. Narayan & Heyl 2003), but not compared directly to time-dependent simulations. Although the shape of the $\dot{m}_{\rm crit}(Q_b)$ curve is reproduced quite well (Fig. 4.8), the linear stability analysis overestimates $\dot{m}_{\rm crit}$ by a factor of about 3. We were not able to identify the reason for the discrepancy; for now we must take the results of linear stability analysis as approximate. Narayan & Heyl (2003) assumed a solar composition, and so cannot be compared with our results.

Heger et al. (2007a) discussed a further prediction of theoretical models, that close to marginal stability, the eigenvalue of thermal perturbations becomes complex (Paczynski, 1983a), leading to an oscillatory mode of burning which has been identified with mHz frequency quasi-periodic oscillations (mHz QPOs) observed from 3 X-ray binaries (Revnivtsev et al., 2001; Altamirano et al., 2008; Linares et al., 2012). By considering only thermal perturbations in this chapter, we have confined our attention to the real part of the eigenvalue, neglecting the compositional perturbations that are important in marginally-stable burning. This is a straightforward extension of the method presented here, and remains to be addressed in a future paper.

It would be interesting to apply the linear stability analysis to steady-state models of solar composition, which include hydrogen burning by the rp-process. A large grid of models were recently published as a function of Q_b and helium fraction Y (Stevens et al., 2014). Heger et al. (2007b) found the stability boundary $\dot{m}_{\rm crit} = 0.924\,\dot{m}_{\rm Edd}$ for

$Q_b = 0.15$ MeV per nucleon in simulations with the KEPLER code. Keek et al. (2014) extend these calculations to investigate the sensitivity of $\dot{m}_{\rm crit}$ to nuclear reaction uncertainties. For their standard set of rates, they have $\dot{m}_{\rm crit} \approx 1.1\ \dot{m}_{\rm Edd}$. Bildsten (1998) estimated $\dot{m}_{\rm crit} = 0.74\ \dot{m}_{\rm Edd}$ for solar composition using the one-zone ignition criterion. In that case, the one-zone estimate appears to give a much more accurate estimate than for pure helium.

The transition to stable burning is believed to explain the observed quenching of Type I X-ray bursts following a superburst (Kuulkers et al., 2002; Cumming & Bildsten, 2001b; Cumming, 2004; Keek et al., 2012). Cumming (2004) assumed that the critical flux that would quench burning is $Q_b \approx 0.7$ MeV per nucleon, independent of accretion rate. In fact, as we showed in this chapter, we expect the Q_b required to stabilize burning to depend strongly on $\dot{m}$. Superburst sources are not pure helium accretors in general, but we can compare our results with Keek et al. (2012), who ran time-dependent simulations of superbursts and studied quenching for the pure helium case. They found that burning became unstable as the luminosity dropped through $L \approx 4 \times 10^{35}$ erg s^{-1} for accretion at $0.3\ \dot{m}_{\rm Edd}$. Subtracting the nuclear burning flux, this is in good agreement with Figure 4.7 which predicts a critical flux of $Q_b \approx 0.5$ MeV per nucleon for this accretion rate. The fact that this is close to the value assumed by Cumming (2004) suggests that their results may not be strongly affected by their assumption that Q_b is independent of $\dot{m}$.

Our results can be immediately applied to 4U 1820-30, an ultracompact binary that most likely accretes pure helium. It displays regular Type I X-ray bursts in its low state, which disappear when the accretion rate increases and the source enters the soft state (Clark et al., 1977; Cornelisse et al., 2003). Cumming (2003) found that at the local rate of $\dot{m}_X = 1.2 \times 10^4$ g cm^{-2} s^{-1} $= 0.14\ \dot{m}_{\rm Edd}$ (as inferred from the X-ray luminosity of the source when bursts are seen), a flux from below of $Q_b = 0.4$ MeV per nucleon was necessary to explain the short ≈ 3 hours burst recurrence times. For this value of Q_b, we find that burning will stabilize above $\dot{m} = 0.35\ \dot{m}_{\rm Edd}$ (using eq. [4.10]). This can be accommodated in the range of accretion rates observed in the 6 month cycle of 4U 1820-30, which is about a factor of 3. Therefore, it may be possible to make a consistent model of the burst recurrence time and the quenching of bursts at higher accretion rates by including a base flux of the appropriate size that is always present. An alternative is that the flux switches on at a critical rate, quenching the burning, but this would have difficulty explaining the short recurrence times when bursts are seen. Time-dependent simulations, e.g. with the MESA code, are required to test whether a self-consistent model of the bursting behavior of 1820-30 can be made.

One issue for explaining the transition to stable burning is the timescale on which bursts appear or disappear as the accretion rate changes. in't Zand et al. (2012) noted that the burst behavior in 4U 1820-30 changes within a day or two of entering or leaving the low state. They suggest that this implies that the shallow heat source must lie at a depth where the thermal time is $\lesssim 1$ day, corresponding to a density of $\rho \approx 10^9$ g cm^{-2}, so that it can adjust to the changing accretion rate. Otherwise, for example, when the accretion rate dropped into the low state, the luminosity from the crust would remain as it was in the high state, not having time to thermally adjust, and X-ray bursts would remain quenched. Instead, we want the luminosity to adjust to a new value of $Q_b\dot{m}$ so that bursting activity can resume.

The fact that the stability boundaries for pure helium and solar composition are closer than previously thought (based on one-zone models, in which they are more than an order of magnitude different) may help to explain why burning stabilizes in

4U 1820-30 at a similar accretion rate to other low mass X-ray binary neutron stars that accrete hydrogen rich material.

5

Conclusion

Type I X-ray bursts are useful for probing neutron star interiors, from measurements of mass and radius, as well as through their thermal structure and evolution. There are challenges associated with both avenues. Systematic uncertainties are thought to affect current measurements of mass and radius from X-ray bursts, and the accurate modelling of the thermal structure of neutron stars has required the inclusion of an unknown, strong heat source. In this thesis, we have taken some steps towards resolving these challenges.

5.1 Summary of main results

In Chapter 2, we addressed ongoing issues relating to systematic uncertainties associated with measurements of mass and radius from Type I X-ray bursts. To do so, we developed a method for deriving mass and radius constraints which do not depend on the distance to the source, or the anisotropy factor. We applied our method to the burst source GS $1826-24$. The main result of this chapter is shown in Figure 2.5, which shows a summary of the distance and anisotropy-independent mass and radius constraints for GS $1826-24$.

In Chapter 3, we took a close look at the comparison of simulated lightcurves to observations of GS $1826-24$, which were used in Chapter 2, and found that our understanding of this source is incomplete. Using an empirical law relating the peak flux to the average helium mass fraction in the accreted layer at ignition, which was calibrated to Kepler simulations, we argue that the data can be well-described by a low-metallicity and helium-enriched accretion model. We also rederived the mass and radius constraints on R_∞ described in the previous chapter, using the most recent burst spectra calculations. The main results of Chapter 3 can be summarized as follows:

- Figure 3.2 shows that solar composition models, previously shown to describe GS $1826-24$ lightcurves well, do not capture the change in the observed peak flux at higher recurrence times.
- Figure 3.3 shows an empirical relation between peak flux and the average helium mass fraction of the layer before ignition, which is calibrated to Kepler lightcurve simulations. The numerical form of this law is stated in equation 3.7.
- In Figure 3.4, we show fits to GS $1826-24$ which are indicative of a low-metallicity accretion.
- Figure 3.5 is an update to Figure 2.5, showing a summary of mass and radius constraints for GS $1826-24$ based on comparisons to updated spectral models. The upper limits on R_∞ have increased by $10-20\%$.

In Chapter 4, we attempted to constrain the strength of the shallow heat source in 4U $1820-30$, by modelling the stability of helium burning as a function of the heat flux emerging from deeper layers. Different approaches to this problem were explored, including a one-zone model calculation, linear stability analysis of a large suite of steady-state models, and a time-dependent multizone simulation of bursts using MESA. As such, this chapter presents the first scientific application of MESA to the study of Type I X-ray bursts. The salient results of Chapter 4 are summarized:

- Equation (4.10) is an analytic expression for the critical accretion rate, at the transition between stable and unstable helium burning, as a function of the heat flux from below. This expression is calibrated to a time-dependent multizone calculation using the stellar evolution code MESA.
- Figure 4.4 shows that the turning point $dy_{\rm burn}/d\dot{m} = 0$ does not correspond to the stability boundary, as has been previously suggested.
- Figure 4.7 summarizes the discrepancy in critical accretion rate values between the linear stability analysis and the time-dependent multizone calculation.

5.2 Future work

This is an exciting time in neutron star astrophysics, given the number of different observable phenomena which probe the different depths of the star. The passive cooling of young isolated neutron stars via neutrinos probes the very interior of the star. Thermal relaxation of quiescent SXRTs can probe the physics of the crust. Meanwhile, regular X-ray bursts and superbursts give us clues about the thermal state and composition of various depths of the ocean. Finally, thermal emission gives us insights into the composition and properties of the very surface of the neutron star.

In the long term, the future of mass and radius constraints from X-ray bursts is uncertain. On the one hand, we require a better understanding of the systematic uncertainties that affect the current leading approaches. On the other hand, we have shown a different approach to this problem, one that may be expanded upon in the future. It may be that mass constraints will be more reliably found from other sources, such as Shapiro delay measurements in double degenerate binaries (Demorest et al., 2010), for example. However, there are not strong prospects for radius measurements from sources outside of LMXB systems. Perhaps a simultaneous fit including different measurements of the same star will allow us recognize and minimize the effects of systematic uncertainties.

A natural follow-up to Chapter 2, given the results of Chapter 3, is a new derivation of mass and radius constraints, with lightcurves that are shown to accurately describe the behaviour of GS $1826-24$. The method we derived is also applicable to other sources, such as KS $1731-260$, another example of mixed H/He burning. What is required are additional lightcurve simulations to compare to. The recent release of the open source stellar evolution code MESA is a very positive development in that respect. The code is directly applicable to X-ray bursts in neutron stars, and therefore is a tool that anyone can use to start mapping out the range of behaviours of lightcurves with accretion rate and composition. One aspect which could be investigated using MESA or other stellar evolution codes, is the theoretical uncertainty in simulations. For example, knowing the theoretical uncertainty in the peak flux would allow us to have a better handle on the uncertainty of our derived redshift constraint, in equation 2.5.

There are a few questions that Chapter 3 leaves unanswered. The derivation of the empirical law between the peak flux and the average helium mass fraction of the layer before ignition hinges on a number of assumptions which would be good to verify. For example, do the Kepler simulations show the predicted evolution of $\overline{Y}$ between bursts? Also, does the peak flux linearly correlate with $\overline{Y}$, particularly outside of the $Y_0 - Z_0$ trend used for Kepler models shown in Chapter 3? And the most important question, would low-metallicity, helium-enriched models reproduce the GS $1826-24$ lightcurves?

Chapter 3 exemplified the importance of the rp-process in mixed H/He X-ray bursts. Bursts from GS $1826-24$ have traditionally been used as probes for rp-process burning. Currently, a new facility called FRIB (Facility for Rare Isotope Beams) is set begin experiments in 2022. This will provide much needed experimental measurements of the many reaction rates within the rp-process. This will enable better modelling of the nuclear burning aspect of X-ray bursts, which will translate into more fruitful comparisons to observations.

Chapter 4, among other things, presented a first step in developing MESA as a general tool for the study of Type I X-ray bursts on accreting neutron stars. The release of MESA is a very exciting development for the theoretical aspect of X-ray burst study, and it offers many new opportunities for research. Relating to Chapter 4 specifically, a detailed analysis of burst sequences and the evolution of the burning layers is needed, starting with the simple pure helium case. From there, an application to mixed H/He burning would be straightforward.

A detailed approach to the modelling of 4U $1820-30$ could form a consistent picture for this source, tying together its bursting behaviour, the strong shallow heat source, and the production of carbon necessary for the superbursts that this source has shown. The stabilization of the regular bursts from the shallow heat source causes the production of carbon from stable helium burning. The shallow heat source must, however, not be so strong that carbon also burns in a stable manner. It would be interesting to see if, using MESA or another stellar evolution code, we could form a self-consistent model for 4U $1820-30$ within these constraints.

Appendices

A

Eulerian perturbations

In §4.1 of chapter 4, we derived the perturbation equations using pressure coordinates, a Lagrangian approach. Here we instead use an Eulerian approach, where perturbations are taken at fixed spatial position, and show that the perturbation equations reduce to those derived in §4.1 when written in terms of Lagrangian quantities. We follow the convention of Cox (1980) by denoting Eulerian perturbations using the prime symbol. For example, T' represents the Eulerian temperature perturbation. The Lagrangian temperature perturbation is then $\delta T = T' + \xi_z \partial T/\partial z$, where ξ_z is the vertical displacement. The displacement obeys the continuity equation

$$\frac{d}{dy}\xi_z = \frac{\delta\rho}{\rho^2} = -\frac{\chi_T}{\rho\chi_\rho}\frac{\delta T}{T}, \tag{A.1}$$

where we have set $\delta P = 0$.

Perturbing equation (4.18) using Eulerian perturbations gives

$$-\frac{1}{\rho}\frac{\partial T'}{\partial z} = -\frac{1}{\rho}\frac{\partial T}{\partial z}\left[\frac{F'}{F} - 3\frac{T'}{T} + \frac{\kappa'}{\kappa} + \frac{\rho'}{\rho}\right]. \tag{A.2}$$

Now to rewrite this in terms of Langrangian perturbations. The gradient of the

Lagrangian temperature perturbation is

$$\frac{\partial \delta T}{\partial z} = \frac{\partial T'}{\partial z} + \frac{\partial}{\partial z}\left(\xi_z \frac{\partial T}{\partial z}\right) = \frac{\partial T'}{\partial z} - \frac{\partial T}{\partial z}\frac{\delta\rho}{\rho} + \xi_z \frac{\partial^2 T}{\partial z^2}, \tag{A.3}$$

where we used the continuity equation $d\xi_z/dz = -\delta\rho/\rho$ to substitute for ξ_z. Combining this with equation (A.2) gives

$$\frac{\partial \delta T}{\partial z} = \frac{\partial T}{\partial z}\left[\frac{\delta F}{F} - 3\frac{\delta T}{T} + \frac{\delta\kappa}{\kappa}\right] - \xi_z \frac{\partial T}{\partial z}\frac{\partial}{\partial z}\left[\ln\left(\frac{F\kappa\rho}{T^3 \frac{\partial T}{\partial z}}\right)\right]. \tag{A.4}$$

The last term in equation (A3) vanishes since the expression inside the logarithm is a constant, giving

$$\frac{\partial \delta T}{\partial y} = \frac{dT}{dy}\left[\frac{\delta F}{F} + \left(\frac{\kappa_T - 3}{T}\right)\delta T\right]. \tag{A.5}$$

We have recovered equation (4.23) from §4.1.

Next, the Eulerian-perturbed entropy equation is

$$\gamma c_P \delta T = \epsilon' + \frac{1}{\rho}\frac{\partial F}{\partial z}\frac{\rho'}{\rho} - \frac{1}{\rho}\frac{\partial F'}{\partial z}. \tag{A.6}$$

As above, we express the Eulerian perturbations as Lagrangian perturbations:

$$\begin{aligned} \gamma c_P \delta T &= \delta\epsilon + \frac{1}{\rho}\frac{\partial F}{\partial z}\frac{\delta\rho}{\rho} - \frac{1}{\rho}\frac{\partial \delta F}{\partial z} + \frac{1}{\rho}\frac{\partial F}{\partial z}\frac{\partial \xi_z}{\partial z} \\ &\quad - \xi_z\left[\frac{\partial\epsilon}{\partial z} + \frac{1}{\rho}\frac{\partial F}{\partial z}\frac{d\ln\rho}{dz} - \frac{1}{\rho}\frac{\partial}{\partial z}\frac{\partial F}{\partial z}\right]. \end{aligned} \tag{A.7}$$

Using the expression $\delta\rho/\rho = -d\xi_z/dz$, and

$$\frac{\partial}{\partial z}\left(\frac{1}{\rho}\frac{\partial F}{\partial z}\right) = \frac{1}{\rho}\frac{\partial}{\partial z}\frac{\partial F}{\partial z} - \frac{1}{\rho}\frac{\partial \ln\rho}{\partial z}\frac{\partial F}{\partial z}, \tag{A.8}$$

equation (A.7) simplifies to

$$\gamma c_P \delta T \;=\; \delta\epsilon - \frac{1}{\rho}\frac{\partial \delta F}{\partial z} - \xi_z \frac{\partial}{\partial z}\left[\epsilon - \frac{1}{\rho}\frac{\partial F}{\partial z}\right]. \tag{A.9}$$

The two terms inside the bracket cancel out in steady state, and we are left with

$$\frac{\partial \delta F}{\partial y} \;=\; \delta T\left(\gamma c_P - \frac{\epsilon \epsilon_T}{T}\right), \tag{A.10}$$

which is equation (4.22) from §4.1.

The set of Eulerian perturbed equations (A.1), (A.2), and (A.6) are physically equivalent to the Lagrangian perturbation equations. If we use the same boundary conditions, as outlined in §4.1, with the additional condition on the vertical displacement, $\xi_z = 0$ at the base, we get the same solutions. However, integration of the Eulerian equations is more complex computationally, because of the additional boundary condition.

Bibliography

Altamirano, D., Keek, L., Cumming, A., Sivakoff, G. R., Heinke, C. O., Wijnands, R., Degenaar, N., Homan, J., & Pooley, D. 2012, MNRAS, 426, 927

Altamirano, D., van der Klis, M., Wijnands, R., & Cumming, A. 2008, ApJ, 673, L35

Backer, D. C., Kulkarni, S. R., Heiles, C., Davis, M. M., & Goss, W. M. 1982, Nature, 300, 615

Bethe, H. A. 1939, Physical Review, 55, 434

Bildsten, L. 1995, ApJ, 438, 852

Bildsten, L. 1998, in NATO ASIC Proc. 515: The Many Faces of Neutron Stars., ed. R. Buccheri, J. van Paradijs, & A. Alpar, 419–+

Bildsten, L. 2000, in American Institute of Physics Conference Series, Vol. 522, American Institute of Physics Conference Series, ed. S. S. Holt & W. W. Zhang, 359–369

Brown, E. F. 2000, ApJ, 531, 988

—. 2004, ApJ, 614, L57

Brown, E. F. & Bildsten, L. 1998, ApJ, 496, 915

Brown, E. F., Bildsten, L., & Rutledge, R. E. 1998, ApJ, 504, L95

Brown, E. F. & Cumming, A. 2009, ApJ, 698, 1020

Clark, G. W., Li, F. K., Canizares, C., Hayakawa, S., Jernigan, G., & Lewin, W. H. G. 1977, MNRAS, 179, 651

Clayton, D. D. 1968, Principles of stellar evolution and nucleosynthesis, ed. Clayton, D. D.

Cocchi, M., Bazzano, A., Natalucci, L., Ubertini, P., Heise, J., in't Zand, J. J. M., Muller, J. M., & Smith, M. J. S. 2000, in American Institute of Physics Conference Series, Vol. 510, American Institute of Physics Conference Series, ed. M. L. McConnell & J. M. Ryan, 203–207

Cornelisse, R., in't Zand, J. J. M., Verbunt, F., Kuulkers, E., Heise, J., den Hartog, P. R., Cocchi, M., Natalucci, L., Bazzano, A., & Ubertini, P. 2003, A&A, 405, 1033

Cox, J. P. 1980, Theory of stellar pulsation

Cumming, A. 2003, ApJ, 595, 1077

—. 2004, Nuclear Physics B Proceedings Supplements, 132, 435

Cumming, A. & Bildsten, L. 2000, ApJ, 544, 453

—. 2001a, ApJ, 559, L127

—. 2001b, ApJ, 559, L127

Cumming, A., Macbeth, J., in 't Zand, J. J. M., & Page, D. 2006, ApJ, 646, 429

Degenaar, N., Wijnands, R., & Miller, J. M. 2013, ApJ, 767, L31

Demorest, P. B., Pennucci, T., Ransom, S. M., Roberts, M. S. E., & Hessels, J. W. T. 2010, Nature, 467, 1081

Ebisuzaki, T. 1987, PASJ, 39, 287

Fujimoto, M. Y. 1988, ApJ, 324, 995

Fujimoto, M. Y., Hanawa, T., Iben, Jr., I., & Richardson, M. B. 1987a, ApJ, 315, 198

Fujimoto, M. Y., Hanawa, T., & Miyaji, S. 1981, ApJ, 247, 267

Fujimoto, M. Y., Sztajno, M., Lewin, W. H. G., & van Paradijs, J. 1987b, ApJ, 319, 902

Fushiki, I. & Lamb, D. Q. 1987a, ApJ, 323, L55

—. 1987b, ApJ, 317, 368

Galloway, D. K. & Cumming, A. 2006, ApJ, 652, 559

Galloway, D. K., Cumming, A., Kuulkers, E., Bildsten, L., Chakrabarty, D., & Rothschild, R. E. 2004, ApJ, 601, 466

Galloway, D. K., Muno, M. P., Hartman, J. M., Psaltis, D., & Chakrabarty, D. 2008, ApJS, 179, 360

Goldreich, P. & Julian, W. H. 1969, ApJ, 157, 869

Güver, T., Özel, F., Cabrera-Lavers, A., & Wroblewski, P. 2010a, ApJ, 712, 964

Güver, T., Wroblewski, P., Camarota, L., & Özel, F. 2010b, ApJ, 719, 1807

Haensel, P., Potekhin, A. Y., & Yakovlev, D. G., eds. 2007, Astrophysics and Space Science Library, Vol. 326, Neutron Stars 1 : Equation of State and Structure

Haensel, P., Zdunik, J. L., & Schaefer, R. 1986, A&A, 160, 121

Hanawa, T. & Fujimoto, M. Y. 1986, PASJ, 38, 13

Hansen, C. J. & Kawaler, S. D. 1994, Stellar Interiors. Physical Principles, Structure, and Evolution.

Hansen, C. J., Kawaler, S. D., & Trimble, V. 2004, Stellar interiors : physical principles, structure, and evolution, ed. Hansen, C. J., Kawaler, S. D., & Trimble, V.

Hansen, C. J. & van Horn, H. M. 1975, ApJ, 195, 735

Heger, A., Cumming, A., Galloway, D. K., & Woosley, S. E. 2007a, ApJ, 671, L141

Heger, A., Cumming, A., & Woosley, S. E. 2007b, ApJ, 665, 1311

Heinke, C. O., Altamirano, D., Cohn, H. N., Lugger, P. M., Budac, S. A., Servillat, M., Linares, M., Strohmayer, T. E., Markwardt, C. B., Wijnands, R., Swank, J. H., Knigge, C., Bailyn, C., & Grindlay, J. E. 2010, ApJ, 714, 894

Heinke, C. O., Jonker, P. G., Wijnands, R., & Taam, R. E. 2007, ApJ, 660, 1424

Hoffman, J. A., Cominsky, L., & Lewin, W. H. G. 1980, ApJ, 240, L27

Hoyle, F. 1954, ApJS, 1, 121

Inogamov, N. A. & Sunyaev, R. A. 1999, Astronomy Letters, 25, 269

—. 2010, Astronomy Letters, 36, 848

in't Zand, J. J. M., Homan, J., Keek, L., & Palmer, D. M. 2012, A&A, 547, A47

in't Zand, J. J. M., Keek, L., Cumming, A., Heger, A., Homan, J., & Méndez, M. 2009, A&A, 497, 469

in't Zand, J. J. M., Kuulkers, E., Verbunt, F., Heise, J., & Cornelisse, R. 2003, A&A, 411, L487

Kajava, J. J. E., Nättilä, J., Latvala, O.-M., Pursiainen, M., Poutanen, J., Suleimanov, V. F., Revnivtsev, M. G., Kuulkers, E., & Galloway, D. K. 2014, ArXiv e-prints

Keek, L., Cyburt, R. H., & Heger, A. 2014, ApJ, 787, 101

Keek, L. & Heger, A. 2011, ApJ, 743, 189

Keek, L., Heger, A., & in't Zand, J. J. M. 2012, ApJ, 752, 150

Keek, L., in't Zand, J. J. M., Kuulkers, E., Cumming, A., Brown, E. F., & Suzuki, M. 2008, A&A, 479, 177

Keek, L., Langer, N., & in't Zand, J. J. M. 2009, A&A, 502, 871

Kuulkers, E., in't Zand, J. J. M., van Kerkwijk, M. H., Cornelisse, R., Smith, D. A., Heise, J., Bazzano, A., Cocchi, M., Natalucci, L., & Ubertini, P. 2002, A&A, 382, 503

Lapidus, I. I. & Sunyaev, R. A. 1985, MNRAS, 217, 291

Lattimer, J. M. & Prakash, M. 2007, Phys. Rep., 442, 109

Lewin, W. H. G., van Paradijs, J., & Taam, R. E. 1993, Space Science Reviews, 62, 223

Linares, M., Altamirano, D., Chakrabarty, D., Cumming, A., & Keek, L. 2012, ApJ, 748, 82

Liu, Q. Z., van Paradijs, J., & van den Heuvel, E. P. J. 2007, A&A, 469, 807

London, R. A., Howard, W. M., & Taam, R. E. 1984, ApJ, 287, L27

London, R. A., Taam, R. E., & Howard, W. M. 1986, ApJ, 306, 170

Madej, J. 1974, Acta Astronomica, 24, 327

Madej, J., Joss, P. C., & Różańska, A. 2004, ApJ, 602, 904

Majczyna, A., Madej, J., Joss, P. C., & Różańska, A. 2005, A&A, 430, 643

Miller, M. C. 2013, ArXiv e-prints

Narayan, R. & Heyl, J. S. 2003, ApJ, 599, 419

Nelson, L. A., Rappaport, S. A., & Joss, P. C. 1986, ApJ, 304, 231

Oppenheimer, J. R. & Volkoff, G. M. 1939, Physical Review, 55, 374

Özel, F., Baym, G., & Güver, T. 2010, Phys. Rev. D, 82, 101301

Özel, F., Güver, T., & Psaltis, D. 2009, ApJ, 693, 1775

Paczynski, B. 1983a, ApJ, 264, 282

—. 1983b, ApJ, 267, 315

Page, D., Lattimer, J. M., Prakash, M., & Steiner, A. W. 2004, ApJS, 155, 623

Page, D., Prakash, M., Lattimer, J. M., & Steiner, A. W. 2011, Physical Review Letters, 106, 081101

Page, D. & Reddy, S. 2006, Annual Review of Nuclear and Particle Science, 56, 327

Pavlov, G. G., Shibanov, I. A., & Zavlin, V. E. 1991, MNRAS, 253, 193

Paxton, B., Bildsten, L., Dotter, A., Herwig, F., Lesaffre, P., & Timmes, F. 2011, ApJS, 192, 3

Paxton, B., Cantiello, M., Arras, P., Bildsten, L., Brown, E. F., Dotter, A., Mankovich, C., Montgomery, M. H., Stello, D., Timmes, F. X., & Townsend, R. 2013, ApJS, 208, 4

Piro, A. L. & Bildsten, L. 2007, ApJ, 663, 1252

Prakash, M., Lattimer, J. M., & Ainsworth, T. L. 1988, Physical Review Letters, 61, 2518

Prakash, M., Lattimer, J. M., Pons, J. A., Steiner, A. W., & Reddy, S. 2001, in Lecture Notes in Physics, Berlin Springer Verlag, Vol. 578, Physics of Neutron Star Interiors, ed. D. Blaschke, N. K. Glendenning, & A. Sedrakian, 364

Revnivtsev, M., Churazov, E., Gilfanov, M., & Sunyaev, R. 2001, A&A, 372, 138

Schatz, H., Aprahamian, A., Barnard, V., Bildsten, L., Cumming, A., Ouellette, M., Rauscher, T., Thielemann, F., & Wiescher, M. 2001, Physical Review Letters, 86, 3471

Schatz, H., Aprahamian, A., Goerres, J., Wiescher, M., Rauscher, T., Rembges, J. F., Thielemann, F.-K., Pfeiffer, B., Moeller, P., Kratz, K.-L., Herndl, H., Brown, B. A., & Rebel, H. 1998, Phys. Rep., 294, 167

Schatz, H., Bildsten, L., Cumming, A., & Ouellette, M. 2003, Nuclear Physics A, 718, 247

Schatz, H., Bildsten, L., Cumming, A., & Wiescher, M. 1999, ApJ, 524, 1014

Schatz, H., Gupta, S., Möller, P., Beard, M., Brown, E. F., Deibel, A. T., Gasques, L. R., Hix, W. R., Keek, L., Lau, R., Steiner, A. W., & Wiescher, M. 2014, Nature, 505, 62

Schwarzschild, M. & Härm, R. 1965, ApJ, 142, 855

Smarr, L. L. & Blandford, R. 1976, ApJ, 207, 574

Steiner, A. W., Lattimer, J. M., & Brown, E. F. 2010, ApJ, 722, 33

Stella, L., Priedhorsky, W., & White, N. E. 1987, ApJ, 312, L17

Stevens, J., Brown, E. F., Cumming, A., Cyburt, R., & Schatz, H. 2014, ArXiv e-prints

Suleimanov, V., Poutanen, J., Revnivtsev, M., & Werner, K. 2011a, ApJ, 742, 122

Suleimanov, V., Poutanen, J., & Werner, K. 2011b, A&A, 527, A139

—. 2012, A&A, 545, A120

Taam, R. E. 1981, ApJ, 247, 257

Tauris, T. M. & van den Heuvel, E. 2003, ArXiv Astrophysics e-prints

Timmes, F. X., Woosley, S. E., & Weaver, T. A. 1996, ApJ, 457, 834

van Paradijs, J., Penninx, W., & Lewin, W. H. G. 1988, MNRAS, 233, 437

Wallace, R. K. & Woosley, S. E. 1981, ApJS, 45, 389

Wiescher, M., Grres, J., Uberseder, E., Imbriani, G., & Pignatari, M. 2010, Annual Review of Nuclear and Particle Science, 60

Witten, E. 1984, Phys. Rev. D, 30, 272

Woosley, S. E., Heger, A., Cumming, A., Hoffman, R. D., Pruet, J., Rauscher, T., Fisker, J. L., Schatz, H., Brown, B. A., & Wiescher, M. 2004, ApJS, 151, 75

Yakovlev, D. G. & Pethick, C. J. 2004, ARA&A, 42, 169

Yoon, S.-C., Langer, N., & van der Sluys, M. 2004, A&A, 425, 207

Zamfir, M., Cumming, A., & Galloway, D. K. 2012, ApJ, 749, 69

Zavlin, V. E., Pavlov, G. G., & Shibanov, Y. A. 1996, A&A, 315, 141